Quantum feedback and quantum correlation measurements with a single Barium ion

Dissertation

zur Erlangung des Doktorgrades an der
naturwissenschaftlichen Fakultät
der Leopold-Franzens-Universität Innsbruck

vorgelegt von

Mag. Daniel Rotter

durchgeführt am Institut für Experimentalphysik
unter der Leitung von
Univ.-Prof. Dr. Rainer Blatt

Februar 2008

Abstract

This thesis reports on various experiments to fully characterize and manipulate the wave-function - regarding both internal (electronic) and external (motional) degrees of freedom - of a single Barium ion stored in a Paul trap. The ion is laser-cooled and -excited by two fields at 493 nm and 650 nm driving the 6 $^2S_{1/2}$ to 6 $^2P_{1/2}$ and 6 $^2P_{1/2}$ to 5 $^2D_{3/2}$ respectively confining the ion within $\sim$35 nm. Scattered photons at the wavelength of 493 nm are observed perpendicular to the laser excitation direction and sent to a Hanbury-Brown and Twiss setup consisting of a 50/50 beam splitter and two photo-multipliers in the individual output-channels. The photocurrent contains all the information about the electronic and motional degrees of freedom of the ion and is investigated in both the frequency domain and in the time domain by measuring correlations between the output ports (second order or "intensity" correlation function).

The basic physical phenomenon underlying all presented experiments is the self-interference of single fluorescence photons in a self-homodyne configuration. A part of the fluorescence is collected with a lens inside the vacuum, collimated and sent to a mirror placed outside the vacuum chamber (the "distant" mirror). The back-reflected light creates a mirror image of the ion which is superimposed with the ion yielding interference of individual fluorescence photons.

The high spatial resolution of the interference on the one hand allows to monitor the motion of the ion in the trapping potential: A moving ion modulates the observed resonance fluorescence and a sideband at the motional frequency appears in the spectrum of the photo-current (motional sidebands). This information can be used to apply electronic feedback. Experiments are demonstrated, where this feedback provides cooling below the Doppler limit.

An analysis of the photo-current in the time-domain indeed reveals this motional sidebands as well. They appear as a modulation of the second order correlation function for times on the order of μs. It is shown, that the stability of the trap and the motional frequencies are deduced. For short times, on the order of ns these measurements furthermore exhibit the internal dynamics of the ion (i.e. the emission properties or "Anti-bunching").

On the other hand the effect of the self-interference allows to perform cavity quantum electro dynamics (QED) measurements - in a bad cavity regime. Measurements are presented, where the relative position of the ion in the interference pattern strongly influences the detection probability of a second photon after a first one. The investigation is carried out in the non-Markovian regime where time-delay effects are not negligible. These measurements are the first ones to study cavity QED in this regime.

In the last chapter an experiment is shown, where a single Barium is transformed into a pseudo two-photon source of almost identical photon pairs. Fluorescence photons are sent to beam-splitter, coupled into fibers and recombined on a 50/50 beam splitter to perform a two-photon interference experiment. The degree of indistinguishability of the photons is measured to be 83%.

The thesis also reports on the implementation of a new photo-ionization scheme for Barium making use of a resonant two-photon absorption process at a wavelength of 413 nm. Furthermore, the design, construction, integration and operation of a new linear ion trap for Barium is described.

Zusammenfassung

In dieser Arbeit wird von verschiedenen Experimenten zur Charakterisierung und Manipulation der Wellenfunktion eines in einer Paul-falle gespeicherten Barium Ions berichtet. Dabei werden sowohl interne (elektronische), als auch externe (Bewegungs-) Freiheitsgrade untersucht. Das Ion wird in der Paul-Falle mit Hilfe zweier Laser bei 493 nm (6 $^2S_{1/2}$ nach 6 $^2P_{1/2}$) und 650 nm (6 $^2P_{1/2}$ nach 5 $^2D_{3/2}$) bis nahe an den quantenmechanischen Bewegungsgrundzustand gekühlt und auf ca. 35 nm lokalisiert. Gestreute Photonen bei 493 nm werden im rechten Winkel zur Laserausbreitungsrichtung aufgesammelt und werden an einen Hanbury-Brown und Twiss Detektor geleitet. Dieser besteht aus einem 50/50 Strahlteiler und zwei Photonenzählern in dessen Ausgangskanälen. Der gemessene Photostrom trägt die gesamte Information über die elektronischen und die Bewegungszustände des Ions, die Analyse erfolgt sowohl im Frequenzraum als auch zeitaufgelöst durch die Messung von Korrelationsfunktionen, speziell die Korrelationsfunktion zweiter Ordnung ("Intensitäts"-korrelation).

Das wichtigste physikalische Phenomen das allen präsentierten Experimenten zu Grunde liegt, ist die Selbstinterferenz einzelner Fluoreszenz-Photonen. Realisiert wird dies durch eine Rückreflexion von Photonen, die von einer Linse innerhalb der Vakuumkammer aufgesammelt werden. Ein kollimierter Strahl aus Fluoreszenz-Photonen wird an einem Spiegel ausserhalb der Kammer zurückreflektiert. Als Folge entsteht ein Spiegelbild des Ions, dass mit dem eigentlichen Spiegelbild überlagert wird, um Eigen-Interferenz einzelner Photonen zu erzeugen.

Die hohe räumliche Auflösung des Interferenzmusters erlaubt es einerseits die Bewegung des Ions im Fallenpotential sichtbar zu machen: Durch die Oszillation wird die Resonanzfluoreszenz exakt bei der Oszillationsfrequenz moduliert. Eine Spektralanalyse des Photostroms zeigt sogenannte Bewegungsbänder als Spitzen bei der Oszillationsfrequenz. Dadurch liegt die Bewegung des Ions als elektronisches Signal vor, das nach Signalbearbeitung auf das Ion zurückgekoppelt werden kann. Es werden Experimente gezeigt, in denen man mit Hilfe solcher Rückkopplungen eine zusätzliche, rein elektronische Kühlung unter das Doppler Limit für das Ion erzeugen kann. In einer zeitlich aufgelösten Analyse des Photostromes können die Bewegungsbänder auch als Modulation der Korrelationsfunktion zweiter Ordnung auf einer Zeitskala von μs beobachtet werden. Diese Messungen werden herangezogen, um die Stabilität des Fallenpotentials zu bestimmen. Zusätzlich kann man auf kurzen Zeitskalen von ns auch die interne Dynamik des Ions beobachten.

Andererseits können mit Hilfe der Selbst-interferenz auch Experimente zur Resonator Quanten-Elektrodynamik ("cavity QED") durchgeführt werden, wobei die Güte des Resonators natürlich sehr klein ist. Es werden Messungen basierend auf der Intensitäts-Korrelationsfunktion gezeigt, in denen die relative Position des Ions in der Stehwelle der Selbst-Interferenz die Emissionswahrscheilichkeit von Photonen stark beeinflusst. Die Untersuchungen werden unter nicht- Markov'schen Bedingungen durchgeführt, also Bedingungen, bei denen Retardierungseffekte nicht vernachlässigt werden können. Erreicht wird dies durch eine entsprechend grosse Entfernung des rückreflektierenden Spiegels. Untersuchungen von "cavity QED" in diesem Regime werden hier zum ersten Male gezeigt.

Im letzten Kapitel wird ein Experiment beschrieben, bei dem aus einem einzelnes Barium Ion - eine Einzelphotonenquelle - eine Pseudo Zwei-Photonenquelle identischer Photonen erzeugt wird. Dazu wird die Fluoreszenz an einem Strahlteiler separiert und an einem 50/50 Strahlteiler wieder überlagert, um den Effekt der Zwei-Photonen Interferenz zu messen. Dadurch kann die Ununterscheidbarkeit dieser Photonen mit einem Kontrast von 83% bestimmt.

Zusätzlich zeigt diese Arbeit eine neue Methode zur Photo-ionisation von Barium mit Hilfe eines resonanten Zwei-photonen Prozess bei einer Wellenlänge von 413 nm. Weiters wird auch das Design, der Aufbau, die Integration und die Arbeitsweise einer neuen, linearen Falle für Barium Ionen beschrieben.

Contents

1 Introduction

From the beginning of natural science, the understanding of the interaction between matter and light was one of the most challenging problems. In particular the understanding of the nature of light constantly played a dominant role and was also the starting point for the development of quantum theory.

Already Descartes (1596-1650) was dealing with the nature of light and suggested light to be a "pressure transmitted through a perfectly elastic medium" [1]. Throughout the following centuries, the wave-theory of light carried by an elastic "aether" medium whose particle follow classical mechanics was the commonly accepted interpretation of light. Despite the inadequate understanding of light, many problems of optics were discovered during that time, such as the law of reflection in 1621 by Snell (1580-1626), the principle of the least time for light propagation in 1657 by Fermat (1601-1665) or the observation of the Newton rings by Boyle (1627-1691) and Hooke (1635-1703). Sir Isaac Newton (1642-1727) contributed to the understanding of the spectral composition of white light in 1666 and the understanding of the phenomenon "color". But Newton was one of the first to recognize experiments supporting a purely corpuscular theory of light. Huygens' (1629-1695) principle of elementary waves and the double-slit experiments performed in 1801 by Young (1773-1829) moreover made their contribution to the general acceptance of the wave-nature of light. It was up to MacCullagh, Faraday (1791-1867) and Maxwell (1831-1879) to develop concepts predicting the possibility of purely electromagnetic, propagating waves, without the necessity of a carrier medium, in contradiction to the aether theory. Following measurements, e.g. by Hertz (1857-1894), proved light to be an electromagnetic wave. But still, even with this new theory, in particular effects of light-matter interaction such as absorption and emission of light could not be explained sufficiently. To this end, initiated by Fraunhofer's (1787-1826) discovery of the absorption lines in the sunlight, the advent of spectroscopy as a new scientific discipline, played (and still plays) a crucial role for investigations of the atomic structure and light-matter interaction.

But even the experimental analysis could not answer the question of how light is produced and destroyed. Based on Planck's (1858-1947) introduction of energy quanta in 1900, the origin of quantum theory, Niels Bohr's (1885-1962) model of the atom could reproduce atomic spectra and thus provide an interpretation of the origin of light emission. On the other hand, Einstein interpreted Planck's energy quanta in 1905 as real light particles (the "photons") and reintroduced the concept of the particle nature of light. The concept was experimentally proved by the photo-electric effect, for which Einstein became a Nobel-laureate in 1921, and by the Compton-effect in 1923.

From that point on, the interpretation of light as a wave and as a particle became more and more accepted. It was up to the famous scientists of that decades to develop this concept and formulate it in the frame of quantum mechanics, starting with de Broglie (1892-1987) who suggested in his doctoral thesis in 1924 to apply the wave-nature to matter as well, followed by the Pauli (1869-1955) exclusion principle in 1925. Schrödinger (1867-1961) developed his wave-mechanics to describe the behavior of the particle wavefunction and Born (1882-1970) and Bohr formulated their interpretation of that results in 1927 (Copenhagen interpretation). In the same year Heisenberg (1901-1976) presented the uncertainty principle. Finally, Paul Dirac (1902-1984) introduced the Bra-Ket notation and the formalism for field quantization of electromagnetic radiation, the foundations of *quantum optics*. The developments of that decades opened an entire new era in physics.

A very big step for the overwhelming success of quantum optics was the invention of the laser. Based on an analysis of the exchange of energy between atoms and thermal radiation, Einstein already discovered the effect of stimulated emission in 1917. It took around 40 years until the concept of light amplification by stimulated emission radiation was realized with a ruby laser by Theodore Maiman in 1960. A lot of disciplines and techniques such as laser-spectroscopy or laser-cooling were born, taking benefit from the advantageous properties of laser light, the most important one being the laser's **optical coherence**. Up to that time, only Hanbury Brown and Twiss dedicated their research to optical coherence by analyzing stelar light in two-photon coincidence counting experiments. The coherence and the spectral density of laser-fields made them ideal instruments to investigate the wave-nature of light as well as light-matter interaction in a very controlled way. Rapid technical progress provided several types of laser-sources based on gas-mixtures, dyes, solid states or semiconductors covering the entire spectral range from Infra-red to deep Ultra-violet.

Almost at the same time of the invention of the laser concepts for isolating single to a few particles were worked out. Erwin Schrödinger was claiming in 1952 "*... we never experiment with just one electron or atom or (small) molecule ...*". But already one year later W. Paul invented the quadrupolar mass-filter [2]. A modification of this device became the famous Paul trap (or "high-frequency cage") for ions [3], which should allow to store charged particles over a long time.

Almost 20 years later Wineland and Dehmelt proposed schemes for cooling trapped particles [4] with the aid of laser light, before Wineland, Drullinger and Walls [5] together with Neuhauser et al. [6] were the first to report on trapping of single, laser-cooled particles in 1978 (Magnesium and Barium ions). From that time on, laser-cooled ions in a Paul trap became almost ideal systems to study fundamental properties of quantum physics, in particular the atomic structure or quantum-mechanical properties of the emitted light, as well as for investigating new frequency-standards. In the 90's on a new realm of quantum optics with trapped ions was initiated by a letter from Cirac and Zoller [7], the field of *quantum information processing* or *quantum computation* (with ions) grow. Ions, and also other well isolated systems, are thereby carrying

quantum bits, which are mostly realized by meta-stable internal states. Information writing and read-out is done with a narrow-band laser source.

While nowadays many groups world-wide are working in the field of quantum information processing with the goal of building a "quantum computer", the experiments described in this thesis are still dedicated to the fundamentals of quantum optics, in particular to the interaction of light and matter at the quantum scale, i.e. single-atom single-photon interaction. In recent years, this field became increasingly important since light-matter interfaces are the most important building blocks of a *quantum network*, a network where quantum states between distant sites [8,9] should be transferred. In this context, single atoms/ions serve as ideal quantum memory, as static quantum bits (qubits), whereas photons are ideal carriers of quantum information [10], so-called flying qubits. To this end, recent key experiments studied various aspects of atom-photon interfacing: The production of ideal photon pairs with atoms trapped in an optical cavity [11], single photon emission from a single-atom cavity system [12], entanglement of a emitted photon with a collective excitation in atomic ensembles [13,14] or real-time conditional control through a photonic channel of two distant atomic ensembles [15]. While atomic ensembles and atom-cavity systems usually don't provide optimal conditions for quantum information processing, it turned out, that single trapped ions are ideal candidates for static qubits in quantum networks offering properties such as long coherence times, long storage times, flexible state manipulation [16] and analysis schemes. A first milestone towards the interfacing of trapped ions and photons has been demonstrated by entangling the state of fluorescence photons and the internal state of a trapped ion [17,18]. Very recently, entanglement of single-atom quantum bits at a distance was shown [22].

It is thus the full characterization and control of the quantum state of a trapped ion, which allows one to observe the dynamics of the light-matter interaction at a quantum scale. In particular, the **internal dynamics**, i.e. the time-evolution of the atomic dipole, of a laser-driven single ion gives information about the interaction. It is well characterized by the statistical description of the measured stream of fluorescence photons, namely by the **second order correlation function** $g^{(2)}(\tau)$ [23]. It describes the probability of detecting a photon at time τ after detecting one at time τ=0. This intensity-intensity correlation function allows one to classify different types of light: For a single atom trapped in free space, a so-called anti-bunching is observed [24,25]. The correlation function $g^{(2)}(\tau)$ exhibits a minimum at $\tau = 0$ which indicates that the emission of a second photon immediately after the first one is very unlikely. This describes that a photon emission event projects the ion into the ground state from where it has to be re-excited. Anti-bunching can not be explained by classical physics and thus defines non-classical light. By contrast, for a large ensemble of atoms the emitted radiation exhibits classical bunching [26]. This effect can for instance be observed in a thermal light beam.

The second order correlation function can also be used to monitor the oscillations of an ion in the Paul-trap potential. They appear as modulations in the correlation

function at long time delays τ, which quantify the so-called **motional** or external states.

Another approach to quantify and control the quantum state of a system are **feedback operations**, which control the state of the system by applying a signal derived from a measurement. In the case of a quantum control, a detection, signal processing and actuation are performed by another quantum system [27], while in conventional cases of feedback, all steps are basically classic.

In this thesis experiments are described pertaining to two categories of measurements: quantum feedback and correlation measurements of resonance fluorescence. Regardless of the experimental necessities the investigations are concerned with essentially three basic components: A **single ion**, a **single photon** and a **single mirror**. *The* basic phenomenon underlying all measurements presented here is the **self-interference of single fluorescence photons**.

At the heart of the experiment is a single Barium ion stored in a Paul trap, laser-cooled by two fields at 493 nm and 650 nm and localized to within ∼35 nm. Its storage time is on the order of days to weeks. The scattered light at the wavelength of the laser-fields is investigated in either the time- or the frequency domain. It is this **resonance fluorescence** that carries all the information about both the internal and the external states of the atom and light-matter interaction. A part of the fluorescence is sent to a mirror where it is back-reflected to the ion resulting in interference, more precisely, in a self-interference of single fluorescence photons [28]. This phenomenon opened the door to new experiments dealing with cavity quantum electro dynamics (QED) in the bad cavity limit, i.e. the influence of the presence of the mirror on the internal states of the ion are weak, but measurable [29]. Additionally, the high spatial resolution of the interference standing wave enables one to measure the position of the ion and, as a consequence, to deduce the motion of the ion following a homodyne detection scheme. This technique was used to study the influence of the mirror on the external states of the ion [30], i.e. the mechanical force the mirror "exerts" on the ion. Later, the photo-current was used as a source for various types of feedback: Feedback to the oscillation phase and to the oscillation amplitude of the ion, as will be reported in this work.

The thesis is structured as follows: Chapter 2 discusses the operation principle of a generic Paul-trap focussing on different realizations, a ring-trap and a linear trap. Ion strings, their stability and oscillation modes are discussed. The next chapter, Chapter 3, summarizes the important theoretical tools such as the 8-level Bloch equations, computation of excitation spectra and the spectrum of resonance fluorescence. Furthermore, the mathematical concept of correlation functions, their applications to physics and a general discussion of classes of light is contained as well as the mathematical picture for the self-interference and the measured photo-current in a homodyne configuration.

The two subsequent chapters describe the experimental setup. Chapter 4 is focussing on the hardware consisting of two basically independent ion traps and three shared

laser-systems. The first ion-trap, a ring trap, was already built in the late 90's [31] and is still fully operational. It is referred to as the "old setup". By contrast, the "new setup" consists of a linear trap which was constructed and integrated during the work for this thesis. The operation of both traps is described in ch. 5. Using the installation and calibration measurements of the new trap system, the daily lab-routine of an experiment-preparation is described.

The discussion of the various experiments start with ch. 6, a text-book experiment for quantum feedback. The measurements described were reported in [32] and are published in [33]. Based on the self-interference, the real-time observation of the ion motion serves as a source for electronic feedback. Measurements leading to feedback cooling as well as feedback heating of the ion are described and compared to both a quantum-mechanical and a semi-classical model summarized/derived in the sub-sections before.

The following chapters are "correlation measurements of resonance fluorescence" in various regimes and setups. Chapter 7 shows investigations of the correlation function focussing on the external states of the ion. Essentially, studying modulations of the correlation function gives information on the motion of the ion, the trap stability and the phase-relation of normal modes. It is shown, that correlation measurements thus reveal the dynamics of all degrees of freedom of the ion's wave-function, on time-scales from nano- to milli-seconds.

A quite similar setup is used for the experiment presented in Chapter 8. Second order correlations of resonance fluorescence photons are measured for a big distance between the ion and the mirror, on the order of one meter. The time delay introduced by a photon round-trip is not negligible compared to the time-scales of the system and prominent memory effects appear. These measurements are the first studies of cavity QED in this regime and prove the theoretical predictions of Uwe Dorner and Peter Zoller exclusively developed for this experiment [34].

Chapter 9 deals with the phenomenon of quantum interference. Two-photon interference of resonance fluorescence photons is performed by splitting the photon stream into two channels, couple them to individual optical fibers and recombine them on a 50/50 beam splitter.

The results are summarized in Chapter 10 followed by a discussion for future prospects of this experiment.

2 Paul traps

A basic requirement for performing quantum optics experiments with a single atomic/ ionic system is the confinement of individual particles and suppression of unwanted coupling to the environment. For charged particles, Paul-traps named after W. Paul turned out to be ideal systems. All realizations of Paul-traps employ a combination of static and dynamical potentials to confine particles via the coulomb interaction. Most commonly used systems are ring traps or linear traps making use of quadrupolar potentials allowing for long storage times of up to months.

The chapter first gives an introduction into ion trapping in a very general way followed by a discussion of ring traps and linear traps, where ion strings and their properties are studied. Ion traps are extensively treated in [35], requirements for trapping ions as subjects of quantum optics experiments are studied in [36]- [38]. A detailed description of traps used in Innsbruck can be found in [31], [39]- [42] and [44].

2.1 The operating principle

Following Paul, a trap creates a quadrupolar potential which can be decomposed into a static and a dynamical, time-dependent part:

$$\begin{aligned}\Phi(x,y,z,t) &= \frac{U}{2}\,(\alpha_x x^2+\alpha_y y^2+\alpha_z z^2)\\ &+ \frac{U_{\rm rf}}{2}\,\cos(\Omega_{\rm rf}\,t)(\alpha'_x x^2+\alpha'_y y^2+\alpha'_z z^2),\end{aligned}\tag{2.1}$$

where U is a D.C. voltage and $U_{\rm rf}$ denotes the amplitude of the radio-frequency voltage with $\Omega_{\rm rf}$. The parameters $\alpha_i^{(')}$ describe the geometry. The potential has to fulfill the Laplace equation, $\Delta\Phi = 0$, leading to restrictions for the geometric factors

$$\begin{aligned}\alpha_x+\alpha_y+\alpha_z &= 0\\ \alpha'_x+\alpha'_y+\alpha'_z &= 0.\end{aligned}\tag{2.2}$$

From that it is obvious that a charged particle can only be trapped in all dimensions by a superposition of static and dynamic potentials. The choice of the geometric parameters allows one to describe different kinds of traps studied below.

The motion of a single charged particle in a quadrupolar potential is decoupled in the spatial coordinates and the classical equation of motion is given by the Mathieu

differential equation. In one direction r_i $(i = x, y, z)$ one finds

$$\frac{d^2 r_i}{d\xi^2} + [a_i - 2q_i \cos(2\xi)] r_i = 0, \tag{2.3}$$

where

$$\xi = \frac{\Omega_{\mathrm{rf}} t}{2}, \qquad a_i = \frac{4|e|U\alpha_i}{m\Omega_{\mathrm{rf}}^2}, \qquad q_i = \frac{2|e|U_{\mathrm{rf}}\alpha_i'}{m\Omega_{\mathrm{rf}}^2} \ . \tag{2.4}$$

The variables a_i and q_i are the stability parameters defining regions in the (a_i,q_i) space, where stable solutions of the differential equations of motion exist. Stable solutions in a mathematical sense are associated with stable trajectories of a charged particle in the dynamical potential. In lowest-order approximation, ($|a_i|$, $q_i^2 \ll 1$), the ion trajectory can be found as

$$r_i(t) \ \propto \ \cos(\omega_i t) \left(1 - \frac{q_i}{2} \ \cos(\Omega_{\mathrm{rf}} t)\right), \tag{2.5}$$

where

$$\omega_i = \beta_i \frac{\Omega_{\mathrm{rf}}}{2}, \qquad \beta_i = \sqrt{a_i + \frac{q_i^2}{2}}. \tag{2.6}$$

Thus the motion of the ion along one direction consists of two parts, one oscillating at the frequency $\omega_i \ll \Omega_{\mathrm{rf}}$ (for $\beta_i \ll 1$) called *secular motion* and one oscillation at the driving frequency Ω_{rf} with an amplitude reduced by a factor of $q_i/2$ and therefore called *micromotion*. In most of the experimental situations the micromotion part can be neglected and the trajectory of the ion in all three dimensions is a harmonic oscillation with frequencies ω_i in a so-called pseudo-potential Ψ (secular approximation) with

$$e\Psi = \frac{1}{2} \ m \sum_i \omega_i^2 r_i^2 \ . \tag{2.7}$$

The depth of the pseudo-potential well is determined by

$$D_i = \frac{1}{2} \ m\omega_i^2 r_{0,i}^2 \ , \tag{2.8}$$

where $r_{0,i}^2$ is the electrode to trap-center distance. Typical well depths are on the order of tens of eV, thus making loading from a thermal beam of atoms possible.

Trapped ions are typically confined at a final temperature given by the environment, i.e. 300 K. This "high" kinetic energy of the ion can be reduced by laser cooling. A semiclassical discussion of this process can be found in [48]. Laser cooling benefits from a net momentum transfer during absorption of photons with a directed momentum and spontaneously emitted photons with random momentum direction. The process is able to cool the motion such that their kinetic energy becomes comparable to $\hbar\omega_i$, the motional energy quantum. For a quantum description one defines creation and

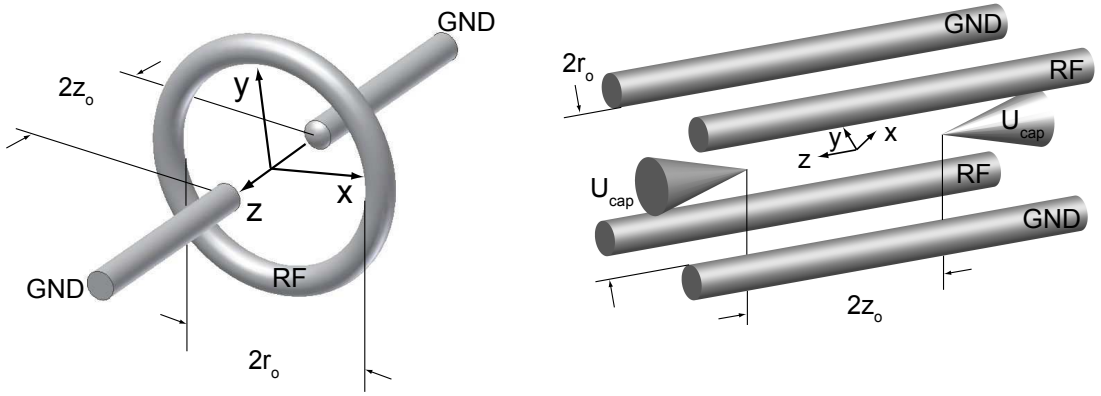

Figure 2.1: Realizations of Paul traps: *Left:* A radiofrequency (RF) applied to a ring with $2r_0$ diameter and two tips at a distance $2z_0$ held at ground potential (GND) form a 3D dynamical confinement. *Right:* Four rods with a diagonal spacing of $2r_0$ and a pairwise applied RF-voltage form a two-dimensional dynamical potential along the z-axis. Two electrodes held at a static potential of U_{cap} 'close' the linear configuration in the z-direction.

annihilation operators ($\hat{r}_i$...position, $\hat{p}_i$...momentum) for the trapped ion [39]:

$$\begin{aligned}\hat{a}^\dagger_{m_i} &= \sqrt{\frac{m\omega_i}{2\hbar}}\ \hat{r}_i + \frac{i}{\sqrt{2m\hbar\omega_i}}\ \hat{p}_i \\ \hat{a}_{m_i} &= \sqrt{\frac{m\omega_i}{2\hbar}}\ \hat{r}_i - \frac{i}{\sqrt{2m\hbar\omega_i}}\ \hat{p}_i\end{aligned} \tag{2.9}$$

The Hamiltonian of this system is

$$\begin{aligned}H = \sum_i \frac{p_i^2}{2m} + \frac{1}{2}m\omega_i^2 r_i^2 = ... &= \sum_i \hbar\omega_i \left(\hat{a}^\dagger_{m_i}\hat{a}_{m_i} + \frac{1}{2}\right) \\ &= \sum_i \hbar\omega_i \left(\hat{n}_i + \frac{1}{2}\right),\end{aligned} \tag{2.10}$$

where $\hat{n}_i$ is the number operator of the harmonic oscillation in the trapping potential. The spread of the wave function of the state with $\langle\hat{n}\rangle = n$ is then given by

$$\langle n|\hat{r}_i|n\rangle^{\frac{1}{2}} = \langle 0|\hat{r}_i|0\rangle^{\frac{1}{2}}\ \sqrt{2n+1} = \sqrt{\frac{\hbar}{2m\omega_i}}\ \sqrt{2n+1}, \tag{2.11}$$

with $\sqrt{\hbar/(2m\omega_i)}$ being the spread of the ground state wave function. For a trapped Barium ion with secular frequency of $\omega_i/2\pi = 1\,\mathrm{MHz}$ the ground state wave packet is $\approx 6\,\mathrm{nm}$, for $n = 15$ the ground state wave packet is $\approx 35\,\mathrm{nm}$.

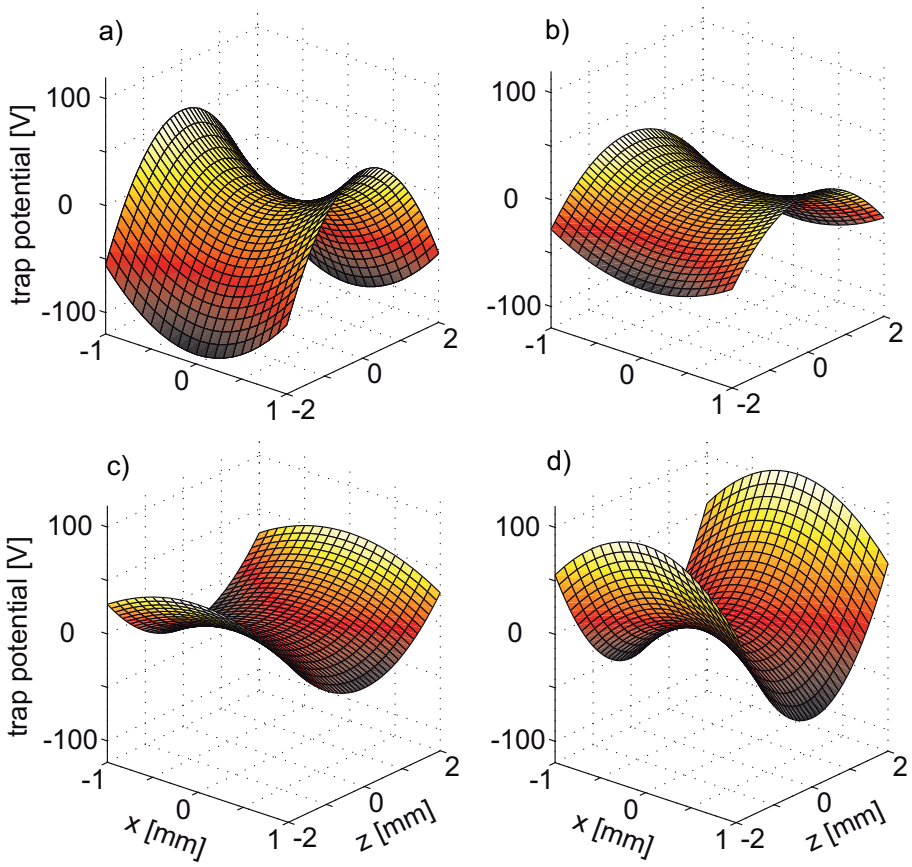

Figure 2.2: Dynamical trapping potential in the ring trap from Eq. (2.12) for different phases $\Omega_{\mathrm{rf}}t = 0,\ \pi/3,\ 2\pi/3,\ \pi$ in a), b), c) and d). Note the stronger confinement in the z direction.

2.2 The Ring Trap

One possible realization of a Paul trap is to use a ring with diameter $2r_0$ and two tips along the z-axis with a distance of $2z_0$, typically on the order of millimeters. The left panel in Fig. 2.1 shows such a configuration. Secular motion in the ring plane along the x- and y-axis (z-axis) are called radial (axial) modes. For such a system the geometrical parameters are [36] $\alpha_x = \alpha'_x = \alpha_y = \alpha'_y = -2\alpha_z = -2\alpha'_z$ and $\alpha_x = 2/(r_0^2 + 2z_0^2)$, thus this configuration allows dynamical trapping in all three dimensions. For a choice of $U = 0$, a merely dynamical trapping potential is obtained

$$\Phi(x, y, z, t) = \frac{U_{\mathrm{rf}}}{r_0^2 + 2z_0^2}\ \cos(\Omega_{\mathrm{rf}}\ t)(x^2 + y^2 - \frac{1}{2}\ z^2). \tag{2.12}$$

The shape of such a potential is depicted in Fig. 2.2. For a given time t, the saddle-potential confines the ion in one direction, e.g. in the x-direction in panel a). In panel

d) the confinement is just in the z-direction. For a saddle-potential whose oscillating frequency is "fast enough", the ion is kept in an effective pseudo-potential as described above. "Fast enough" in this respect is described by proper stability parameters including the mass, charge, the geometry of the trap and the radio-frequency properties. For the choice of $U = 0$, $a_i = 0$ and

$$q_x = q_y = \frac{2|e|U_{\mathrm{rf}}}{m(r_0^2 + 2z_0^2)\Omega_{\mathrm{rf}}^2} \qquad q_z = -2q_x \tag{2.13}$$

$$\beta_x = \beta_y = \frac{1}{\sqrt{2}}\, q_x \qquad \beta_z = \frac{1}{\sqrt{2}}\, q_z = -\frac{2}{\sqrt{2}}\, q_x\ . \tag{2.14}$$

In the lowest stability region defined by $0 < q \lesssim 0.9$, a charged particle oscillates along the x, y and z axis with frequencies

$$\omega_x = \omega_y = \frac{q_x \Omega_{\mathrm{rf}}}{2\sqrt{2}} \qquad \omega_z = \frac{|q_z|\Omega_{\mathrm{rf}}}{2\sqrt{2}} = \frac{q_x \Omega_{\mathrm{rf}}}{\sqrt{2}}. \tag{2.15}$$

For typical values of $q \sim 0.3$, the radial oscillation frequencies are $\omega_x = \omega_y \approx 10\%\ \Omega_{\mathrm{rf}}$, the axial frequency are $\omega_z \approx 20\%\ \Omega_{\mathrm{rf}}$.

Since a_i is vanishing for $U = 0$, the radial oscillation frequencies are degenerate. However, experiments mostly show slightly different frequencies of the two radial modes, which is due to geometrical imperfections of the trap. A frequency measurement can quantify this effect.

2.3 The linear Trap

Another possible realization is an electrode configuration displayed in the right panel of Fig. 2.2. It consists of 4 rods, where one diagonal pair is connected to a DC-potential, mostly to ground-potential, and the second pair to a radio-frequency source. Two endcaps close the potential at the end of this linear configuration with the aid of DC potentials (U_{cap}). The confinement is thus realized with a dynamical potential in the two radial directions x and y and with a static potential in the axial direction z. The geometry parameters fulfill [36] $\alpha'_x = -\alpha'_y$ and $\alpha'_z = 0$ yielding a potential

$$\Phi(x, y, z, t) = \frac{U_{\mathrm{rf}}}{r_0^2}\ cos(\Omega_{\mathrm{rf}}\ t)(x^2 - y^2), \tag{2.16}$$

where $U = 0$ as before and $2r_0$ is the distance between two diagonal electrodes. The potential parameters are

$$q_x = -q_y = \frac{2|e|U_{\mathrm{rf}}}{mr_0^2\Omega_{\mathrm{rf}}^2} \qquad q_z = 0 \tag{2.17}$$

$$\beta_x = -\beta_y = \frac{q_x}{\sqrt{2}} \qquad \beta_z = 0. \tag{2.18}$$

The secular motion in the radial direction reads

$$\omega_x = \omega_y = \frac{q_x \Omega_{\mathrm{rf}}}{2\sqrt{2}} \ , \tag{2.19}$$

as before. In the axial direction z the ion is confined by applying a voltage U_{cap} to the endcaps. A harmonic potential is assumed following

$$\frac{1}{2} m \omega_z^2 z_0^2 = \kappa e U_{\mathrm{cap}}, \tag{2.20}$$

where z_0 is the half distance between the end caps and κ is a geometry factor describing the penetration of the field at the trap center. The axial motion thus is

$$\omega_z = \sqrt{\frac{2\kappa e U_{\mathrm{cap}}}{m z_0^2}}, \tag{2.21}$$

and is independent of the confinement in the radial direction. The pseudo potential, however, is slightly weakened by the defocusing effect of the axial confinement, such that the radial frequencies are modified:

$$\omega_{x,y} \rightarrow \omega'_{x,y} = \sqrt{\omega_{x,y}^2 - \frac{1}{2}\omega_z^2}. \tag{2.22}$$

Anyway, this effect is usually on the order of some percent and can be neglected for the experiments performed in this work.

2.3.1 Ion crystals in a linear trap and equilibrium postions

The linear trap configuration is in particular advantageous for storing more than one ion without exhibiting additional micro-motion. Detailed studies of ion strings in linear Paul traps can be found in in [37], [46] and [47]. For a radial confinement stronger than the axial confinement, the ions are forming linear strings. In such a case the ions "see" the axial harmonic potential and the repulsive coulomb potential of other ions. Denoting the equilibrium positions of the ions with z_m and z_n one obtains [37]

$$\Psi' = \sum_{m=1}^{N} \frac{m}{2} \omega_z^2 z_m^2 + \sum_{n,m=1, n\neq m}^{N} \frac{e^2}{8\pi\epsilon_0} \frac{1}{|z_m - z_n|} \ . \tag{2.23}$$

The N ions arrange themselves at equilibrium positions $z_m^{(0)}$, where the potential has its minimum, i.e.

$$\left[\frac{\partial \Psi'}{\partial z_m}\right]_{z_m = z_m^{(0)}} = 0, \tag{2.24}$$

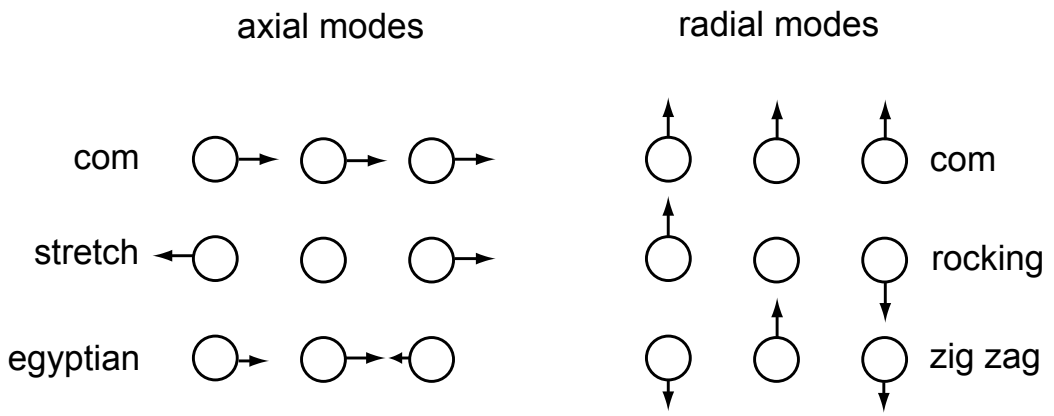

Figure 2.3: Oscillation modes of a three ion crystal in axial and radial direction. The principal mode is the center-of-mass mode (COM).

This equation can be solved analytically for $N = 2$ and $N = 3$, for higher N numerically. Setting the trap center at $z = 0$, the equilibrium postions of N ions are

$$\begin{aligned} N &= 2: & -\left(\frac{1}{2}\right)^{2/3} l & & \left(\frac{1}{2}\right)^{2/3} l & \\ N &= 3: & -\left(\frac{5}{4}\right)^{1/3} l & 0 & \left(\frac{5}{4}\right)^{1/3} l & \\ N &= 4: & -1.44\, l & -0.45\, l & 0.45\, l & 1.44\, l \end{aligned} \tag{2.25}$$

where

$$l = \left(\frac{e^2}{4\pi\epsilon_0 M\omega_z^2}\right)^{(1/3)} \tag{2.26}$$

is the characteristic length of the trap. For typical values of $\omega_z = 2\pi \cdot 1\,\mathrm{MHz}$ and using Barium atoms $l \sim 2.9\,\mu\mathrm{m}$ yielding an ion distance of $\Delta z = 3.7\ \mu\mathrm{m}$ for $N = 2$ and $\Delta z = 3.2\ \mu\mathrm{m}$ for $N = 3$ ions.

2.3.2 Normal modes of oscillation

The individual ions in a crystal oscillate about their equilibrium positions

$$z_m(t) = z_m(0) + q_m(t). \tag{2.27}$$

The oscillations take place in the radial and the axial direction and are shared by all ions since the Coulomb interaction provides a coupling among them. They are called

common modes or also bus-modes for quantum computation purposes. The system behaves similar to masses coupled by springs, where either the center-of-mass is oscillating, but the relative distance of the ions stays constant (center-of-mass mode, COM) or vice versa (breathing or rocking mode). Additionally, there exists an intermediate oscillation scheme called axial egyptian and radial zig zag mode. Figure 2.3 gives an overview of the different oscillation types. The oscillation frequencies of the center-of-mass modes are in both the radial and the axial directions identical to the single ion frequencies shown above[1]. Extensive studies of other oscillations in linear traps can for instance be found in [41, 42].

2.3.3 Stability of normal modes

The ions just form a linear string, if the radial confinement is much stronger than the axial. If this condition is violated a linear-to-zig-zag phase transition in the ionic crystal takes place. Indeed, micro-motion and thus excessive heating appears and disturbs ideal measurement conditions. From Ref. [45] and [46] one finds

$$\left(\frac{\omega_z}{\omega_{x,y}}\right)^2_{crit} = \alpha N^\beta, \tag{2.28}$$

where $\alpha = 2.53$ and $\beta = -1.73$ are determined using simulations [45]. This formula is valid for ion numbers N up to 1000 and can be used to estimate the axial frequency while observing the phase transition, such that

$$\omega_z = \sqrt{\alpha N^\beta}\ \ \omega_{x,y}. \tag{2.29}$$

For instance, for a measured radial frequency of $\omega_{x,y}/2\pi$=1 MHz of a crystal with three ions, a phase-transition takes place at at an axial frequency of $\omega_{x,y}/2\pi \approx 620$ kHz, for a 5 ion crystal at $\omega_{x,y}/2\pi \approx 400$ kHz. Note that the experiments (simulations) performed in Ref. [46] yield $\alpha = 3.23\ ^{+0.06}_{-0.2}$ (2.94 ± 0.07) and $\beta = -1.83 \pm 0.04$ (-1.80 ± 0.01).

[1] This approximation does not hold for very large ion numbers $N > 10$, where the oscillation frequency depends on the number of ions.

3 Light-matter interaction

3.1 The Barium ion

Neutral Barium (Gr. *barys*, heavy) is a soft and metallic element which belongs to the earth alkaline group. It oxidizes very easily and is only found in combination with other elements. It is used as a getter in vacuum tubes. Besides the 7 stable isotopes listed in table 3.1 39 radioactive isotopes and isomers are known to exist.

The single ionized Barium, especially $^{138}Ba^{+}$, played an important role in the history of ion trap experiments. It was one of the first atomic ions trapped and observed. Several properties of Barium 138 make this element suitable for ion trapping: The electron configuration is the one of Xenon with an additional electron in the $6^2S_{1/2}$ state yielding an alkaline-like level-scheme. Additionally, due to the vanishing nuclear spin, $I = 0$, the level scheme does not exhibit any hyperfine splitting. While not all wavelengths for addressing the five lowest lying levels (Fig. 3.1) are easy to produce, the relevant electronic transitions for an efficient laser-cooling are in the visible range (see Fig. 3.2), thus easy to handle and to detect. The three relevant levels form a Λ configuration depicted in Fig. 3.2 a). Furthermore, the weight of Barium makes it resistant to background collisions in a vacuum environment and allows for longer storage times.

The generic three-level system is converted into an effective 8-level system when a weak magnetic field is applied. The electronic states split up according to the Zeeman effect and the level schemes become more involved. In all measurements presented in this work, a geometrical configuration was used, where the polarization (linear) and the propagation direction is perpendicular to the magnetic field axis.

In the following, a summary of the formalism of the optical Bloch equations is given to be able to make predictions for the photon emission properties and statistics of a laser driven single Barium ion.

Isotope	^{130}Ba	^{132}Ba	^{134}Ba	^{135}Ba	^{136}Ba	^{137}Ba	^{138}Ba
nuclear spin I in $\hbar$	0	0	0	3/2	0	3/2	0
abundance in %	0.1	0.1	2.4	6.6	7.3	11.3	71.7

Table 3.1: Stable Barium isotopes and their natural abundance [49, 50].

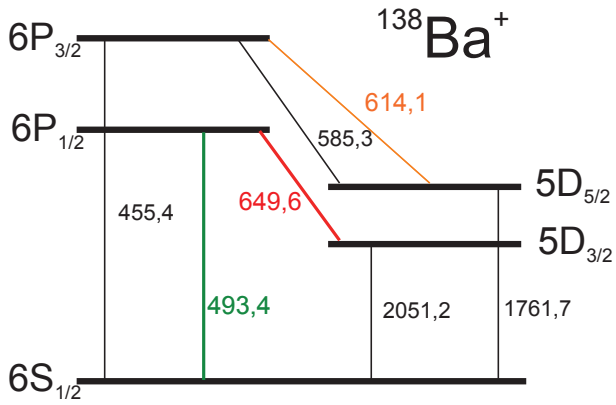

Figure 3.1: Scheme of the lowest atomic levels in $^{138}Ba^{+}$. Wavelengths are given in nano-meters [50].

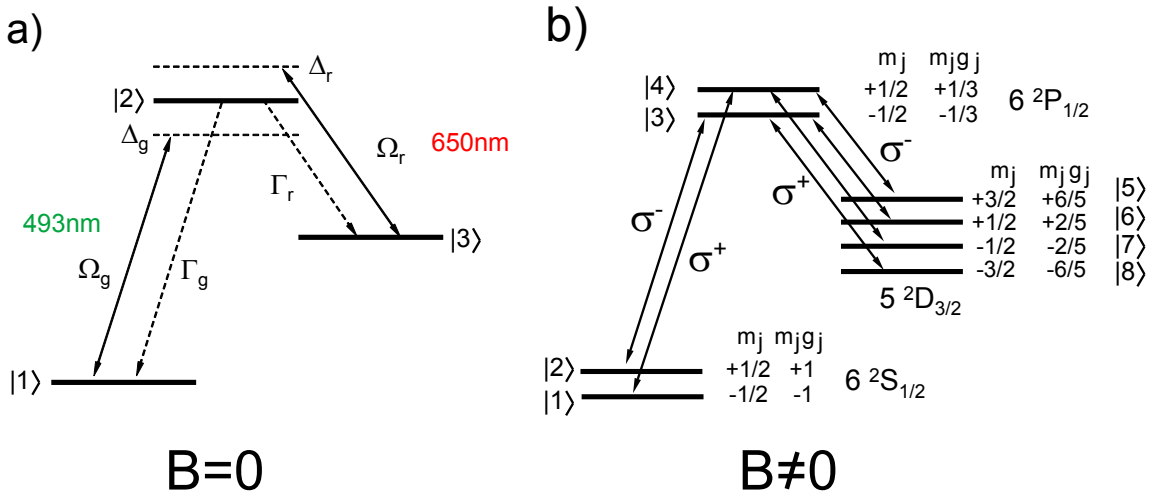

Figure 3.2: Relevant levels and transition wavelengths for Ba^{+}. Figure a) defines the notation used for the Bloch equations. A weak magnetic field B lifts the energetic degeneracy of the Zeeman substates and thus creates an 8 level system depicted in Fig. b). Possible transitions are shown for a linear polarization of the light field perpendicular to the magnetic field applied.

transition	λ_{air} [nm]	Γ_{nat} [MHz]	A [10^8 s^{-1}]
$6^2S_{1/2} \longleftrightarrow 6^2P_{1/2}$	493.4007	15.1	0.953
$6^2P_{1/2} \longleftrightarrow 5^2D_{3/2}$	649.898	5.3	0.310

Table 3.2: The relevant transitions in the Barium ion, the transition wavelengths, natural linewidths and the Einstein coefficients [50].

3.2 The Bloch equations

The source for all experiments described in this thesis is the radiation emitted by a laser-excited ion. Thus, in the following chapter a description of the interaction of an atom and two laserfields in terms of the Bloch equations is given. For clarity the dynamics of a *three*-level system is studied before extending the model to the realistic *eight*-level system. Figure 3.2 is illustrating the notations used. A general analysis of this problem can for instance be found in [23] or in [51], while an analysis applied to Barium ions is found in [52].

The Hamiltonian: Atom, light field and dipole interaction

The complete Hamiltonian of this system consists of three parts describing the atom, the field and the interaction between them:

$$\hat{\mathcal{H}} = \hat{\mathcal{H}}_{atom} + \hat{\mathcal{H}}_{field} + \hat{\mathcal{H}}_{int}. \tag{3.1}$$

The atomic Hamiltonian fulfills the equation

$$\hat{\mathcal{H}}_{atom}|a\rangle = \hbar\omega_a|a\rangle, \tag{3.2}$$

where $|a\rangle$ are the atomic eigenvectors denoted with $a = 1, 2, 3$ for a three-level system ($6^2S_{1/2}$, $6^2P_{1/2}$ and $5^2D_{3/2}$ in the case of the Ba^+) and ω_a are the atomic Bohr frequencies. $\hat{\mathcal{H}}_{atom}$ then reads

$$\hat{\mathcal{H}}_{atom} = \sum_{a=1}^{3} |a\rangle\langle a|\hbar\omega_a \tag{3.3}$$

and can be written in a matrix representation with respect to the basis $a = 1, 2, 3 \rightarrow (1, 0, 0)$, $(0, 1, 0)$ and $(0, 0, 1)$ leading to

$$\hat{\mathcal{H}}_{atom} = \hbar \begin{pmatrix} \omega_1 & 0 & 0 \\ 0 & \omega_2 & 0 \\ 0 & 0 & \omega_3 \end{pmatrix}. \tag{3.4}$$

The zero point of the energy is chosen at the level $|2\rangle$ which modifies the Hamiltonian to:

$$\hat{\mathcal{H}}_{atom} = \hbar \begin{pmatrix} \omega_1 - \omega_2 & 0 & 0 \\ 0 & 0 & 0 \\ 0 & 0 & \omega_3 - \omega_2 \end{pmatrix}. \tag{3.5}$$

The atom is coupled to two laser fields at 493 nm and 650 nm driving the $|1\rangle$ to $|2\rangle$ and $|3\rangle$ to $|2\rangle$ transitions, respectively. The laser field is described as a classical monochromatic wave,

$$\vec{E_g}(t) = \Re\ (E_{g0}\ e^{-i\omega_g t}) \cdot \vec{\epsilon_g}, \qquad \vec{E_r}(t) = \Re\ (E_{r0}\ e^{-i\omega_r t}) \cdot \vec{\epsilon_r}. \tag{3.6}$$

Here, the index g describes the laser field at 493 nm (green) and r describes the transition at 650 nm (red). E_{g0} is the amplitude, $\vec{\epsilon_g}$ the polarization vector and ω_g the angular frequency.

In the following it is assumed that the laser fields only interact with the electric dipole moment of the atom (dipole approximation), higher order electric or magnetic moments are neglected. The interaction Hamiltonian under this assumption reads

$$\hat{\mathcal{H}}_{int} = -\vec{D} \cdot \vec{E}, \tag{3.7}$$

where $\vec{D}$ represents the atomic dipole operator. Since the transition from state $|1\rangle$ to $|3\rangle$ is dipole forbidden the state $|3\rangle$ is assumed to be stable and the atom-laser interaction can be written in the matrix representation

$$\hat{\mathcal{H}}_{int} = \hbar \begin{pmatrix} 0 & \frac{\Omega_g}{2} e^{+i\omega_g t} & 0 \\ \frac{\Omega_g}{2} e^{-i\omega_g t} & 0 & \frac{\Omega_r}{2} e^{-i\omega_r t} \\ 0 & \frac{\Omega_r}{2} e^{+i\omega_r t} & 0 \end{pmatrix}, \tag{3.8}$$

where

$$\hbar\Omega_g := \vec{\epsilon_g} \cdot \vec{D_g} \cdot E_{0g} \qquad \hbar\Omega_r := \vec{\epsilon_r} \cdot \vec{D_r} \cdot E_{0r}. \tag{3.9}$$

The frequency $\Omega_{g(r)}$ are the Rabi frequencies and describe the coupling strength between the atom and the field. For simplicity the Rabi frequency can be expressed in terms of the saturation parameters S_i,

$$S_g = \frac{\Omega_g}{\Gamma_g} \qquad S_r = \frac{\Omega_r}{\Gamma_r}\ . \tag{3.10}$$

Finally, the complete "coherent Hamiltonian" in matrix representation reads:

$$\hat{\mathcal{H}} = \hbar \begin{pmatrix} \omega_1 - \omega_2 & \frac{\Omega_g}{2} e^{+i\omega_g t} & 0 \\ \frac{\Omega_g}{2} e^{-i\omega_g t} & 0 & \frac{\Omega_r}{2} e^{-i\omega_r t} \\ 0 & \frac{\Omega_r}{2} e^{+i\omega_r t} & \omega_3 - \omega_2 \end{pmatrix}. \tag{3.11}$$

Applying a unitary transformation is changing into a frame rotating at the laser frequencies. In the matrix representation the transformation reads:

$$U = \begin{pmatrix} e^{-i\omega_g t} & 0 & 0 \\ 0 & 1 & 0 \\ 0 & 0 & e^{-i\omega_r t} \end{pmatrix}. \tag{3.12}$$

Performing the transformation modifies the Hamiltonian resulting in a final and simplified Hamiltonian for the three-level system coupled to two laser fields

$$\hat{\mathcal{H}}' = \begin{pmatrix} \Delta_g & \frac{\Omega_g}{2} & 0 \\ \frac{\Omega_g}{2} & 0 & \frac{\Omega_r}{2} \\ 0 & \frac{\Omega_r}{2} & \Delta_r \end{pmatrix}, \tag{3.13}$$

where the abbreviations are introduced according to the atomic Bohr frequencies:

$$\Delta_g = \omega_g - (\omega_2 - \omega_1), \qquad \Delta_r = \omega_r - (\omega_2 - \omega_3). \tag{3.14}$$

Density operator formalism, spontaneous decay

Up to now, spontaneous decay of the state $|2\rangle$ or other decoherent effects were not considered. Since the system is no longer in a pure state, the density matrix formalism is used. The atomic density operator in the basis $|a\rangle$ reads

$$\hat{\rho} = \sum_{a,b=1,2,3} \rho_{a,b} |a\rangle\langle b|. \tag{3.15}$$

Diagonal elements of the density operator ($\hat{\rho_{ii}}...i = 1, 2, 3$) are the expectation values for finding the ion in one of the states (occupation probability) and thus $Trace(\hat{\rho}) = 1$. The off-diagonal elements describe coherences, i.e. superpositions of quantum states.

The dynamics of the system is described by the equation of motion for the density operator, i.e. the Master (Liouville) equation. Dissipative processes, such as spontanous decay or finite laser linewidths, have to be described as a coupling to reservoirs, the system transforms into an open system. However, it can be shown, that the master-equtions in Lindblad-form is the trace-preserving description for dissipative systems and reads

$$\frac{d\rho'}{dt} = -\frac{i}{\hbar}[\mathcal{H}', \rho'] + \mathcal{L}_{damp}(\rho). \tag{3.16}$$

where the density matrix is written in the rotating frame. The second term in this equation describes all possible damping terms and reads

$$\mathcal{L}_{damp}(\rho) = -\frac{1}{2}\sum_m [\hat{C}_m^\dagger \hat{C}_m \rho + \rho \hat{C}_m^\dagger C_m - 2\hat{C_m} \rho \hat{C}_m^\dagger]. \tag{3.17}$$

For a three-level atom, the $\mathcal{L}_{damp}(\rho)$ - term describes the damping introduced by spontaneous emission as a rate times a projector for the transition, i.e.

$$\hat{C}_g = \sqrt{\Gamma_g}|1\rangle\langle 2| \qquad \hat{C}_r = \sqrt{\Gamma_r}|3\rangle\langle 2|, \tag{3.18}$$

and the finite laser linewidth introduced by the operators:

$$\hat{C}_{lg} = \sqrt{\delta_{lg}}|1\rangle\langle 1| \qquad \hat{C}_{lr} = \sqrt{\delta_{lr}}|3\rangle\langle 3|, \tag{3.19}$$

where δ_{lg} and δ_{lr} describes the laser linewidths of the green and the red laser respectively. In summary, the $\hat{C}_m$ operators allow one to include all incoherent processes like spontaneous emission and finite laser linewidths.

Bloch equations

The final Hamiltonian, the density operator ρ' and the damping terms[1] $\mathcal{L}_{damp}$ can now be inserted into Eq. (3.16). Matrix multiplication leads to a set of linear equations (the optical Bloch equations) of the form

$$\dot{\overrightarrow{\rho_i}} = \sum_j M_{ij} \overrightarrow{\rho_i}, \tag{3.20}$$

where the density operator is transformed into a vector

$$\overrightarrow{\rho} = (\rho_{11}, \rho_{12}, ..., \rho_{87}, \rho_{88}). \tag{3.21}$$

This system of linear equations has a unique solution,

$$\overrightarrow{\rho}(t) = \exp(Mt)\overrightarrow{\rho}(0), \tag{3.22}$$

where $\overrightarrow{\rho}(0)$ describes the initial condition, e.g. the atom is in the groundstate at $t = 0 \rightarrow \rho_{11}(0) = 1, \rho_{22}(0) = 0$, and $\rho_{33}(0) = 0$. Here a normalization is introduced, such that the sum of occupation probabilities equals one for all times, i.e.

$$\sum_i = \rho_{ii} = 1 \quad \forall t. \tag{3.23}$$

Moreover, for deriving excitation spectra only the steady state solution is of interest, where $\rho(\infty) = \text{const}$ and $\dot{\rho} = 0$. For the solution one of the Bloch equations is replaced due to the normalization condition (3.23) and the system of equations

$$0 = \sum_j M_{ij} \overrightarrow{\rho_i}, \tag{3.24}$$

can be solved by diagonalizing the Matrix on the right side numerically (or analytically in certain cases).

3.3 Excitation spectroscopy

3.3.1 Three-level system

Excitation spectroscopy is performed by recording fluorescence photons as a function of the detuning of one cooling laser. With the three-level system given in Fig. 3.2 a) the excited state $|2\rangle$ decays either into the ground state $|1\rangle$ associated with an emission of a green photon at 493 nm or into the metastable state $|3\rangle$ together with an emission

[1] The damping terms remain unchanged under the transformation.

of a red photon at 650 nm. The total rate of photon emission, N_{tot}, is proportional to the population of the excited state ρ_{22}, such that

$$N_{tot} \;=\; \Gamma_g\ \rho_{22} + \Gamma_r\ \rho_{22}. \tag{3.25}$$

In a photon counting experiment different filters select the desired photon wavelength, normally in our experiment the green fluorescence is investigated. Count rates are typically measured within a time window of 100 ms up to 1 s. This justifies an evaluation of the excited state population in the steady state limit, where $\dot{\rho}_{ii}(t) \equiv 0$, since $1/\Gamma_{r,g} \cong 10 - 1000$ ns.

Figure 3.3 shows such an evaluation of the excited state population ρ_{22} in the steady state limit plotted as a function of the detuning of the repumping 650 nm laser, while the detuning of the cooling laser at 493 nm is kept constant. This excitation spectrum[2] of a three-level Λ system shows a prominent dip occurring at equal detuning of the driving laser fields, i.e. $\Delta_g = \Delta_r$. Apparently, with such conditions the population of the excited state vanishes and the ion does not emit photons. This feature is called dark resonance and is understood as the creation of a coherent superposition of the states $|1\rangle$ and $|3\rangle$. The Bloch equations can be solved analytically and yield a density operator in the steady state

$$\rho_{ss} = \begin{pmatrix} \frac{\Omega_r^2}{\Omega_r^2+\Omega_g^2} & 0 & \frac{-\Omega_r^2\Omega_g^2}{\Omega_r^2+\Omega_g^2} \\ 0 & 0 & 0 \\ \frac{-\Omega_r^2\Omega_g^2}{\Omega_r^2+\Omega_g^2} & 0 & \frac{\Omega_g^2}{\Omega_r^2+\Omega_g^2} \end{pmatrix}. \tag{3.26}$$

As expected, the population of the excited state, ρ_{22}, vanishes. States $|1\rangle$ and $|3\rangle$ share the population (see middle plot of Fig. 3.3) and the non-vanishing off- diagonal elements show the coherent oscillations between the two states. For ideal conditions, i.e. vanishing laserlinewidths, the dark resonance dip should go down to zero. This is not true for a finite linewidth of the driving laser fields, such that dark resonances are a good measure for the latter.

3.3.2 Eight-level system

The three-level system discussed so far is mainly of academic interest for the measurements presented in the frame of this work. In an experimental situation, weak magnetic fields are applied to prevent optical pumping into the extreme Zeeman states $|D_{3/2}, m_F = \pm 3/2\rangle$ and to define the quantization axis. The magnetic field lifts the degeneracy of the electronic states and splits up the Zeeman substates resulting in an 8-level scheme (Fig. 3.2). As a consequence, the number and the position of the dark

[2]The shape of the spectrum is identical for measuring green or red photons. However, the count rates scale according to Eq.(3.25).

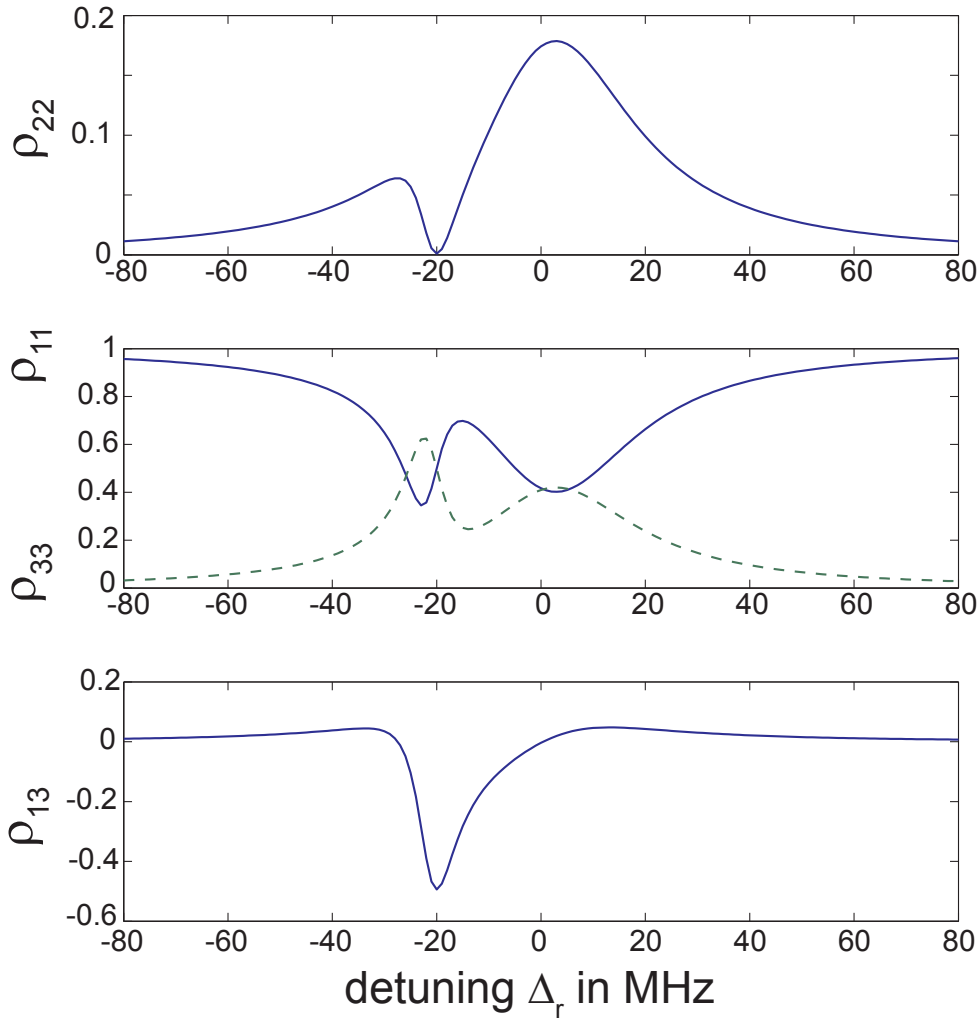

Figure 3.3: Excitation spectrum for a three-level system calculated from the Bloch equations. The parameters are chosen for typical experimental conditions: $S_g = 1, S_r = 3, \Delta_g/2\pi = -20\,\mathrm{MHz}, \delta_{\mathrm{l}}\mathrm{g}/2\pi = \delta_{\mathrm{l}}\mathrm{r}/2\pi = 10\,\mathrm{kHz}$.

resonances changes with respect to the three-level system and depends on the angle between the magnetic field and the polarization of the laser field.

The optical Bloch equations can be generalized to an eight-level system, but become involved. The magnetic field enters the model through

$$u = \frac{\mu_B |\vec{B}|}{\hbar}, \qquad \Delta\omega_{Zee} = m_j g_j u, \tag{3.27}$$

with the Bohr magneton μ_B and the Zeeman splitting $\Delta\omega_{Zee}$ of the substates in frequency units. Following the same formalism a detailed analysis is given in [52].

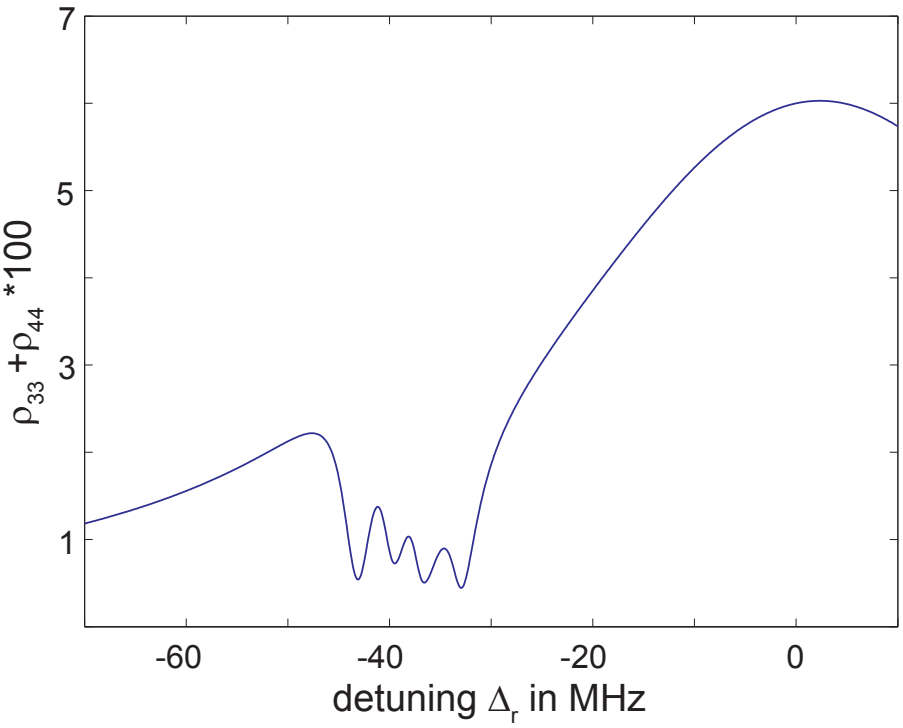

Figure 3.4: Excitation spectrum for a single Ba^+ ion calculated from the eight-level Bloch equations. The parameters are chosen for typical experimental conditions: $S_g = 1.15, S_r = 2.2, \Delta_g/2\pi = -25\,\mathrm{MHz}, \delta_\mathrm{lg}/2\pi = \delta_\mathrm{lr}/2\pi = 40\,\mathrm{kHz}, \mathrm{u}/2\pi = 2.3\,\mathrm{MHz}, \alpha = 95°$.

Similar to the three-level system excitation spectra can be obtained by evaluating the population (see Fig. 3.2 b)) of the excited states $|3\rangle = |P_{1/2}, m_F = -1/2\rangle$ and $|4\rangle = |P_{1/2}, m_F = 1/2\rangle$ in the steady state limit as a function of the laser detuning. The measured photon emission rate is thus proportional to

$$N_{tot,8L} \propto \rho_{33} + \rho_{44}. \tag{3.28}$$

All experiments presented in this work were performed in a geometrical configuration, where the angle between the magnetic field and the polarization of the laser field is 90°. The Bloch equations predict an excitation spectrum with 4 dark resonances for this case, as shown in Fig. 3.4.

Measuring excitation spectra is of fundamental importance for calibrating the experiment, since the shape of the spectra sensitively depends [52] on the laser intensities (Rabi frequencies), laser detunings and linewidths, the magnetic field and the angle between the magnetic field and the electric polarization.

3.4 Correlation functions

3.4.1 Introduction

The statistical properties of a light field are characterized with a set of correlation functions of different moments. In general, the degree of r-th order coherence is defined as [23, 51]

$$g^{(r)}(\mathbf{r}_1 t_1, ..., \mathbf{r}_r t_r; \mathbf{r}_{r+1} t_{r+1}, ..., \mathbf{r}_{2r} t_{2r}) = \tag{3.29}$$

$$\frac{\langle : E^*(\mathbf{r}_1 t_1)...E^*(\mathbf{r}_r t_r)E(\mathbf{r}_{r+1} t_{r+1})E(\mathbf{r}_{2r} t_{2r}) : \rangle}{[\langle |E(\mathbf{r}_1 t_1)|^2 \rangle ... \langle |E(\mathbf{r}_r t_r)|^2 \rangle \langle |E(\mathbf{r}_{r+1} t_{r+1})|^2 \rangle ... \langle |E(\mathbf{r}_{2r} t_{2r})|^2 \rangle]^{1/2}} \ , \tag{3.30}$$

where E is the electric field and (r_i, t_i) denotes a space-time point, "::" denotes time and normal ordering. Experimentally, the first- and second order coherence are of greatest importance. The lowest order of coherence is [51]

$$g^{(1)}(\mathbf{r}_1 t_1, \mathbf{r}_2 t_2) = \frac{\langle : E^*(\mathbf{r}_1 t_1)E(\mathbf{r}_2 t_2) : \rangle}{[\langle |E(\mathbf{r}_1 t_1)|^2 \rangle \langle |E(\mathbf{r}_2 t_2)|^2 \rangle]^{1/2}} \ . \tag{3.31}$$

The $g^{(1)}$-function describes the ability of light fields to interfere, i.e. $g^{(1)}(\mathbf{r}_1 t_1, \mathbf{r}_2 t_2) = 1(0)$ describes a first-order coherent (incoherent) light-field. A measurement of the fields at the same point in space ($\mathbf{r}_1 = \mathbf{r}_2$) but at different points in time ($t_1 = t, \ \ t_2 = t + \tau$) reduces Eq.(3.31) to

$$g^{(1)}(t, t+\tau) \equiv g^{(1)}(\tau) = \frac{\langle : E^*(t)E(t+\tau) : \rangle}{\langle E^*(t)E(t) \rangle} \ . \tag{3.32}$$

Thus a function measuring the interference contrast as a function of the time-difference τ is obtained. The $g^{(1)}(\tau)$-function is moreover of fundamental interest for determining the spectrum of a light field, since its Fourier-transform is the spectral distribution

$$S(\omega) = \frac{1}{2\pi} \int_{-\infty}^{\infty} g^{(1)}(\tau) e^{i\omega\tau} d\tau \ . \tag{3.33}$$

In the same way we determine

$$g^{(2)}(t, t+\tau) \equiv g^{(2)}(\tau) = \frac{\langle : E^*(t)E^*(t+\tau)E(t+\tau)E(t) : \rangle}{\langle E^*(t)E(t) \rangle^2} \ . \tag{3.34}$$

This correlation function measures the second-order coherence of a light field, also called intensity correlation function, since $I(t) \propto E^*(t) \cdot E(t)$, where $I(t)$ is the intensity operator of a light field. The intensity can be measured with analog devices, such as photodiodes, or with photon counting elements, such as photomultipliers (PMT), for weak fields. For an experimental interpretation we write the correlation function in terms of count rates N. Equation (3.34) can be rewritten

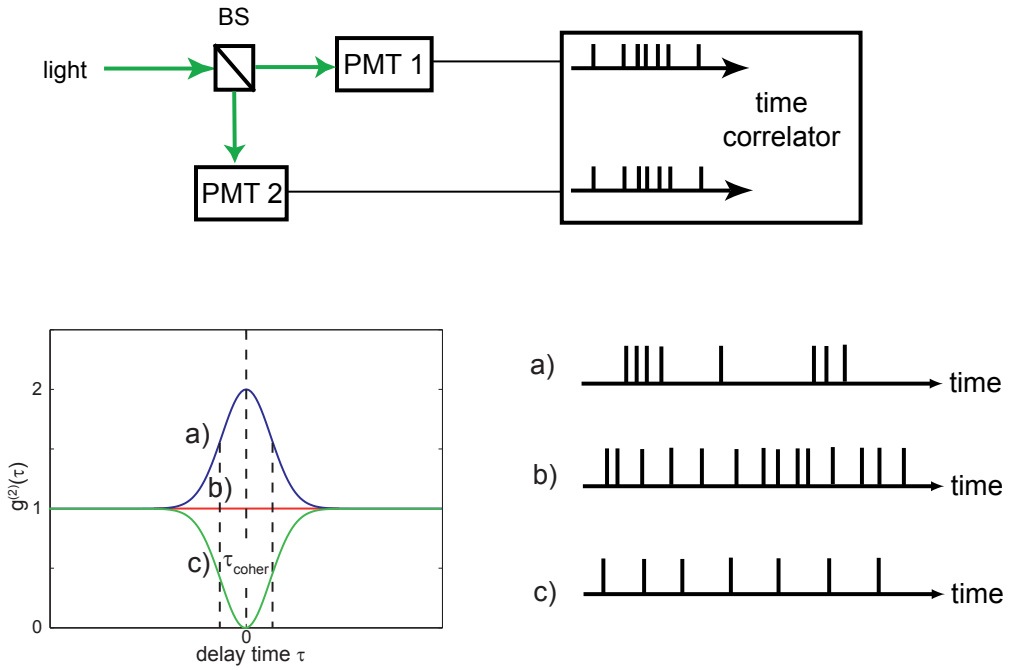

Figure 3.5: Illustration of a Hanbury-Brown and Twiss measurement setup (top), schematic correlation functions (left) and photon stream pictures of different light fields. The cases a), b) and c) correspond to thermal light, coherent laser light and non-classical light emitted by an ion.

$$g^{(2)}(\tau) = \frac{\langle : I(t)I(t+\tau) : \rangle}{\langle I(t) \rangle^2} = \frac{\langle : N(t)N(t+\tau) : \rangle}{\langle N(t) \rangle^2} \,. \tag{3.35}$$

This equation describes the temporal fluctuations of the light field. Here, it is implicitly assumed that first order interference can be neglected. However, ch. 7 and 9 show experiments, where is assumption is not fulfilled.

Experimentally, a second order correlation function is obtained by measuring the intensity at time t and at a later time $t+\tau$ normalized to an average intensity squared. This measurement is realized in a Hanbury-Brown and Twiss setup depicted in Fig. 3.5, where the light is directed to two PMT's via a beam splitter. Correlations are obtained by comparing the arrival time of two photons statistically. A normalization is applied, such that $g^{(2)}(\infty) = 1$. For classical light fields one finds the Cauchy-Schwarz inequalities

$$\begin{aligned} g^{(2)}(0) &\geq 1 \qquad \text{and} \\ g^{(2)}(\tau) &\leq g^{(2)}(0). \end{aligned} \tag{3.36}$$

The inset in Fig. 3.5 shows the second order correlation function for different light fields. For thermal light (case a)) the second order correlation for $\tau = 0$ is two and gets smaller for larger τ, depending on the coherence time τ_{coher} of the light source. After the detection of one photon there is a higher probability of detecting another photon with a small time delay τ than with a larger one. This behavior is called **bunching**. Photons preferably arrive in packets of two or more photons as illustrated in the photon stream picture. It reflects the bosonic nature of light and strong intensity fluctuations. For laser light (case b)), the correlation function $g^{(2)}(\tau) = 1$ for all τ, no intensity fluctuations are observed. This indicates a long coherence time. A photon stream of such a source has a constant flux, and photons do not show any correlation. Case c) is indicating a non-classical correlation function with $g^{(2)}(0) < 1$, where photons never appear in packets of two. This so-called **Anibunching** is observed for instance observed in a stream of photons emitted by an ion.

3.4.2 Second order correlation function for a single ion: Antibunching

A measurement of the second order correlation function is based on the detection of two photons. The observation of the first photon emitted by the ion projects the ion to the ground state. As a consequence, the ion is not "able" to emit a second photon after the first one, it needs to be re-excited by the driving laser-field. As a consequence, fluorescence photons never appear in packets of two, they always arrive as single photons. This effect is called **Antibunching** and is a signature for non-classical light. The second order correlation function in this case is $g^{(2)}(0) = 0$, since the probability of emitting a second photon right after the first one is 0. This violates the inequality (3.36) for classical light fields and proves the non-classical emission statistics.

Formally, the correlation function can be evaluated by inserting electric field operators. For simplicity, a two-level system with excited state $|g\rangle$ and $|e\rangle$ is assumed in the following. Resonance fluorescence photons emitted by the ion are associated with an atomic decay described by the operator $\sigma^-(t) = |g\rangle\langle e|$ to create an electric field at time t of the form

$$\widehat{E}(t) = \xi e^{-i\omega_L t}\sigma^-(t)\Theta(t). \tag{3.37}$$

Here, ξ is a constant amplitude, ω_L the laser frequency and $\Theta(t)$ a step function at t=0, i.e. $\Theta(t < 0) = 0$ and $\Theta(t \geq 0) = 1$. It is assumed that photons are just elastically scattered. The correlation function of first and second order take the form of

$$g^{(1)}(\tau) = \frac{\langle : \widehat{E}^{\dagger}(t)\widehat{E}(t+\tau) : \rangle}{\langle \widehat{E}^{\dagger}(t)\widehat{E}(t) \rangle} \tag{3.38}$$

$$g^{(2)}(\tau) = \frac{\langle : \widehat{E}^{\dagger}(t)\widehat{E}^{\dagger}(t+\tau)\widehat{E}(t+\tau)\widehat{E}(t) : \rangle}{\langle \widehat{E}^{\dagger}(t)\widehat{E}(t) \rangle^2} , \tag{3.39}$$

or in terms of the atomic operators

$$g^{(1)}(\tau) = \frac{\langle : \sigma^{+}(t)\sigma^{-}(t+\tau) : \rangle}{\langle \sigma^{+}(t)\sigma^{-}(t) \rangle} \tag{3.40}$$

$$g^{(2)}(\tau) = \frac{\langle : \sigma^{+}(t)\sigma^{+}(t+\tau)\sigma^{-}(t+\tau)\sigma^{-}(t) : \rangle}{\langle \sigma^{+}(t)\sigma^{-}(t) \rangle^2} . \tag{3.41}$$

The emission properties of a continuously laser driven ion are governed by the laser parameters. The Bloch equations serve as a complete set of equations for a quantitative description. It can be shown applying the quantum regression theorem [23, 52], that the correlation function of fluorescence photons at steady state limit reduces to

$$g^{(2)}(\tau) = \frac{\rho_{22}(\tau)}{\rho_{22}(\infty)} . \tag{3.42}$$

The diagonal matrix element $\rho_{22}(\tau)$ has to be evaluated with the initial conditions $\rho_{22}(0) = 0,\ \rho_{11}(0) = 1$ and $\rho_{12}(0) = \rho_{21}(0) = 0$.

In the following experiments 8 internal states (see Fig. 3.2 b)) are considered for the Barium-ion electronic structure. The procedure described above also applies for this case, such that the correlation function for the 493 nm fluorescence on the $|S_{1/2}\rangle$ to $|P_{1/2}\rangle$ transition is obtained by

$$g^{(2)}(\tau) = \frac{\rho_{33}(\tau) + \rho_{44}(\tau)}{\rho_{33}(\infty) + \rho_{44}(\infty)} = \frac{|b_{\mathrm{P}_{1/2}}(\tau)|^2}{|b_{\mathrm{P}_{1/2}}(\infty)|^2} , \tag{3.43}$$

where the $b_{\mathrm{P}_{1/2}}$ denotes the occupation amplitude of the $\mathrm{P}_{1/2}$ level [34]. Figure 3.6 shows a correlation function for a single Ba^{+} ion. One clearly observes the antibunching property, i.e. $g^{(2)}(0) = 0$. The increase of the probability for measuring a second photon is mainly governed by the intensities of the driving laser fields.

3.5 Resonance Fluorescence: Spectrum

The measurement of resonance fluorescence is one of the most important analysis tools in quantum optics. It allows one to study the interaction between light and matter described by the Bloch equations for both internal and external degrees of freedom.

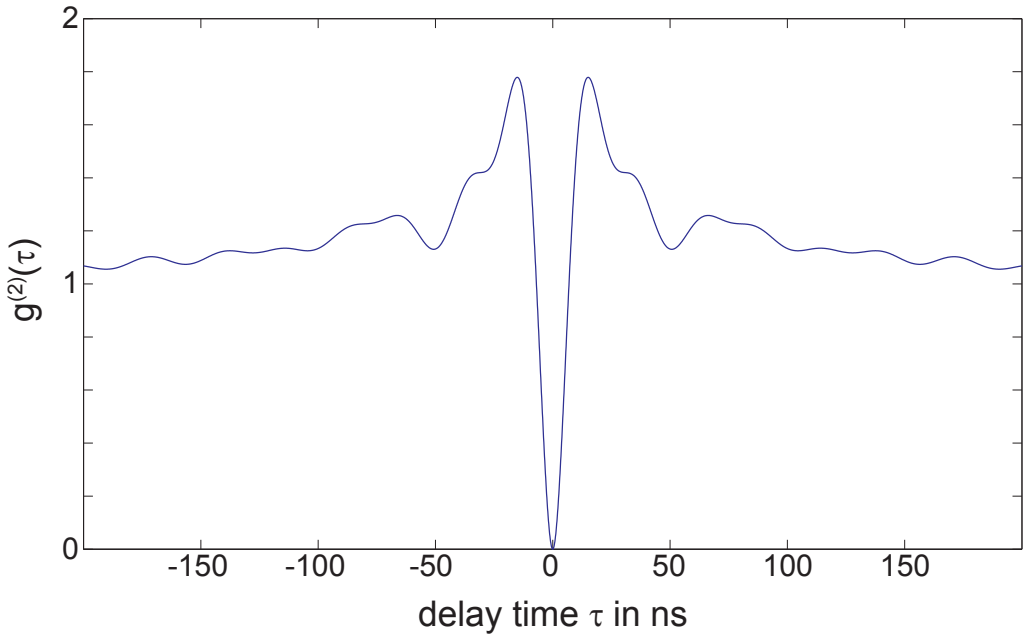

Figure 3.6: Second order correlation function for a single Ba^+ ion calculated from the eight-level Bloch equations. Note the non-classical property of anti-bunching. The parameters are: $S_g = 1.15, S_r = 2.2, \Delta_g = -25\,\mathrm{MHz}, \Delta_\mathrm{r} = -5\,\mathrm{MHz}, \delta_\mathrm{l}\mathrm{g} = \delta_\mathrm{l}\mathrm{r} = 40\,\mathrm{kHz}, \mathrm{u} = 2.3, \alpha = 95°$.

Right from the beginning of ion trap experiments the investigation of resonance fluorescence was one of the most important goals. Single ions are ideal systems for such investigations, in particular Ba^+ ions played a crucial role [53].

There are several ways to observe resonance fluorescence. One was already introduced to the reader as excitation spectroscopy, where the fluorescence of an ion is measured as a function of the detuning of one laser field. Another approach is to measure the spectral properties of resonance fluorescence with the help of a spectrum analyzer in different types of heterodyne or homodyne setups.

3.5.1 Spectrum of an atom at rest

The spectrum of resonance fluorescence for a single two-level atom driven by a laser-field was first predicted by Mollow in 1969 [54] and then measured by Schuda, Stroud and Herscher in 1974, in the group of Ezekiel in 1975 with sodium atoms and by H. Walther [57].

In a low excitation regime, the spectrum only shows an elastic peak centered at the frequency ω_L of the incident laser which has the same spectral distribution as the

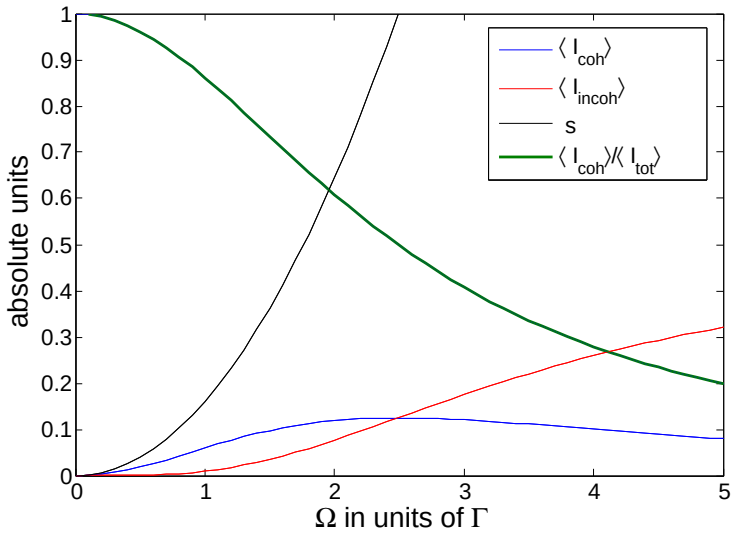

Figure 3.7: Fraction of the elastic (coherent) scattered light as a function of the laser-power (Rabi-frequency in units of Γ). Black: Saturation parameter defined in [55].

laser. For high excitation intensities three inelastic contributions centered at ω_L and at $\omega_L \pm \Omega_R$ show up and form the so-called "Mollow-Triplet", where Ω_R is the Rabi frequency. The appearance of the "sidebands" at $\omega_L \pm \Omega_R$ are a consequence of the coupling of the atom and the quantized light field states (dressed states) due to dipole interaction (a.c. Stark shift). The height of the peaks centered at $\omega_L \pm \Omega_R$ are 1/3 of the height of the inelastic central peak.

The fraction of elastic and inelastic radiation in a two-level system is for instance calculated in [55]. There, the saturation parameter

$$s = \frac{\Omega^2/2}{\Delta^2 + (\Gamma^2/4)} \tag{3.44}$$

is defined. Ω, Δ, are the Rabi-frequency and the detuning, Γ is the transition linewidth. The contributions of elastic (coherent) and inelastic (incoherent) scattering then read

$$\begin{aligned} \langle I_{coh} \rangle &= \frac{1}{2} \frac{s}{(1+s)^2} \\ \langle I_{incoh} \rangle &= \frac{1}{2} \frac{s^2}{(1+s)^2} \\ \langle I_{tot} \rangle &= \langle I_{coh} \rangle + \langle I_{incoh} \rangle. \end{aligned} \tag{3.45}$$

Figure 3.7 shows the variation of each component as a function of the laser-intesity, i.e. the Rabi-frequency in units of the linewidth Γ (c.f. Eq. 3.10). The red (blue)

curve shows $\langle I_{coh}\rangle$ ($\langle I_{incoh}\rangle$), the thick, green curve shows the fraction of $\langle I_{coh}\rangle$ in the emitted radiation. As stated above, for low laser-powers almost all scattering is elastic. Experiments performed in this work use laser-powers with $\Omega/\Gamma \approx 1$ such that more than 80 % of the scattering is elastic. For clarity, the black curves shows the saturation parameter defined in Eq. (3.44). Note, that the saturation parameter as defined above is valid for three-level systems, for an eight-level system, the respective Clebsch-Gordan coefficients have to be included in the Rabi-frequency

A detailed investigation of the resonance fluorescence spectrum of a single Ba^+ ion under strong excitation at 493 nm and and a weak red (650 nm) excitation can be found in [58].

3.5.2 Spectrum including motional sidebands

We consider a two-level atom with excited state $|e\rangle$ and ground state $|g\rangle$ coupled to a laser field with frequency ω_L. The ion in the trapping potential oscillates at secular frequencies denoted by $\omega_x,\ \omega_y,\ \omega_z$ and at the micro-motion Ω_{rf}. In the following, the ion-motion is assumed to be merely one dimensional along x with frequency ω_x. The motion of the ion is quantized and associated with a quantum number n denoting the motional state $|n\rangle$. The composite electronic-motional states are denoted by $|n,{}^{e}_{g}\rangle$.

When the ion is irradiated, there is a possibility of changing its motional state during the emission of a photon. This corresponds to a situation drawn in Fig. 3.8. A change in the motional quantum can happen via two different quantum paths: First, the atom is excited on the $|n,g\rangle$ to $|n,e\rangle$ transition and spontaneously decays into the states $|n\pm 1,g\rangle$ associated with photons altered in frequency by one quantum of motion. The second option is a transition from $|n,g\rangle$ into $|n\pm 1,e\rangle$ state followed by a spontaneous emission without changing the quantum number. In the spectrum, three different Lorentzian contributions appear centered at ω_L and at $\omega_L \pm \omega_x$. Transitions with $\Delta n = 0$ at the center ω_L are called "carrier transition", whereas the transition centered at $\omega_L + \omega_x$ ($\omega_L - \omega_x$) is called the blue (red) sideband transition.

For a regime where the extension of the ion's ground state wave-packet a_0 is much smaller than the wavelength λ of the laser field, i.e. the Lamb-Dicke regime with $\eta = 2\pi a_0/\lambda \ll 1$, calculations show ([36, 59, 60]), that the coupling strength of the different sidebands relative to the carrier coupling given in Rabi frequency Ω_0 is given by

$$\begin{aligned} \Omega_{n,n-1} &= \Omega_0\sqrt{n}\,\eta \\ \Omega_{n,n+1} &= \Omega_0\sqrt{n+1}\,\eta. \end{aligned} \tag{3.46}$$

Thus, the height of the (first) motional sideband is a factor of $\eta \ll 1$ smaller than the carrier. The relative heights of the blue and the red sidebands reflect the population difference of the trap levels $|n\rangle$ and can be used to determine the ion's energy measured

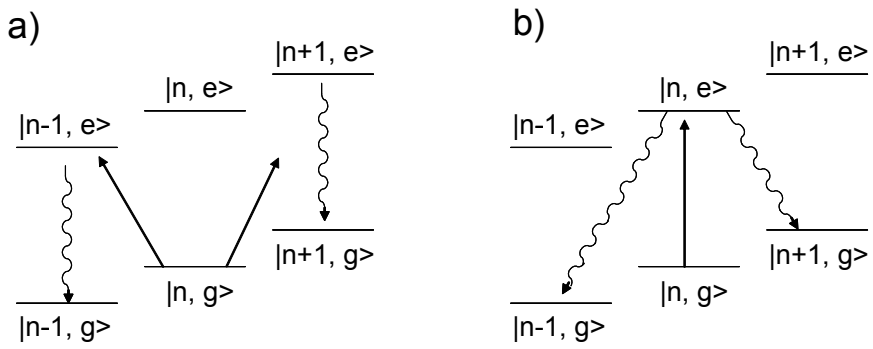

Figure 3.8: Level scheme of a two level atom in a harmonic potential coupled to a laser field. $|n, g\rangle$ describes the atom in state with n quanta of motion and in the electronic ground state. Arrows denote laser stimulated transitions, wavy lines show spontaneous emission processes [59].

as motional excitation $\langle n \rangle$. For an ion approaching the ground state of the trapping potential, the red sideband's amplitude vanishes [61]. Moreover, the width Γ of the sideband is given by half the laser cooling rate (for a two-level system) and is of interest for the measurements shown in the next chapter.

In reality, the ion oscillates in 3 dimensions and the overall spectrum consists of the carrier, the 3 red and the 3 blue sidebands. Additionally, the ion exhibits a micromotion part at the driving frequency of the trap, which gives another contribution to the resonance fluorescence spectrum. Figure 3.9 shows a schematically a spectrum of resonance fluorescence .

So far all the transitions are assumed to be narrow, i.e. the lifetime of the decaying state is sufficiently long. This assumption holds for instance for the quadrupole transition $|S_{1/2}\rangle$ to $|D_{5/2}\rangle$ in $^{40}Ca^{+}$ with an associated linewidth of 1 Hz, but not for dipole transitions with linewidths of several tens of MHz, which is the case for the $|S_{1/2}\rangle$ to $|P_{1/2}\rangle$ transition in $^{138}Ba^{+}$ at 493 nm wavelength. The width of the carrier conceales the motional sidebands and investigations of the spectral distribution of the fluorescence are tricky. Nevertheless, throughout the history of the experiment presented here, some clever ideas have made this investigations possible. In the following, one of this methods is presented.

3.5.3 Measurement of the spectrum in a "Self-homodyne" setup

A measurement of the spectrum of resonance fluorescence requires a tuneable and narrowband filter in front of the detector. In some experiments (e.g. in [58]) Fabry-Perot interferometers were used to scan the collected fluorescence light but with a

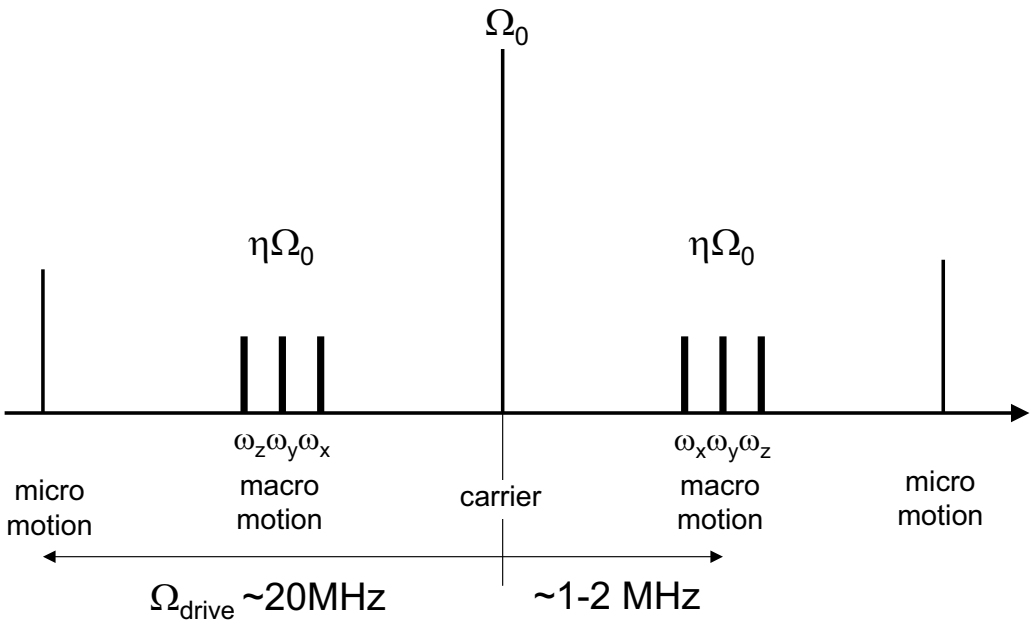

Figure 3.9: Schematic spectrum of the resonance fluorescence of a trapped ion. Sidebands appear at the motional frequencies of the ion (macro motion) and at the frequency of the trap drive (micro motion). Ω_0 and η describe the coupling of a laser field to the carrier and to the sidebands.

limited spectral resolution on the order of MHz. Fabry-Perot interferometers appear to be a proper tool for measuring coarse features in the spectrum, such as the Mollow triplet.

A method with a much higher resolution was realized in 2000 by making use of a heterodyne setup [62]. The principle relies on a beat-signal between the resonance fluorescence and a local oscillator ω_{lo} detuned by several tens of MHz with respect to the driving laser field for the ion (ω_{fluo}). The carrier transition and the entire spectrum is thus shifted to an easy to access frequency range at $\omega_{fluo} - \omega_{lo}$. The measurements could even show the elastic carrier peak of the Rayleigh scattering and was only limited by the resolution bandwidth of the spectrum analyzer.

A quite similar method is discussed in the following. By setting the difference frequency of the local oscillator to zero one would obtain a spectrum of the resonance fluorescence with a carrier at zero frequency. In the literature, this is referred to as **homodyning**. While the experimental setup can be smaller than in a heterodyne configuration, one still needs an interferometric setup similar to the one presented in [62].

Throughout this work the spectrum of the resonance fluorescence is measured with the help of a **"self-homodyne" setup** making use of a high resolution single photon interference. Figure 3.10 depicts such a quite simple but effective setup consisting of a

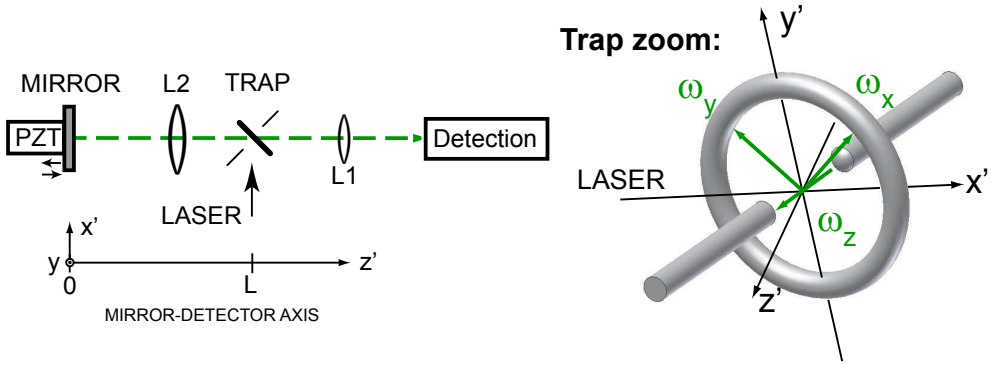

Figure 3.10: The self-homodyne setup. The fluorescence of the ion is back-reflected by a distant mirror thus creating interference. (x', y', z') is the laboratory coordinate system, (x, y, z) the trap system.

single ion and one mirror.

The ion localized at the trap center ($z = L$) is illuminated by a laser-field and emits fluorescence into 4π solid angle. Two opposite channels allow for detection, one through the lens L2, which directs a collimated beam to a distant mirror ($z = 0$) mounted on a piezo transducer. Through lens L1 the ion and its mirror image can be observed. For a perfect alignment interference of the partial waves of single resonance fluorescence photons is observed. The piezo translation stage allows for scanning the interference pattern and thus modulates the measured intensity. Along the mirror-detector axis the electric field created by the ion reads

$$E_z(t) = \sqrt{\epsilon\Gamma_g}\sin(k_g(L + \widehat{z}_m))\sigma^-(t) \ , \tag{3.47}$$

where ϵ is the fraction of solid angle collected, Γ_g is the $P_{1/2}$-$S_{1/2}$ spontaneous emission rate and k_g the corresponding photon momentum. L is the distance between the ion and the mirror and $\sigma^-{=}|S_{1/2}\rangle\langle P_{1/2}|$ is the Pauli lowering operator with a time evolution $\sigma^-(t){=}\sigma^- e^{-i\omega_L t}$ and ω_L the excitation laser frequency. The operator $\widehat{z}_m$ is the position operator of the ion relative to the center of the trap. More precisely, since the trap axis is tilted by an angle θ with respect to z', z_m corresponds to the projection of x, y and z along z (x, y and z denote the coordinates of the ion in the trapping potential basis). The ion position operator is $\widehat{z}_m(t){=}A_{\omega_t}(a_m e^{-i\omega_t t}{+}a_m^\dagger e^{i\omega_t t})$. a_m and $a_m^\dagger$ are the bosonic operators associated with the motion of the ion in the trap, at the frequency[3] ω_t, and A_{ω_t} is a normalization factor.

The measured intensity is calculated via the first order correlation function

$$\langle I(t)\rangle_c = \langle E_z^\dagger E_z\rangle_c(t) = Tr\langle E_z^\dagger E_z \rho_c(t)\rangle. \tag{3.48}$$

[3] ω_t is used as a general notation for one of the oscillation frequencies $\omega_{x,y,z}$

The index "c" is referring to *conditional* dynamics [75, 76] counting for a measurement induced projection of the system into the ground-state. Inserting (3.47) into (3.48) one obtains

$$\langle I(t)\rangle_c = \epsilon\Gamma_g\langle\sin^2(k_g(L+\widehat{z}_m))\rangle_c(t)\langle\sigma^+\sigma^-\rangle_c(t) \tag{3.49}$$

On one hand the measured intensity is modulated by the distance between the mirror and the ion (L), and on the other hand it is modulated by the motion of the ion in the trap denoted by $\widehat{z}_m$. It can be shown [76] that neglecting the motion of the ion and assuming a constant ion-mirror distance L leads to an intensity

$$\langle I(L)\rangle_c = \gamma\ \sin^2(k_gL), \quad \text{where} \tag{3.50}$$

$$\gamma = \epsilon\Gamma_g\frac{\Omega_g^2}{4\Delta_g^2+\Gamma_g^2} \tag{3.51}$$

is the optical pumping rate into the mirror channel, Ω_g denotes the Rabi frequency and Δ_g the laser detuning. The average photocurrent thus exhibits a modulation induced by the variation of the ion-mirror distance. According to Fig. 3.11 the bottom of the intensity fringes corresponds to the ion being at a node of the mirror field, i.e. k_gL= nπ (n being an integer), the maximum of the fringes correspond to the situation where k_gL= (n+1/2)π (antinode of E_z).

Including the ion motion the photocurrent reads

$$\langle I(t)\rangle_c = \gamma\ \langle\sin^2(k_g(L+\widehat{z}_m))\rangle_c(t). \tag{3.52}$$

In the Lamb-Dicke regime $\eta = 2\pi z_0/\lambda \sim 0.07 \ll 1$ (z_0 denotes the r.m.s. size of the trap ground state) the motional sidebands have intensities reduced by the Lamb-Dicke parameter η relative to the elastic component of the fluorescence. One can then expand exponentials, e.g. $e^{ik_g\widehat{z}_m} = e^{i\eta(\widehat{a}_m+\widehat{a}_m^\dagger)} \equiv 1 + i\eta(a_m + a_m^\dagger)$. The average position of the ion can be fixed by setting k_gL= (n+1/4)π, i.e. on the maximum slope of the interference fringes. In this particular case

$$\langle I(t)\rangle_c = \frac{\gamma}{2}\langle 1 + 2\eta(a_m + a_m^\dagger)(t)\rangle_c + o(\eta^2) \tag{3.53}$$

In a frame rotating with the laser frequency, the green fluorescence then consists of a strong elastic component at zero-frequency (the constant contribution in Eq. (3.53) and a second contribution a factor of η weaker than the carrier and proportional to the position operator of the ion, $\widetilde{z}_m \equiv a_m + a_m^\dagger$. The second term thus contains the information of the ion motion and the motional sidebands in the frequency domain.

This situation is indeed reminiscent of homodyne detection, where a strong local oscillator (the elastic scattering) beats with a weak signal close in frequency (the motional side-bands) allowing for a detection of motional sidebands, though the carrier transition due to the linewidth of 15 MHz would conceal the motional sidebands.

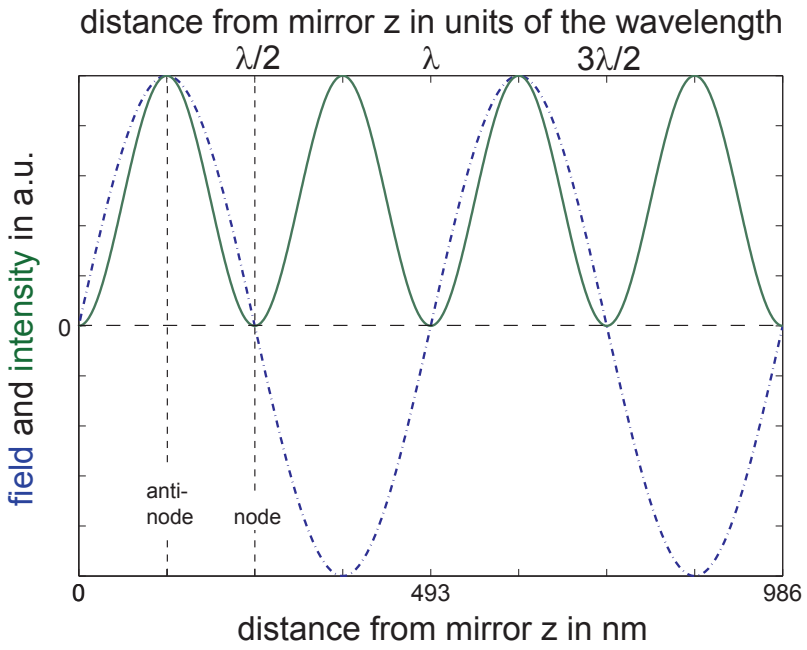

Figure 3.11: Standing wave (dashed dotted) and intensity in a "half cavity" as a function of the distance from the mirror. The field is $\propto \sin(k_g L)$, the intensity $\propto \sin^2(k_g L)$. Node of the standing wave/ minimum fringe: $k_g L = n\pi$; antinode of the standing wave/ maximum fringe $k_g L = (n + \frac{1}{2})\pi$.

4 General Experimental Setup

All measurements reported in this thesis were done with the so-called old trap, a ring trap. While this system is still in operation, an additional linear trap was set up to increase the variety of applications of the experiment. As a first point, this chapter gives a summary of the old setup used for the experiments including the ring trap, the cooling lasers and the detection setup. Special constructions for the individual measurements are discussed in the according chapters. As a second point, this chapter contains all important operational and geometrical parameters for the new trap and the new setup.

4.1 The old setup: A summary

In this part the old setup is discussed, i.e. the ion trap, the two laser systems at 493 (green) and 650 nm (red) and the detection setup.

A very detailed description of the setup can be found in [31], here a summary should suffice. The vacuum chamber plotted in 4.1 (reproduced from [44]) of the old setup has a spherical shape with two opposite CF-150 viewports for observation and 6 CF-36 viewports with 3 independent directions for laser-cooling. Two Barium ovens point towards the center of the trap as well as an e-gun system which is equipped with electron optics. The Paul trap and the compensation electrodes are mounted on the top flange and are thus hanging upside down. For a better orientation we define the main laser cooling direction as x' and the observation direction as z'. Note, that the trap coordinate system is denoted with x, y and z according to the oscillations ω_x, ω_y and ω_z.

The miniaturized Paul trap consists of a ring electrode with $2r_0$=1.4 mm inner diameter made out of a 0.2 mm molybdenum wire and two endcap electrodes with the same wire diameter and a distance of $2z_0$=1.4 mm (see Fig. 4.1). The latter are usually at ground potential (but can be used for additional external fields), whereas the ring electrode is connected to a radio frequency drive at $\Omega_{\mathrm{rf}}/2\pi \sim 20$ MHz and an amplitude of $\mathrm{U}_{RF} \sim 500\, V_{pp}$. The dynamical electric field creates a pseudopotential of a well depth of approximately 50 eV in which the ion can be held over weeks. The quasi-free secular (or macro) motion of the ion is decomposed into three normal modes along the trap coordinate axis x, y and z. The first two are radial modes and have measured values on the order of $\omega_x/2\pi \sim 1$ MHz and $\omega_y/2\pi \sim 1.2$ MHz, the motion along z is the axial mode and has a measured frequency of $\omega_z/2\pi \sim 2$ MHz. In the following

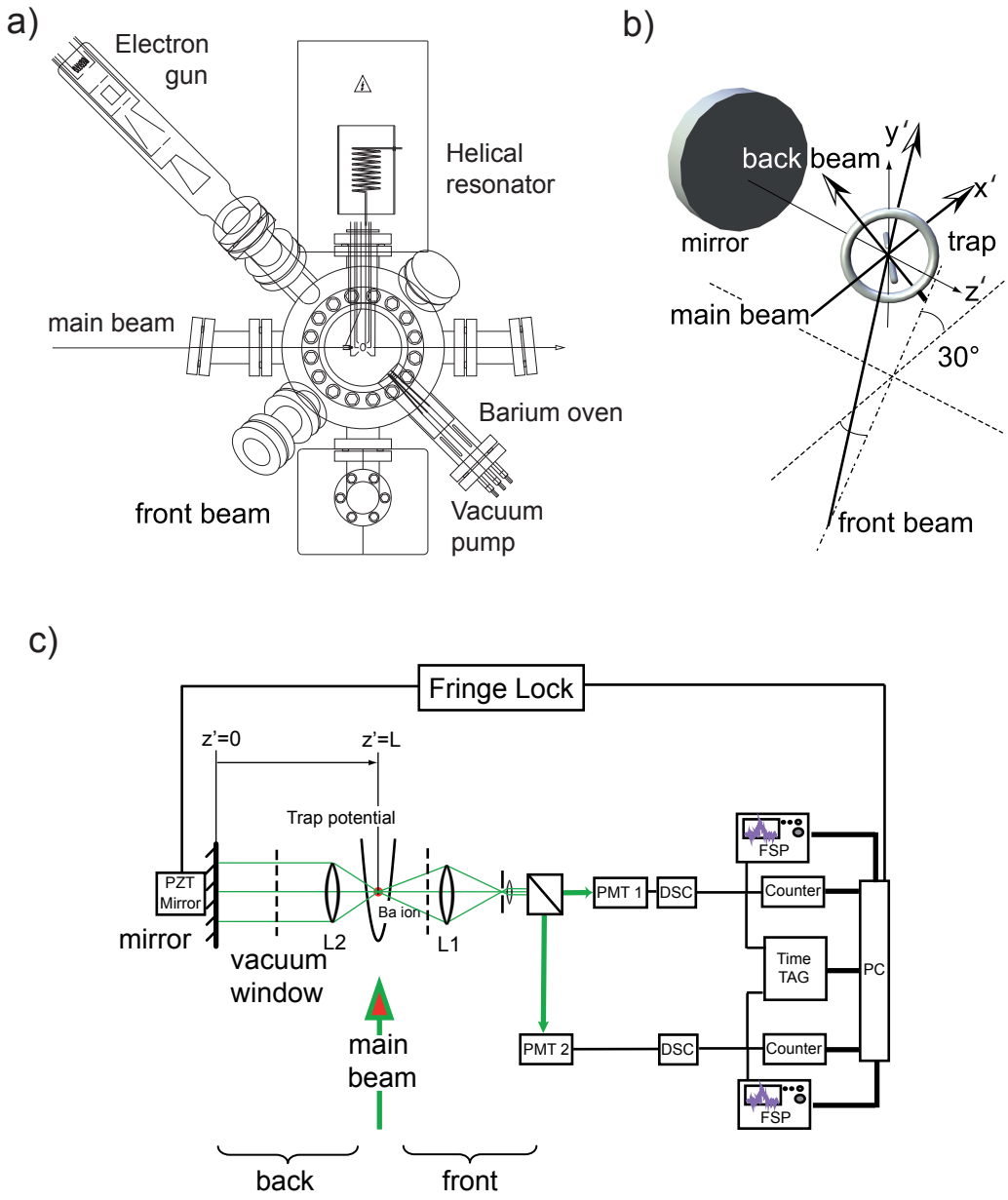

Figure 4.1: Sketches of the old setup: *a)* Vacuum vessel (reproduced from [44]). *b)* The Paul trap and the orientation of the three cooling laser directions. *c)* Observation and analysis: PZT...piezo, L1...macroscope, L2...Halo-lens, DSC...discriminator, Time Tag...correlator, FSP...spectrum analyzer.

these modes will be referred to as the "X" (x), "Y" (y) and "Z" (z) sidebands. Additionally to the secular motion a micromotion part modulated at the drive-frequency of $\Omega_{\mathrm{rf}}/2\pi = 20\,\mathrm{MHz}$ is superimposed on the trajectory of the ion in the trap. Through all the measurements it is compensated for the micromotion so that it can be neglected.

The cooling laser fields are mode overlapping and sent through the trap along $\overrightarrow{k}$ parallel to the x' axis with the polarization vector $\overrightarrow{\varepsilon}$ perpendicular to $\overrightarrow{k}$ and parallel to the y' axis (see Fig. 4.1 b)). For optimal laser cooling three different directions can be used to illuminate the ion, called "main", "front"- and "back"-beam. A weak (about 2 G) homogenous magnetic field $\overrightarrow{B}$ along the z'-axis prevents optical pumping among the 5 $D_{3/2}$ sub-states and defines the quantization axis.

The fluorescence of the ion is observed along the z' axis (perpendicular to the propagation of the laser light fields and parallel to the $\overrightarrow{B}$ field) in two opposite directions, i.e. the back and the front channel as depicted in Fig. 4.1 c). For the experiments discussed in Chapter 5 to 7 the front channel is the only observation channel. The light is collected through a large viewport with a macroscope (Wild Modell M400, F♯=2, L1), focused onto a pinhole with 600 μm diameter and is sent to one of the photomultipliers (PMT 1 or PMT 2) after passing a spectral filter, a focussing lens and a 50/50 beam-splitter. In the mirror channel the light is collected with a high quality, custom-made lens (Linos Halo 25/04) inside the vacuum chamber (L2). It is mounted on a stainless steel tube fixed on a vacuum bellows. The lens is designed to collect light from a large solid angle (numerical aperture of 0.4, working distance 10 mm) and to minimize wavefront distortion. The quality of the wavefront was measured to be better than $\lambda/10$ peak-to-valley to perform interference measurements. One drawback of the old setup is the mounting of this lens. The orientation of the lens depends on three screws with 120° angular separation pressing against the vacuum chamber. Turning one of the screws changes the lens orientation in all three dimensions thus making the alignment complicated.

For analysis, two photomultipliers measure the photo-current and send the pulses to different measurement devices such as spectrum analyzers, counters and correlators.

4.2 The new linear trap

As described in Chapter 2 a linear trap configuration offers the possibility of storing more than one ion without obtaining excessive micromotion. A logical consequence of the measurements performed in [28], where interference effects of *one* ion with its mirror image were studied, is to increase the number of ions in the trap. Measurements described in [62] showed a reduced contrast of this interference effect by virtue of an excessive micro-motion. In a linear trap this effect can be excluded and further analysis is possible. Moreover, an integration of the new trap into the already existing setup opens the door to new measurements dealing with quantum networks and coupling of two traps.

4.2.1 Design parameters

For the sake of clarity, the most important parameters and relations derived in Chapter 2.3 are summarized. The parameters are the radial frequency $\omega_x = \omega_y = \omega_{rad}$, the stability parameter q and the axial frequency $\omega_z = \omega_{ax}$. Additionally, the Lamb-Dicke parameter η is listed, where the angle ϕ is between the laser propagation and the oscillation axis:

$$\omega_{rad} = \frac{q\Omega_{\mathrm{rf}}}{2\sqrt{2}} , \tag{4.1}$$

$$q = \frac{2|e|U_{\mathrm{rf}}}{mr_0^2\Omega_{\mathrm{rf}}^2} , \tag{4.2}$$

$$\omega_{ax} = \sqrt{\frac{2\kappa eU_{\mathrm{cap}}}{mz_0^2}} , \tag{4.3}$$

$$\eta = \cos\phi \; k\sqrt{\frac{\hbar}{2m\omega}} . \tag{4.4}$$

A comparison to the linear $^{40}Ca^+$ trap

The design of the linear trap used with $^{40}Ca^+$ trap is described in the thesis of S. Gulde [40] and has the following geometry: The half distance between the radial trap electrodes $r_0 = 0.8\,\mathrm{mm}$, the half distance between the tip electrodes is $z_0 = 2.5\,\mathrm{mm}$. The trap is operated at a drive-frequency of $\Omega_{\mathrm{rf}}/2\pi = 23.4\,\mathrm{MHz}$. Measurements of the radial frequency with a RF-power of 12 W yield $\omega_{rad}/2\pi = 4.35\,\mathrm{MHz}$ and thus a stability parameter of $q \approx 0.5$. As a consequence the amplitude of the RF field has to be $U_{\mathrm{rf}} \approx 1500\,\mathrm{V}$. Measurement in the axial direction yields $\omega_{ax}/2\pi = 1.7\,\mathrm{MHz}$ for a DC-Voltage of $U_{\mathrm{cap}} = 2000\,\mathrm{V}$, from which the field penetration factor $\kappa \approx 0.075$ can be estimated. A Lamb-Dicke factor of $\eta \sim 7\%$ is measured for the axial confinement.

If the same trap is loaded with $^{138}Ba^+$, the radial frequency scaling with $1/m$ will be reduced by the mass ratio $40/138 \sim 30\%$. The axial frequency is reduced by the square-root of the mass ratio $\sqrt{40/138} \sim 55\%$. The results obtained from the equations above are: $q_{\mathrm{Ba}} \approx 0.15$, $\omega_{rad,\mathrm{Ba}}/2\pi = 1.3\,\mathrm{MHz}$ and the axial frequency $\omega_{ax,\mathrm{Ba}}/2\pi = 0.92\,\mathrm{MHz}$. The effect of loading species with different mass is thus changing the trap frequency drastically. However, the extension of the ground-state wave-packet relative to the wavelength, i.e. the Lamb-Dicke parameter η, is just altered slightly in the axial direction such that $\eta \sim 8\%$. To obtain the same trapping frequencies in the radial direction the RF amplitude U_{rf} would have to be on the order of 5.2 kV and the cap voltage U_{cap} even higher at around 6 kV.

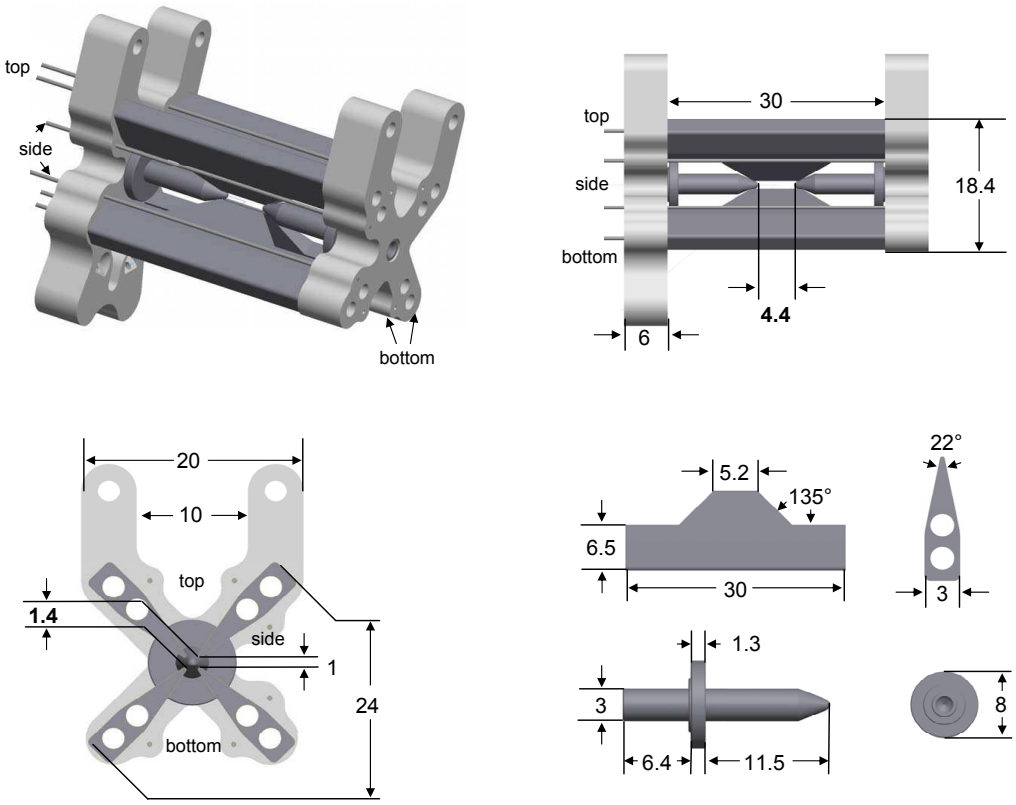

Figure 4.2: Geometry of the trap: Dimensions are given in mm, angles in degrees. "Top", "bottom" and "side" denote the pairs of compensation electrodes.

The final design

To avoid the use of such high voltages the trap geometry was changed slightly. To this end the most efficient way is to downsize the trap. As can be seen from the equations above, the radial oscillations scale with $1/r_0^2$ such that reducing the distance of the trap electrodes is very efficient. In addition, the optical access and machining limitations have to be considered. The axial frequency grows linearly with $1/z_0$, then half-distance between the tip electrodes, but even more important: For instance a reduction of z_0 by a factor of 2 allows for a reduction of the voltage U_{cap} by a factor of 4 (to obtain the same axial frequency.)

Considering the limitations for optical access and manufacturing the parameters were chosen to be

$$\begin{aligned} r_0 &= 0.7\ \mathrm{mm} \\ z_0 &= 2.2\ \mathrm{mm} \end{aligned}$$

With this geometrical parameters and a driving frequency of $\Omega_{\mathrm{rf}}/2\pi = 15.1\,\mathrm{MHz}$ the radial frequency is calculated to be $\omega_{rad}/2\pi = 2.45\,\mathrm{MHz}$ (corrected $\omega_{rad}/2\pi = 2.33\,\mathrm{MHz}$,

see Eq. 2.22) for an RF-amplitude of $U_{\mathrm{rf}} = 1500\,V$ and a corresponding $q = 0.45$. The axial frequency becomes $\omega_{ax}/2\pi = 1.05\,\mathrm{MHz}$ for a voltage of $U_{\mathrm{cap}} = 2000\,V$. Thus we obtain a Lamb-Dicke parameter of $\eta \sim 7.5\%$ in the axial direction.

Figure 4.2 is depicting the geometry of the trap in a detailed way: A 3D-image visualizes the setup, while different projections of individual ports show the dimensions given in millimeters. Light grey indicates macor® pieces[1] arranged by milling machines, while dark grey pieces are made up of stainless steel and are manufactured by a wire erosion machine.

The thin wires denoted with "top", "side" and "bottom" are electrodes used for compensating for all effects leading to a displacement of the ion from the dynamical minimum ("compensation electrodes"). Such effects can be stray fields or machining imperfections. To obtain a symmetric penetration of the compensation voltage applied to the electrodes without constraining the optical access, *pairs* of electrodes are attached to the same DC-potential.

A photograph of the trap is shown in the top panel of Figure 4.3. Note that the trap is mounted upside down in the final experimental setup. The white macor® pieces are used to fix the electrodes at different potentials. Most of the connections are done with copper-beryllium inline clamps.

4.2.2 Vacuum vessel, optical access and magnetic field

At the heart of the experiment is the trap, two Halo-lenses inside the vacuum, two Barium ovens, an electron emitter ("e-gun") and the respective electric feed-throughs. For alignment and installation purposes, all parts are mounted on a single CF-200 flange, while all other ports of the vacuum chamber are equipped with viewports. Figure 4.3 is presents a photograph of the experiment flange, Fig. 4.4 shows sketches of the entire vacuum vessel both in 3D and as 2-dimensional projections.

The experiment flange is attached to the main vacuum chamber which consists of an octagon and a six-way cross for vacuum-service ports. To reach and maintain a pressure on the order of $10^{-11}\,\mathrm{mbar}$ (UHV) the chamber was pumped out by a turbo-pump during baking of up to 150°C for one week. An ion pump and a Titan-sublimation (Ti-sub) pump are able to maintain the pressure after removing the turbo-pump system. Moreover, Barium itself is known as a "getter" such that Barium-emission from the oven supports the pumping systems. A vacuum gauge provides a measure of the pressure *inside* the chamber that is in the $10^{-11}\,\mathrm{mbar}$ range. Ions can be stored over 2-3 days in the linear trap without any laser cooling. The octagon, i.e. the main experiment chamber, offers 8 CF-63 ports and 2 CF-200 ports. The experiment flange is attached to the top CF-200-port, such that the experiment is hanging upside down. This allows us to mount the helical resonator [40] for the radio-frequency drive on top of the trap.

[1] This ceramic material is a very good thermal and electric insulator with very low outgassing rates making it perfect for UHV applications. Its operation temperature can be up to 1000°C.

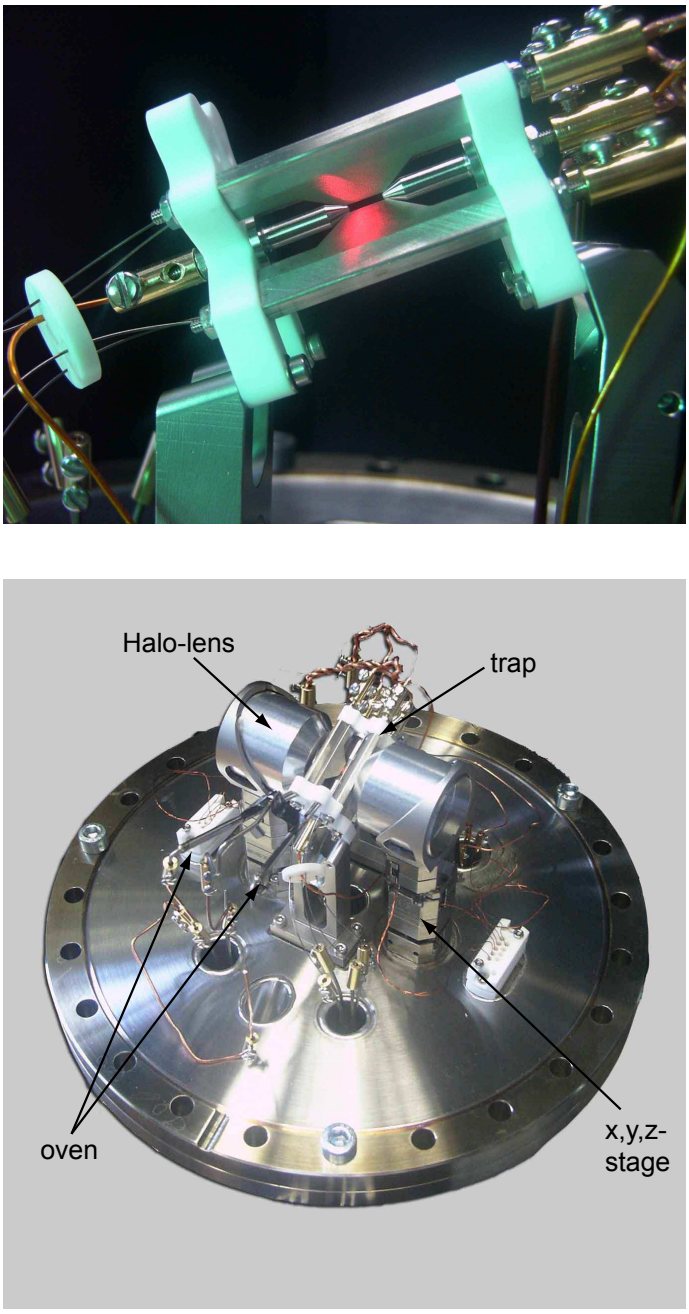

Figure 4.3: *Top:* Photograph of the new, linear trap illuminated with a laser-pointer. *Bottom:* Photograph of the experiment flange before integration into the vacuum chamber. The main components are the linear trap and the observation (Halo-) lenses mounted on x, y, z-translation stages. The steel tubes are the two Barium ovens.

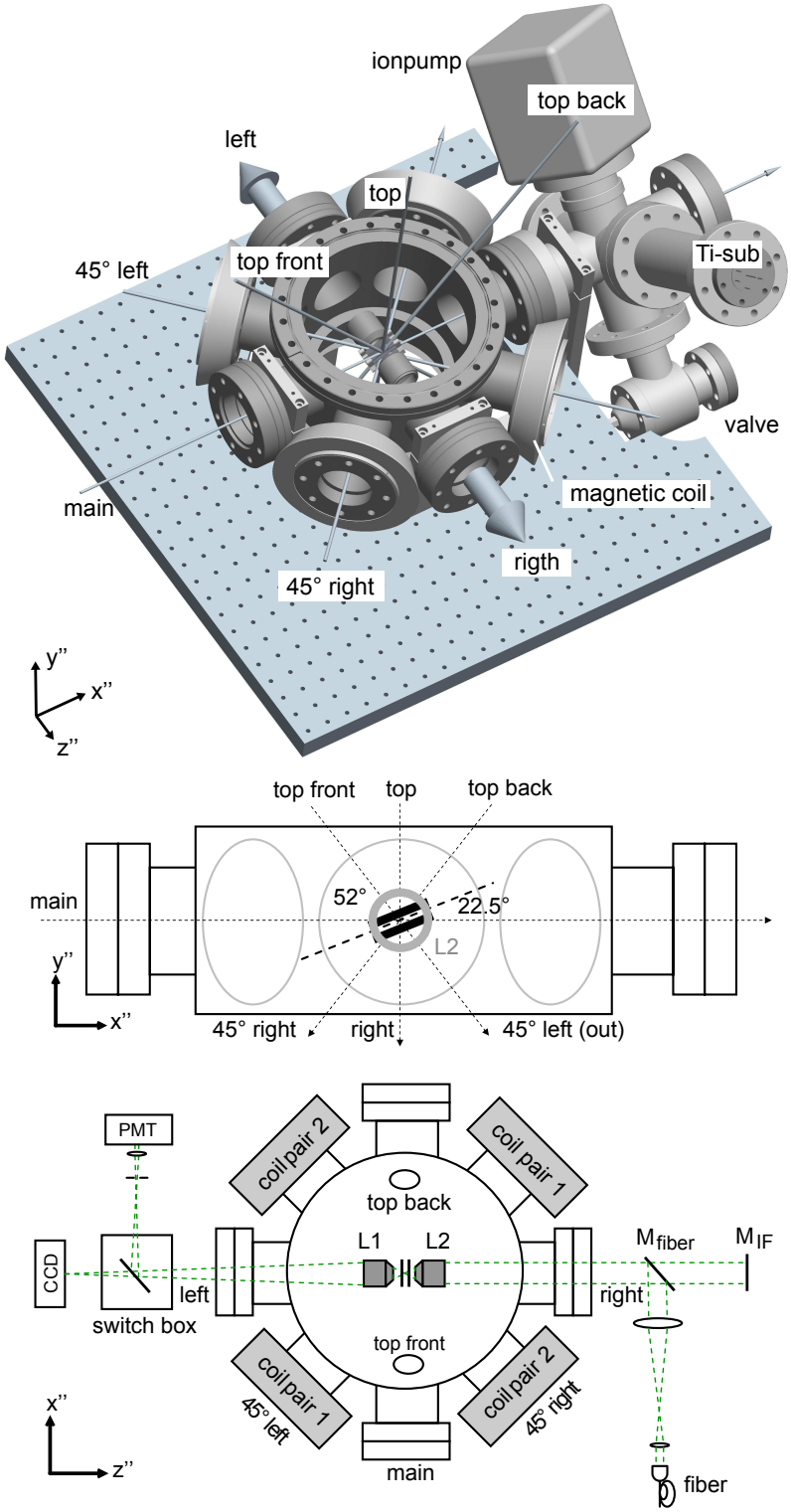

Figure 4.4: 3D sketch of the experimental setup: Thin arrows indicate cooling laser inputs, "left" and "right" are the observation channels. L1 and L2 Halo-lenses, M_{fiber} flip mirror to optical fiber, M_{IF} back-reflecting mirror for interference measurements. Details in the text.

For clarity, we define a lab coordinate system with the axis x'', y'', z'' and their respective unit vectors $\overrightarrow{e}_{x'',y'',z''}$. The relative statements of place right and left are valid for an observer looking along the x-axis: We denote x'' as the main laser-cooling direction such that the wavevector $\overrightarrow{k}$ is parallel to x''. The (linear) polarization of the incoming laser is oriented along the y direction and observation is done along the z''-directions defining the quantization axis. We furthermore define the horizontal plane as the (x'', z'')-plan parallel to the experiment flange and a vertical plane spanned by (x'', y'').

The linear trap is mounted at an angle of 22.5° out of the horizontal (x'', z'') plane, but with the trap axis in the vertical (x'', y'')-plane shown in the middle and the bottom panel of Fig. 4.4. The orientation is chosen to create projections of all oscillation directions of the ion in the trapping potential onto the cooling laser. While the linear trap operated with Calcium described in [40] is rotated in the horizontal plane, the here used rotation in the vertical plane allows for the observation of atoms/ions along the z-direction with lenses as close as 12 mm to the trap center, i.e. 2 mm away from the outside margin of the trap. Note, that the trap coordinate system, usually denoted with x, y, z (with z describing the trap axis), does not coincide with the lab system.

The orientation of the trap is crucial for a proper observation of resonance fluorescence. To take benefit from observation lenses *inside* the vacuum chamber in particular, the observation lenses have to fulfill several requirements: On the optical side the lens should collect as much fluorescence as possible and should be able to create a collimated beam. In particular for interference measurements another strong prerequisite are low wave-front abberations. The lenses should have an AR-coating for the important wavelengths. Material-wise the production of the lens and its housing has to consider UHV compatibility which also includes resistivity against baking of the system. Moreover, the lenses should be manufactured such that a beams going through the 45° viewports are not blocked by the lenses. Most of the requirements are already met using a custom made Halo-lens used in the old setup [44], where this configuration was tested to be suitable for high contrast interference measurements. Thus, the lens design was reproduced with some slight modifications. For clarity, the parameters of the lens are a focal length of $f = 25$ mm and a numerical aperture of 0.4, the lens collects a fraction of the solid angle of $\varepsilon \sim 4\%$. At a working distance of 11.8 mm at a wavelength of 493 nm the lens can be mounted as close as 1.8 mm to the trap. The mounts of the lenses in the new setup were modified to allow for optical access from 45° and were anti-reflection coated for the wavelengths 493 nm, 650 nm and for 1.7 μm for future experiments. Positioning of the lenses is modified as well: While in the old setup the lens is held with a long metal tube fixed on a bellows with three interdependent and coarsely operating screws, the new setup is making use of piezo-translation stages (ANP x,y,z 100, Attocube) which allow for positioning the lenses along the directions x'', y'', z'' with very high precision below 50 nm.

The optical axis of the Halo-lenses coincides with the z''-axis so that the observation

name	usage	in plane	orientation along
main	laser	horizontal	$\overrightarrow{e_{x''}}$
45° left	laser	horizontal	$\overrightarrow{e_{x''}} + \overrightarrow{e_{z''}}$
45° right	laser	horizontal	$\overrightarrow{e_{x''}} - \overrightarrow{e_{z''}}$
top	laser	vertical	$-\overrightarrow{e_{y''}}$
top front	laser	vertical	$\sphericalangle$(top front, top) $= -38°$
top back	laser	vertical	$\sphericalangle$(top back, top) $= 38°$
left	observation	horizontal	$-\overrightarrow{e_{z''}}$
right	observation	horizontal	$\overrightarrow{e_{z''}}$
bottom	observation	vertical	$\overrightarrow{e_{y''}}$

Table 4.1: Optical access to the new trap

is along the "left" and "right" channels. Both of them are equipped with custom-made $\lambda/10$ surface quality view-ports to guarantee low wave front abberations. The two observation channels are used in two different ways as shown in the bottom panel of Fig. 4.4. In left channel the collected fluorescence light can be sent to either an intensified CCD camera (Andor Luca), to a PMT or both by making use of a switch box, where a rotatable wheel inserts different mirrors. Both paths are spectrally filtered (Interference filter, Semrock FF01-494/20-25, transmission @493$\pm$10 nm>90%, suppresion 1e-8), the PMT path moreover has an adjustable rectangular slit for spatial filtering followed by a lens to focus onto the PMT aperture. The imaging of the ions is done in a simple way by displacing the left Halo-lens "L1" to a working distance of 14 mm from the trap. Thus a magnification M on the order of $M \sim$13 is obtained corresponding to an object distance of $s_0 = 27$ mm and an imaging distance of $s_1 \sim 333$ mm and a resolution of 1.3μm per pixel. For typical ion distances of 4μm the distance between individual ions is sufficient, i.e. single ions can be distinguished. For laser addressing experiments the magnification should be increased. On the right side, the Halo lens is positioned in order to produce a collimated beam, i.e. the ion is in the exact focal point of the Halo-lens "L2". The calculated working distance for this is 11.8 mm from the trap center. The collimated beam of $\sim$ 20 mm in diameter passes the high-quality view-port and can either be sent to an optical fiber (via flip-mirror M_{fiber}) after passing a telescope for beam size matching or to a back-reflecting mirror for interference measurements as presented below (M_{IF}).

For generating a weak magnetic field three pairs of Helmholtz coils are available, two of them in the horizontal plane, one in the vertical palne. We denote them with "pair 1,2" and "pair vert". The configuration allows for a compensation of the earth magnetic field as well as for a deliberate orientation of the magnetic field in the horizontal direction. In a standard configuration the field is set parallel to the z''-axis, i.e. along the direction of observation.

All other vacuum ports are equipped with standard fused-silica view ports with

anti-reflection coating for the wavelengths 493, 650 and 1762 nm. To allow for optical access in all directions, three CF-16 viewports and one CF-200 in the vertical plane and another 6 CF-64 in the horizontal plane are mounted. Table 4.1 list gives an overview of the optical ports and their properties and should be compared to Fig. 4.4.

For loading of ions in the trap a beam of neutral atoms is sent to the trap center, where the ionization takes place. Two stainless steel tubes of 6 cm length, 3 mm diameter and 0.2 mm wall thickness are filled with Barium grains and heated by a current of around 4 A through it. The tip of the ovens are plugged into holes drilled into one of the macor holders to guarantee a rigid construction and to make sure, that the center of the trap is hit. For low atom flux, the geometrical dimensions of the oven define the collimation of the atomic beam. Investigations showed, that collimation below 1 mm is *not* advisable, since first the atom flux is reduced and second baking of the oven can cause slight derivations from the original target point. More details and investigations of this design are presented in [43]. The ionization procedure is realized with a photo-ionization process as described below. As a back-up system an electron emitter (BaO-disc ES-015, Kimble-physics) is installed for creating ions via electron impact ionization.

4.3 Combined Setup

4.3.1 Arrangement

Figure 4.5 shows a schematic of the actual status of the combined lab system. On the old optical table 1 the two ion trap system are placed together with the entire lasersystem at 493 nm and the photoionisation-lasersystem at 413 nm, while the 650 nm laser-system was already moved to the new table 2. This table also carries the interferometer mounted on an additional breadboard for a later move. One clearly recognizes, that at this intermediate stage of the combined system development, the placement of lasers and experiment vessels is mixed. The final goal is to have all lasers on the optical table 2 and the two traps together with the interferometer on table 1. This has the advantage, that for example radio-frequency pick-ups and other noise-sources can be suppressed. However, the system is fully operational at this stage. A lab computer (not shown) controls the wavelength of the cooling lasers, and is the interface for ion-imaging and analysis of the fluorescence photocurrent.

4.3.2 Laserfields and light distribution

The three lasersystems used at this stage, i.e. 493 nm, 650 nm and 413 nm, are distributed to both traps, where it was decided to send the *same* wavelengths to both of the traps. Thus the distribution is just done with the help of polarizing beam splitters and half-wave retardation plates. A detailed description of the generation of the

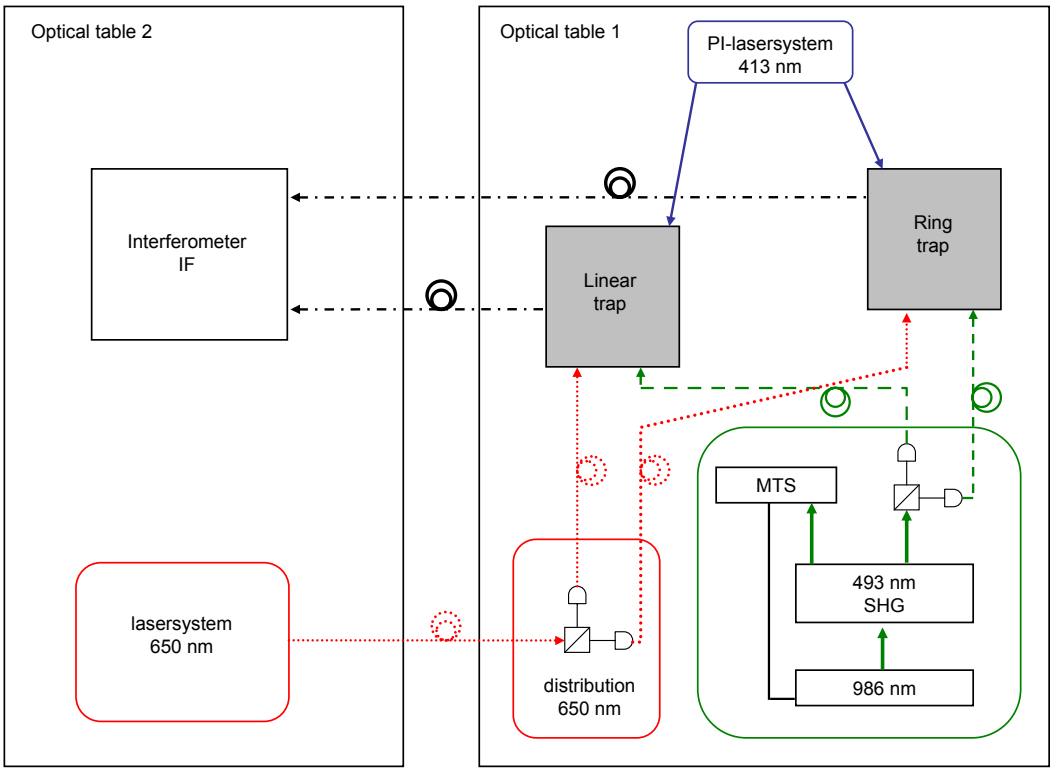

Figure 4.5: Schematics of the combined setup including two traps and the laser-systems.

laserfields at 493 nm and 650 nm is given in [64], we here just present an overview.

The light field at 493 nm is generated with a homebuild 986 nm diode laser in Littman-Metcalf configuration locked to a reference cavity with a Finesse of about 1000. The second harmonic is generated in a $KNbO_3$ crystal placed in one focus of a bow-tie cavity for 986 nm light. The output at **493 nm** is locked using Doppler free modulation transfer spectroscopy (MTS, see [65]) to a Te_2 resonance after being frequency-shifted by $\sim$ 400 MHz in a double-pass configuration. This laser drives the $6S_{1/2}$ to $6P_{1/2}$ in the Barium level scheme. Out of the 30 mW produced power after the doubling cavity up to P_{493}=400 μW are used for illuminating the ions. Another AOM controls the detuning of the laser. The light field is intensity controlled to 1% and has a line width smaller than 60kHz. The light is distributed to the individual traps with two single-mode, polarization maintaining optical fibers.

The second light field at **650 nm** serves to quench the meta-stable $D_{3/2}$ state and is generated by a commercially available diode laser system (Toptica DL 100) in Littrow configuration. Part of the 10 mW output power is used for stabilizing the frequency of the light field to a cavity with Finesse of about 1000 within less than 100 kHz. The remaining power is coupled into a single-mode, polarization maintaining optical

fiber and guided to the optical table 1. There, another distribution stage couples into two additional fibers guiding light to the traps and distributes light to the wavelentgh analysis tools, i.e. a commercially available Fizeau-wavemeter with 10 MHz accuracy and a hollow cathode. The light field is intensity stabilized and can be detuned with the help of a double pass AOM. In total, up to P_{650}=400 μW of light at 650 nm is available to illuminate the ion and to drive the transition from $5D_{3/2}$ to $6P_{1/2}$.

Another commercially available laser-diode system from Toptica (DL 100) generates light for photoionisation at **413 nm**. The output of this grating-stabilized system is directly guided through air to one of the traps after passing a pinhole for mode-cleaning. This light field is neither frequency nor intensity stabilized. Its wavelength is determined by the aid of the Fizeau-wavemeter which is sufficient for fast and efficient loading. Around 2 mW of blue power is needed to be sent to the individual traps to guarantee fast loading times. More details about the photoionization-process can be found in Chapter 5.

4.3.3 Counting electronics

Photon counting is done with photomultipliers (PMT, Hamamatsu H7421-40) selected for a minimal quantum efficiency of 40% at 500 nm and a maximal dark count rate of 75 cps. The experiment is equipped with 4 of these devices, one per trap and two for a Hanbury-Brown and Twiss setup in the interferometer. A single photon detection event is converted into a TTL pulse with a pulse-length of 45 ns by the PMT electronics. The TTL pulses pass through a TTL to NIM converter, a discrimation stage (LeCroy 821) and are then distributed to a photoncounter (LeCroy 3615) and to a time-to-digital converter (TDC, LeCroy 4204 and 3588 Histogram Memory). The photon counts are typically integrated over a time of 100 ms and monitored on the Lab View control programm. The photocurrent can optionally be investigated in the frequency domain by use of a spectrum analyzer (Rohde & Schwarz, FSP 13). Most of the data acquisition in Chapter 4 is done in the frequency domain for which the LabView Programm also controls the settings and read-out the of the spectrum analyzer data.

The photocurrent can also be investigated in a time-resolved measurement, i.e. measuring the arrival time of the photons. As already described before, a Hanbury-Brown and Twiss setup is used to split the photons into two channels and correlations between the channels are obtained. There are two ways to do so as illustrated in Fig. 4.6: In the "so-called" histogram mode a start and a stop channel is defined. An electronic circuit starts a time measurement triggered with the first photon in the start channel and stops it with the second one in the stop channel. The time between these two *successively* detected photons is calculated and written into a histogram. Doing this measurement repeatedly yields a histogram with the number of measured correlations as a function of different time delays with a predefined resolution. There are several drawbacks of this way of measuring photon correlations. First, the time resolution of the histogram is chosen before the measurement and can not be changed at a later

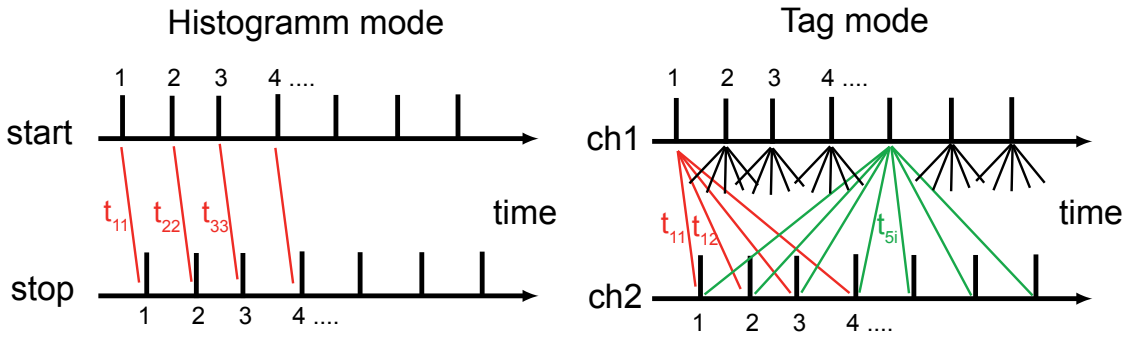

Figure 4.6: Illustration of the "histogram" mode and the time tag mode for correlation measurements.

stage. This postprocessing is not possible. The method is furthermore not efficient in terms of statistics. It has to be made sure, that the stop channel n_{stop} has a higher count-rate than the start channel n_{start}. Otherwise a time measurement is started, but a stop photon never arrives. The devise registers an overflow count. The number of correlations measured is given by the number of start photons n_{start} since the correlations are merely obtained between *one* and *one* photon. In particular, the probability of measuring *long* time intervals is exponentially decreasing since a stop photon yields the electronics to be reset and starts another measurement. The operation principle of the TDC device from above is working like that. Because of the drawbacks, in the measurements reported here the TDC is used for micromotion compensation (correlation) measurements only.

A more elaborate way to measure photon correlations is to rate the time of photons in a stream, i.e. the arrival time and the channel of each photon is noted down into a binary file (PicoHarp 300, PicoQuant). Using these raw data, one is able to calculate the correlations in the following way. The time of photon 1 in channel 1 is taken and compared to photon 1 in channel 2, then with photon 2 in channel 2 and so. Then photon 2 of channel 1 is taken and correlations with all photons from channel 2 are obtained. Indeed, the outcome is a histogram as well, but the raw data are still available and postprocessing is possible. Measurements between two channels are called "cross-correlations" in contrast to "auto-correlations", where just one channel is investigated. The resolution of the time measurement can be as low as 4 ps. The statistics is much more efficient, since each photon is correlated with all others, in particular long time intervals can be measured and no statistical corrections have to be applied. Theoretically, the number of correlations can be as high as $n_{\text{start}} \times n_{\text{stop}}$, but in a realistic situation, the time window of the correlations is limited to a certain region of interest.

5 Trap operation

This chapter gives an overview on the basic steps for operating both traps. The working procedures for preparing the new trap for experiments is almost identical to the old trap. Aside from the principal distinction of both traps regarding geometry and dynamical confinement, differences concern the observation of ions only. The following measurements are all done in the new trap setup and prove it to be fully operational. Indeed, identical measurements are performed with the old setup when preparing it for an experiment. The structure of this chapter follows the daily lab-routine.

5.1 Photo-Ionization procedure

The first step for an ion trap experiment is the production of ions inside the trap volume or transport of ions into the trapping zone. In experiments performed in our group, ions are produced by sending a beam of neutral atoms through the trap center, where an ionization process takes place. Most commonly used methods are either based on a *photo*-ionization process or an *electron impact*-ionization process. Both possibilities differ dramatically in their respective properties and efficiencies. Until 2005, electron impact ionization was used for the old setup before the photo-ionization was introduced.

Extensive studies of photo-ionization vs electron impact ionization are described e.g. in [40] and [43] focussing on the linear trap experiment operating with Calcium in Innsbruck. The results of these studies showed overwhelming advantages of loading with a photo-ionization process summarized in the following points:

- Loading-efficiency: up to 5 orders of magnitude higher.
- Isotope selectivity.
- Suppresses the production of patches and stray fields on the trap electrodes and mounts. As a consequence, compensation fields are constant in time.
- Adjustment: Ionizing laser beam can be installed from outside, laser system can eventually be replaced without breaking the vacuum.
- No heating inside the vacuum chamber.

From this it appears natural to implement photo-ionization procedures in every experiment. In fact, following our line of work most of the ion trapping experiments

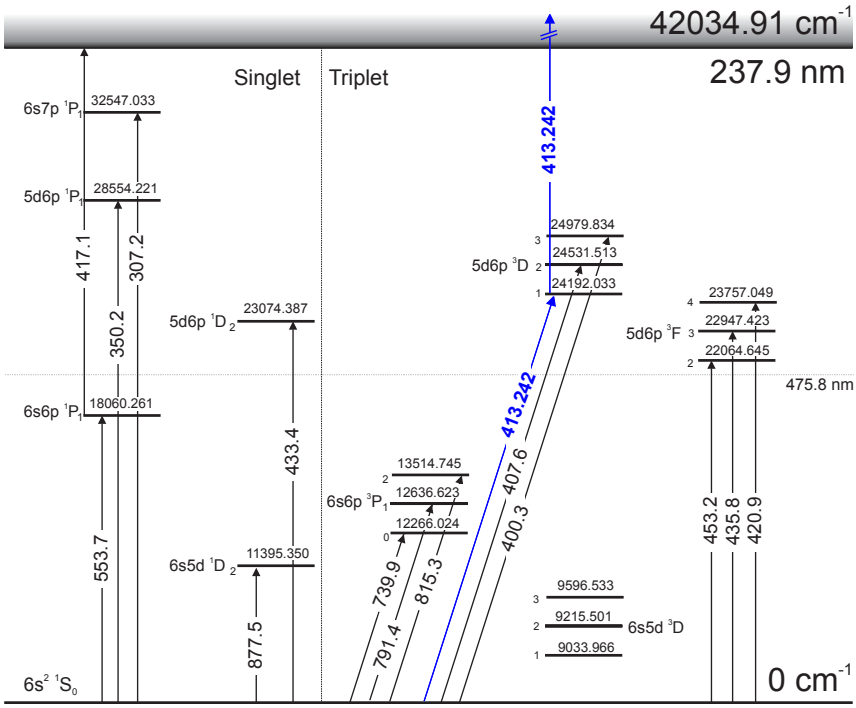

Figure 5.1: Level-scheme of neutral Barium (not complete). Level energies in cm^{-1}, wavelength in air given in nm. The grey area denotes the continuum

world-wide are trying to implement such procedures for ion production. One big limitation is the availability of apropriate lasers for the production of the right wavelength. For economic reasons it is advisable to use cheap and easy to handle diode laser systems.

As an example, the work reported in [40] relies on a resonant two-photon process to ionize neutral Calcium. Here, a resonant excitation from the ground-state $^1S_0$ to the $^1P_1$-state with a laser-field at 423 nm is followed by an excitation into very high lying Rydberg states with 390 nm radiation and a subsequent field ionization in the trapping potential produces the Calcium ions. As suggested in [43], the same method could be applied for Barium as well. In this case, one would need to produce wavelengths at 553.7 nm and 417 nm or lower (see Figure 5.1), which are currently only available with dye lasers. This option was rejected for economic reasons mentioned above.

Several other methods for photo-ionization were studied and are briefly summarized here:

Non-resonant one-photon process with 224 nm radiation.

This method relies on a direct ionization with *one* photon at a wavelength of lower than 238 nm, the ionization limit. One possibility to produce this wavelength would be an HeAg gas-laser emitting at 224 nm. In reference [66] the efficiency of such a process

is studied by studying the absorption spectra of BaI and an absorption cross-section of lower than $1 \times 10^{-18}\,\mathrm{cm}^2$ is measured. Obviously, this method could be optimized by using laser-fields being detuned to auto-ionization resonances[1], but would require a tunable laser-source in the deep UV. Moreover, handling deep UV in a lab can be very tricky and expensive.

Non-resonant two-photon process with 473 nm radiation

An alternative way of using deep UV-radiation is to employ two photons with half the frequency. The ionization limit on the order of 238 nm could in principle be reached by using two photons with 476 nm. Looking at commercially available laser-systems, sources at 473 nm seem to be an appropriate choice, systems at 405 nm seem to be even more efficient. In fact, measurements in [66] show a higher atomic absorption cross section for this process of $2.4\times 10^{-18}\,\mathrm{cm}^2$. From [67], where such a process was applied to Calcium, we find an estimation for the laser-parameters needed: Intensity $I \sim 10^8\,\mathrm{W/m}^2$, pulse-length $\tau \sim 10\,\mathrm{ns}$ and a power of 25 kW. This values should be reachable for a proper focussing and photo-ionization should be possible.

Though these photo-ionization processes have been shown to be working, their principle is based on a (first-order) non-resonant process and is thus not very efficient. We will now consider possible ways for photo-ionization including one resonant excitation.

Resonant two-photon process with 791 nm radiation

During the work of this thesis another group published an ionization scheme in [68]. The method relies on two laser-fields, one resonant with the intercombination line from $^1\mathrm{S}_0$ to the $^3\mathrm{P}_1$-state (see Fig. 5.1) and another one at a wavelength of 337.1 nm to ionize the $^3\mathrm{P}_1$-state. The light fields are produced by a diode-laser and a nitrogen gas-laser. Isotope-selective loading, reasonable loading times and easy laser setups prove this scheme to be very practical.

Resonant two-photon process with 413 nm radiation

The photo-ionization scheme presented and used in this work is comparable to the scheme presented above, though motivated by the work presented in [69]- [74]. The first, resonant step utilizes an intercombination line, from the $^1\mathrm{S}_0$ to the $^3\mathrm{D}_1$-state. As illustrated in the level-scheme in Fig. 5.1, the $^3\mathrm{D}_1$-state is already "high" enough to be ionized by another 413 nm photon. Thus, this method requires just *one* laser source making this method even more practical, very cheap and efficient.

[1] An autoionization-process corresponds to an excitation of both valence electrons, where the overall energy of both electrons is higher than the first ionization energy. One electron transfers the energy to the other one and ionization takes place. Therefore, resonances in the "continuum" can be found, as measured in [66].

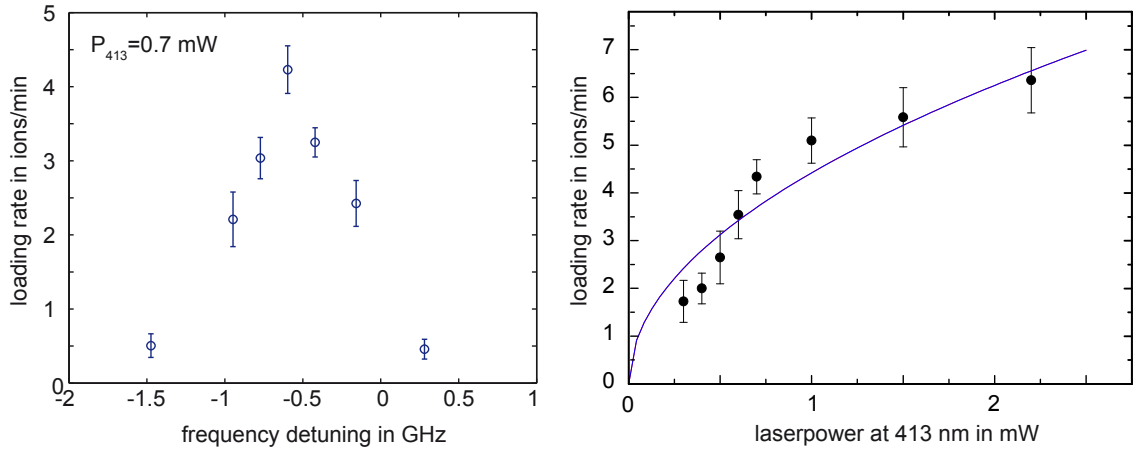

Figure 5.2: *Left:* Loading rate of Barium-ions as a function of laser-wavelength at 413 nm at a constant oven-temperature of 550 K. The 0 denotes the official value for the center wavelength of 413.24266 nm. P_{413}=0.7 mW. *Right:* Loading rate of Barium ions vs. laser power.

In reference [69] it is claimed, that this method of photo-ionization can be realized using a pulsed laser source with the following parameters: Repetition rate ∼10 Hz, linewidth δf ∼15 GHz, pulse duration τ_{pulse} ∼5 ns, a focus of 0.02 cm^2 and a pulse power of P_{pulse} ∼2μJ. From this a peak power of 2 $\times 10^4$ W/cm^2 in 15 GHz bandwidth is obtained. In a CW mode, the same intensity is achieved for P∼10 mW and a focus of∼10 μm, but the spectral bandwidth is at least 3-4 orders of magnitude lower. This estimation indicates, that a CW laser-field with even lower power should be sufficient to perform photo-ionization following this scheme. Moreover, it can be found from [50], that the intercombination line has a center wavelength of **413.24266 nm** and a linewidth of 240 kHz.

The light-field at 413 nm is provided by a Toptica DL100 diode laser-system. After the feedback of the grating and a pinhole configuration for beam-shaping a laser-power of up to P_{413} ∼2.5 mW is available to be sent to one of the traps. Additionally, the light can be sent to a Fizeau-wavemeter with 10 MHz resolution. In front of both traps, the photo-ionization (PI) beam is superimposed with the green and the red light and is sent through the trap along the main channel. In both cases, this configuration is *not* Doppler-free since the atomic beam is pointing towards the laser-direction with a tilt of 17°(40°) for the new (old) setup[2]. From that it is already apparent, that the laser-field has to be slightly detuned to count for the Doppler-shift induced by the velocity of the ions. Calculations, e.g. see [43], are yielding an average Doppler-shift on the order of 600 MHz for Barium atoms at a temperature of 550 K and a "peak" velocity

[2]However, a Doppler-free configuration could easily be installed.

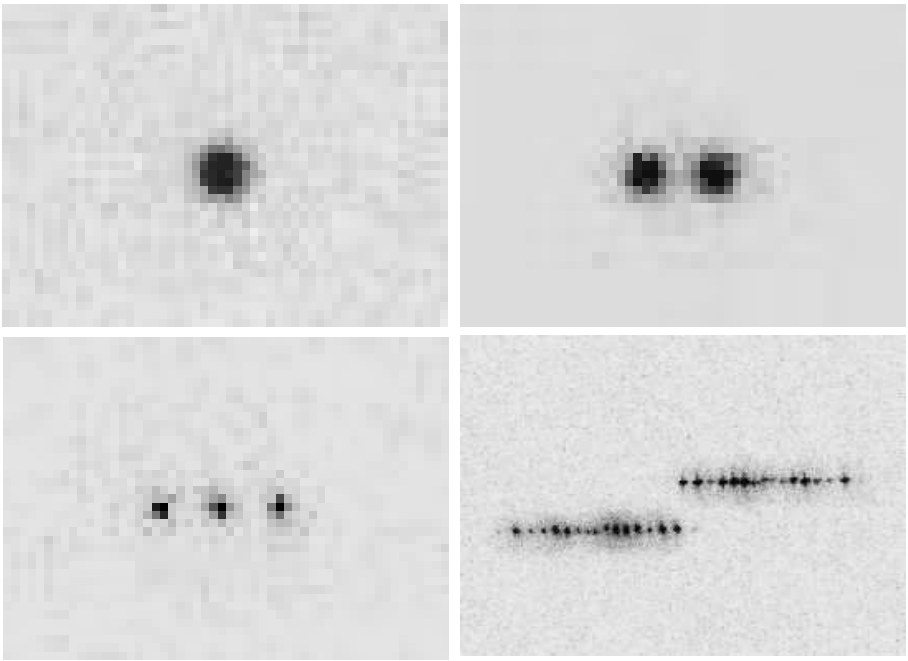

Figure 5.3: CCD images of one, two and three ions on the same region of 54 × 39 pixels. *Bottom right:* Ion string and its mirror image (270 × 195 px).

v=$\sqrt{2kT/m}$ ∼ 250 m/s for which the light-frequency field has to be decreased to maintain full resonance. The calculated frequency shift matches the measured deviation from the literature transition wavelength within the accuracy.

Figure 5.2 presents loading rates obtained in the new trap as a function of the detuning from the center wavelength given in the literature. The shift of the resonance is clearly observable. Typical loading rates are on the order of several ions per minute for a constant pressure close to but lower than 10^{-10} mbar. Apparently, the accuracy of the wavemeter of 10 MHz is absolutely sufficient to set the optimum wavelength for loading. The right panel of Fig. 5.2 shows the loading efficiency as a function of the laser-power.

After the loading process, in the majority of the cases one ion is caught in the trap and can be observed. An inverted image of the CCD camera of one, two and three ions is shown in Fig. 5.3, the right bottom plot shows a string of several ions together with its mirror-image as a preparation for interference measurements as described below.

5.2 Micromotion compensation

In Chapter 2 it was shown, that the trajectory of the ion consists of two parts, one called the secular motion oscillating in the Pseudo-potential and one oscillating at the

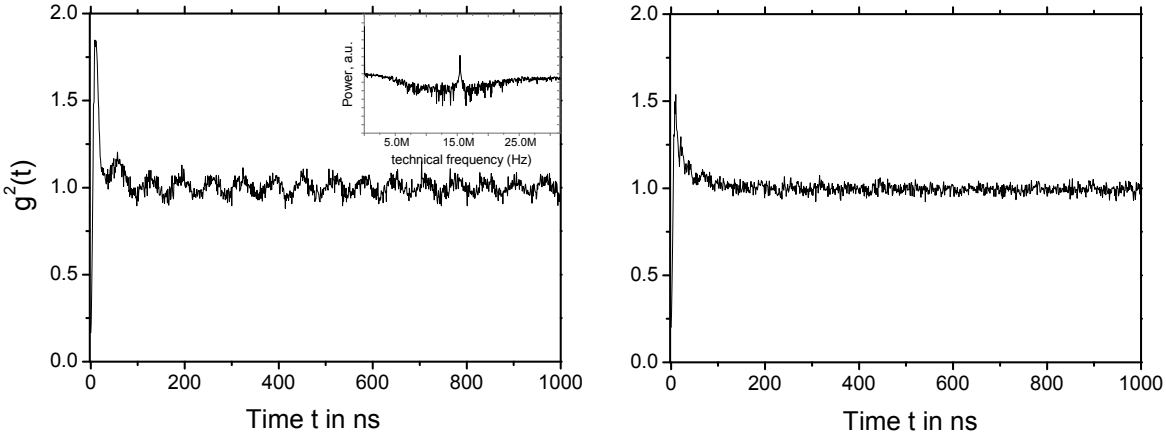

Figure 5.4: Micromotion compensation measured by the photon-photon correlation method.

drive-frequency, the micro-motion. This motion can not be laser-cooled, its relative amplitude can just be minimized by placing the ion in the exact minimum of the radio-frequency potential. Displacements can arise from geometrical imperfections and stray fields, but are usually compensated by using additional electrodes. Thus, after loading one (or several) ions into the trap the micro-motion has to be compensated.

In the setup discussed here, the compensation electrodes are realized by three pairs of electrodes named "top", "bottom" and "side" (cf. Fig. 4.2). Measuring and compensating the micro-motion can be done in very different ways:

- **Coarse compensation:** Since micro-motion is caused by a displacement of the ion from the dynamical trap minimum a rough way to minimize the micromotion is to lower the trap potential and look for a displacement of the ion on a CCD camera. Therefore, the ion position is marked at a high RF power (7-10 W). Displacements of the ion while lowering the trapping potential is compensated for by adding voltages to the compensation electrodes. This procedure can be already sufficient for a lot of applications. In any case, it is a very good starting point, for other methods studied below.

  The method indeed relies on a measurement of the (relative) position of the ion in the trap in all the relevant directions. In the setup presented here, the position of the ion along the observation direction (z"-axis in Fig. 4.4) is in principle not visible. But since the imaging lens produces a very tight focus, a displacement of the ion is observed as a change of the size of the ion spot, which is sufficient for a coarse compensation in this direction.

- **Correlations: Trap-drive ↔ fluorescence:** This method relies on correlations between the trap drive and the fluorescence photons. The displacement

of the ions due to the micro-motion modulates the emitted fluorescence at the drive-frequency due to the Doppler-effect. This modulation can be measured by correlating a fluorescence photon (start) with a TTL pulse obtained from the trap drive (stop) in the TDC "histogram" correlator (see ch. 4). More details can for instance be found in [31, 40]. This way of compensating micro-motion contributions is mainly used for the old setup.

- **Correlations: Photon ↔ photon:** The modulation of the fluorescence can indeed also be seen by measuring photon-photon correlations in the fluorescence. Especially, in a setup, where ($g^2(\tau)$) correlation functions are investigated, this method is apparently the first choice. Beside that, the all optical determination of the micro-motion is automatically ignoring radio-frequency noise or pick-up effects, which might play a role. Moreover, the micro-motion contribution can be integrated into the eight-level Bloch equations such that quantitative measurements of the velocity amplitude can be deduced from both excitation spectra and correlation measurements. This method is in constant use for both trap systems.

- **Minimizing the micromotion sidebands:** The same modulation as discussed above is also visible in the frequency domain as "micro-motion sidebands", when performing spectral analysis of the fluorescence. The micro-motion can be compensated for by minimizing the sideband height[3]. This method is routinely used in the ^{40}Ca linear trap experiment in Innsbruck.

Figure 5.4 shows the measurements for micro-motion compensation in the linear trap after a coarse compensation using the photon-photon correlation method. The plots shows measurements of the correlation function g^2 for times up to $1\,\mu$s obtained by placing one PMT on the observation channel "right" additionally to the one placed on the left. In addition to the anti-bunching feature for time $t = 0$ the micro-motion induced modulation of the fluorescence is clearly visible in the left plot. A Fourier transform of the g^2-function shown in the inset proves the modulation frequency to be equal to the drive frequency of the trap. On the right panel, an optimally compensated micro-motion reveals a flat line.

The micro-motion compensation has to be done once after installation of the setup. The values for the compensation voltages stay constant in time, in particular, if photo-ionization is used for loading ions. The proper compensation voltages differ for different tip voltages, most likely as a consequence of an off-axis alignment of these electrodes. The ion thus feels a tip-induced potential in the radial direction, for which it has to be compensated for.

[3]Here, also higher order sidebands have to be considered. They can also be observed with the correlation methods.

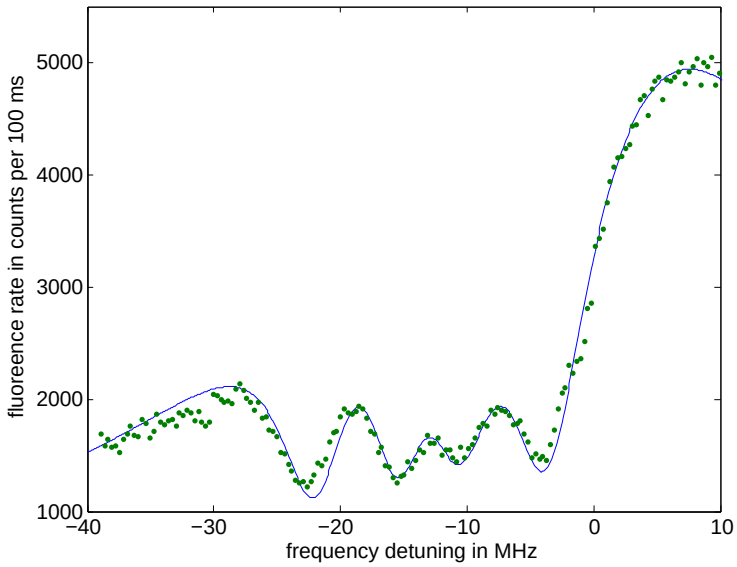

Figure 5.5: Excitation spectrum of Barium. The parameters are: $S_g = 0.95, S_r = 2.5, \Delta_g/2\pi = -13\,\mathrm{MHz}, \delta_\mathrm{g}/2\pi = \delta_\mathrm{r}/2\pi = 200\,\mathrm{kHz}, \mathrm{u}/2\pi = 4.1\,\mathrm{MHz}, \alpha = 95°$. Offset and proportionality factor are adjusted to simulate detection conditions.

5.3 Excitation spectra

After loading ions into the trap (and micro-motion compensation) the next step is to determine the main experimental parameters, i.e. laser intensities and detuning. A very efficient way for this is to record excitation spectra by observing the fluorescence rate of green photons (493 nm) as a function of the detuning of the red repumping light at 650 nm. Excitation spectra can of course also be obtained by detuning the green light or looking at the red fluorescence. Such investigations can for example be found in [52]. However, the standard routine in this experiment is first to roughly tune in all lasers, such that the green laser-field has a negative detuning between -30 and -20 MHz and the red field has just a slight detuning by a few MHz. As a next step, the intensities of both laser-fields are adjusted for a maximum count-rate and are then slightly decreased to avoid saturation. From that starting point, the red laser can be scanned over the dark resonances as described in Chapter 3. The model based on eight-level Bloch equations is used to determine all important parameters, in particular parameters which slightly change from day to day, such as the laser intensities. Other parameters entering the model are laser detunings, the magnetic field, the laser linewidth and the angle between the magnetic field and the polarization.

Figure 5.5 shows an excitation spectrum obtained from the new trap. The parameters are set to typical values with a low green laser power of $S_g = 0.95$ and a relatively high

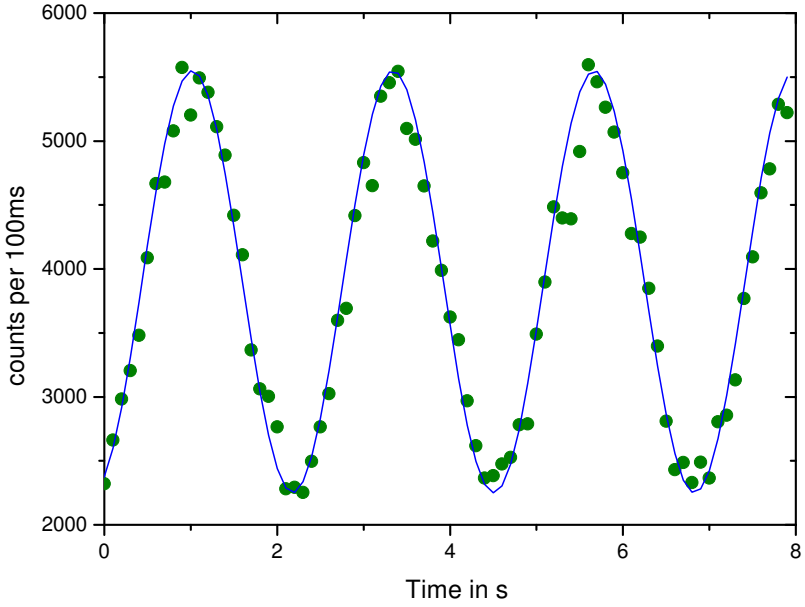

Figure 5.6: Fringes by self-interference of fluorescence photons in the new trap.

red laser-power with $S_r = 2.5$.

5.4 Self-Interference

After the standard operation values for intensities and detunings are set, the next step is to create self-interference of the fluorescence photons[4]. The procedure is identical for both traps.

The Halo lens "L2" inside the vacuum chamber creates a collimated beam with 20 mm diameter, which passes through a high quality vacuum window. The beam is back-reflected by a dielectric mirror (the "distant" mirror) placed at a distance of L with respect to the trap center and mounted on a high precision piezo translation stage (Physical Instruments, P-762-TL, down to 1 nm resolution). The collimated beam is then focussed onto the ion creating a mirror image which can be superimposed with the ion itself. The mirror is coated such that 99% of the green fluorescence is back reflected, whereas fluorescence at the wavelength of 650 nm (emitted on the $6P_{1/2}$ to $5D_{3/2}$ transition) is transmitted and can optionally be used for further analysis.

For a perfect overlap, interference is observed. Its pattern can be scanned by applying a voltage ramp to the Piezo-stage. The count-rate as a function of time (or as a function

[4]The experiment described in Chapter 9 does not need this step

of relative ion-mirror distance) is recorded and plotted in Fig. 5.6. The interference is measured in the new trap setup and shows a visibility of 42% without back-ground subtraction as representing a typical experimental situation. Visibilities as high as 72% were measured during this work. According to Eq. (3.49) and Fig. 3.11 the relative distance between minimum and maximum in the interference pattern corresponds to 120 nm. This measurement proves the high quality of the optics integrated into the new trap-system, i.e. the lens used inside the vacuum chamber, the vacuum window and the mirror used for back-reflection.

As was shown in [28], this interference effect is not a classical interference, but a **self-interference of fluorescence photons**. The probability of having two interfering photons in the setup at the same time is as low as 10^{-4}. This effect is the most important requirement for almost all measurements performed on this experiment and in particular the presented experiments in this thesis.

5.5 Measurement of the radial sidebands

The self-interference can for example be used to determine the motional sidebands of the ion in the trapping potential as pointed out in Chapter 3. For that purpose the so-called "ion-interferometer" has to be stabilized. This is done by actively stabilizing the relative distance between the ion and the mirror with the help of the Piezo-translation stage. A LabView control programm compares the measured photon count rate of the PMT1-channel with a set-value and provides an error signal. A PI controller (proportional integrative controller, SRS SIM960, denoted as "Fringe Lock") regulates and stabilizes the measured count-rate. On a short time scale the ion is oscillating with the secular frequencies and is thus scanning the standing wave of the interference. This leads to an amplitude modulation of the fluorescence which can be observed in the frequency domain.

Figure 5.7 shows the results of this measurement. The left panel depicts the radial secular frequencies centered at 1.675 MHz and at 1.706 MHz after averaging over 500 traces. The sidebands are superimposed on a noise pedestal with frequency dependent power, which is subject of further investigations. The right panel shows the micro-motional sideband centered at the drive-frequency of the new trap. The measurements were done at a radio-frequency power of 7W. The micro-motion sideband in this measurement is centered at the Ω_{rf} =15.088 MHz. In this setup configuration, the axial motion cannot be visualized. The axial motion has no projection along the standing wave of the interference.

For clarity, it should be mentioned, that the measurement of the radial sidebands is not trivial. Without the trick of the self-interference the carrier would conceal the radial sidebands. The self-interference, or in other words the self-homodyning produces a beating between carrier and sideband contributions compareable to measurements performed in [44]. As a consequence, the sideband contributions become visible.

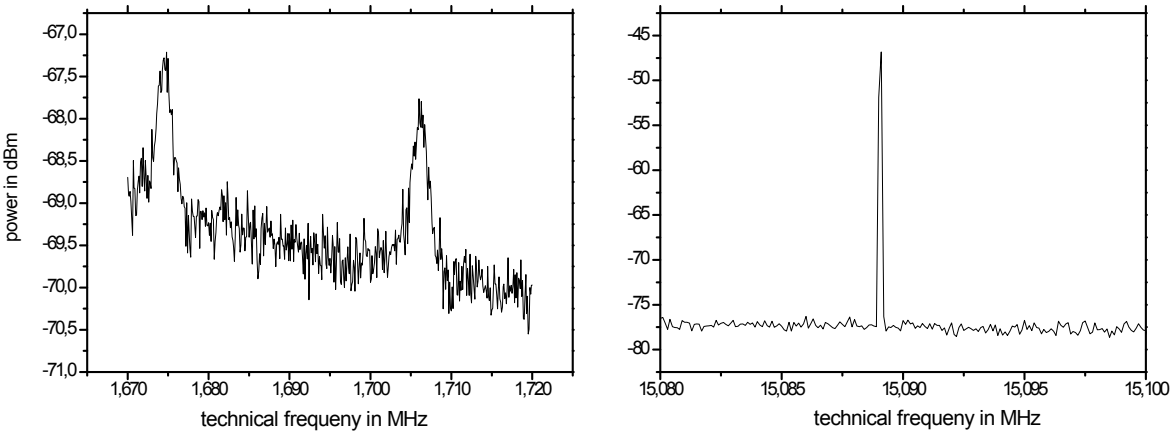

Figure 5.7: Radial sidebands (left) and micro-motional sidebands in the new trap.

6 Quantum feedback cooling

This chapter reports on an experimental demonstration, where the motion of a single ion in a Paul trap is manipulated by means of electro-mechanical feedback. A real-time measurement of the position of the ion based on a self-interferometer setup is source for creating feedback of various kinds. Both electronic *feedback cooling* of the ion below the Doppler limit (cold damping) and *feedback excitation* is measured and investigated by two different theoretical models, one based on classical physics and one based on quantum-mechanics. Moreover, studies inside and outside the feedback loop were performed by coupling out a part of the resonance fluorescence with a beam-splitter. As will be discussed in detail, feedback observations change dramatically depending on a inloop or outloop readout. The presented measurements are successive to experiments described in [32] with a focus on studying different feedback phases.

The key to these feedback experiments is the interference of single resonance fluorescence photons established in the "self-homodyne setup" described in Chapter 3. The high spatial resolution of the latter allows one to observe the motion of the ion in the trapping potential, more precisely, the ion position is permanently monitored. This information is transformed into an electronic signal and is subsequently used to create a feedback signal applied to electrodes of the ion trap. Proper electronic feedback enables one to influence the motion of the ion leading to additional heating or cooling. The feedback operation is quantum-noise limited (shot-noise) and depends on the collection efficiency of the experimental setup. It will be shown, that an effective cooling of 30 % below the Doppler limit is achieved.

Viktor Steixner, Peter Rabl and Peter Zoller developed a quantum-mechanical model for exactly the experiment described here [76]. The most important results of this letter are summarized and discussed in the first section followed by a semiclassical model presented in section 2. Measurements for all types of feedback together with a comparison of the models is found in the last section. The most important results for feedback cooling are summarized in [33].

The experiment presented in this chapter is stimulated by a variety of experiments and theoretical treatises, where feedback control of various systems is investigated [80]-[91].

6.1 Quantum mechanical model: A summary

6.1.1 Homodyne current

As mentioned, the key to the feedback experiments is the homodyne setup and the self-interference of fluorescence photons. In Chapter 3, the intensity of the photo-current measured in such a configuration in the Lamb-Dicke limit was derived in Eq. (3.53), i.e.

$$\begin{aligned} \langle I_c(t)\rangle &= \frac{\gamma}{2}\langle 1 + 2\eta(a_m + a_m^\dagger)(t)\rangle_c + o(\eta^2), \quad \text{where} \\ \gamma &= \epsilon\Gamma_g \frac{\Omega_g^2}{4\Delta_g^2 + \Gamma_g^2} \ , \end{aligned} \tag{6.1}$$

is the optical pumping rate into the mirror channel, Ω_g the Rabi frequency and Δ_g the laser detuning, as before. The index "c" denotes observables obtained from the conditional density matrix. It describes, that each photon count implies a quantum jump of the ion wave function, i.e. a projection into the ground state. The green fluorescence consists of a strong elastic component at zero-frequency (the constant contribution in Eq.(6.2)), and motional side-bands of the order of η which are proportional to the position operator of the ion, $\widetilde{z}_m \equiv a_m + a_m^\dagger$. As mentioned before, this situation is reminiscent of homodyne detection, where a strong component (elastic scattering) beats with a weak one (elastic scattering). Following the formalism of homodyne detection of diffusive processes [75], the measured photocurrent reads

$$I_c^{(h)}(t) = \frac{\gamma}{2} + \gamma\eta\langle\widetilde{z}_m\rangle_c(t) + \sqrt{\frac{\gamma}{2}}\xi(t) \ , \tag{6.2}$$

where $\xi(t)$ is a Gaussian white noise function satisfying $\langle\xi(t)\xi(t')\rangle = \delta(t-t')$. This term arises from the measurement process itself and describes the shot-noise of photon counting experiments. In the diffusion approximation the Poissonian distribution is replaced by a Gaussian (white noise) distribution of the stochastic variable $\xi(t)$. The noise fundamentally limits the sensitivity of photo detection and the quality of quantum feedback operations.

6.1.2 Feedback

In Eq.(6.2) it is shown, that the measured photocurrent continuously follows the mean position of the ion along z, $\langle\widetilde{z}_m\rangle_c$. This information can be used to manipulate the motion of the ion, for instance to further cool it below the Doppler limit, by means of electronic feedback.

The feedback circuit used in the experiment is depicted in Fig. (6.2). The photocurrent $I_c^{(h)}$ is first mixed with a local oscillator of variable frequency and phase (ω_{lo} and φ respectively), and then sent to a band pass filter centered at $\omega_f/2\pi$= 10.7 MHz.

The signal is finally mixed again with the local oscillator, amplified and sent back to the trap electrode. The transfer function of the band pass filter is denoted by $Z(\omega)$. Considering all electronic transformations done to the measured photo-current (signal), the feedback current reads

$$I_{fb,c}(t) = G'_{qm} cos(\omega_{lo} t) \int_{-\infty}^{t} dt_1 \widetilde{Z}(t - t_1) \cos(\omega_{lo} t_1 + \varphi) I_c^{(h)}(t_1) \tag{6.3}$$

where G'_{qm} is the gain of the amplification stage and $\widetilde{Z}(t)$ the Fourier transform of $Z(\omega)$. For a clear separation of dynamics, i.e. the bandwidth of the filter B in the feedback circuit much larger than the cooling rates of the motion of the ion, the feedback current can be expressed as [76]

$$I_{fb,c}(t) = G'_{qm} \left(\gamma \eta \langle X_\varphi \rangle_c^I(t) + \sqrt{\frac{\gamma}{2}} \Xi \right) \cos(\omega_{lo} t). \tag{6.4}$$

In (6.4) the first term, $\langle X_\varphi \rangle$=Tr$\{X_\varphi \widetilde{\rho}_c(t)\}$, is the expectation value of the quadrature component

$$X_\varphi \equiv a_m e^{i\varphi} + a_m^\dagger e^{-i\varphi} \ , \tag{6.5}$$

in a rotating frame. X_φ thus determines the different types of feedback applied, either proportional to the momentum or to the position of the ion. For instance, for φ= -$\pi/2$, feedback is identical and opposite to the momentum operator of the ion, $p_m \equiv i(a_m - a_m^\dagger)$, as shown later. The second contribution in Eq.(6.4) describes the Gaussian noise passing through the band pass filter and reads

$$\Xi(t) = \int_{-\infty}^{t} dt_1 \widetilde{Z}(t - t_1) cos(\omega_{lo} t_1 + \varphi) \xi(t_1) \ . \tag{6.6}$$

This white noise contribution deriving from ξ is the limitation for the reported feedback experiments . It is spectrally flat over a frequency range of B and plays a crucial role for all feedback phases, φ. This noise Ξ is indeed systematically fed back to the ion which then heats up the motion of the ion. Thus, the measurements performed are expected to be shot-noise limited.

6.1.3 Energy vs. gain

The theory developed by Steixner and coworkers employs the formalism of the stochastic Schrodinger equation to express the photocurrent. Based on a general quantum feedback formalism [80], a quantum feedback master equation for the motion of the trapped ion is derived. This allows oneto study the dynamics and limits of quantum feedback cooling. One of the most interesting observables in this system is the energy of the ion and changes of the energy during feedback operations. This quantity is measured as a function of the gain G_{qm} of the feedback circuit. In ion trap experiments the

energy is measured in terms of motional quantum numbers n_{phn}. At Doppler cooling conditions the initial phonon number is $n_{phn,i}$, typically on the order of $n_{phn,i} \approx 15$. The energy of the ion in units of n_{phn} as a function of the feedback-gain G_{qm} and the feedback phase φ taken from [76] is

$$\begin{aligned} \langle n_{phn} \rangle_{ss}^{\varphi} &= \frac{n_{phn,i} - \frac{1}{2}(4n_{phn,i} - 1)\eta\tilde{\gamma}G_{qm}\sin\varphi}{(1 - \eta\tilde{\gamma}G_{qm}\sin\varphi)(1 - 2\eta\tilde{\gamma}G_{qm}\sin\varphi)} \\ &+ \frac{\frac{1}{8}\tilde{\gamma}G_{qm}^2[1 + 4\tilde{\gamma}\eta^2(2n_{phn,i} + 1 - 2\sin^2\varphi)]}{(1 - \eta\tilde{\gamma}G_{qm}\sin\varphi)(1 - 2\eta\tilde{\gamma}G_{qm}\sin\varphi)} \\ &- \frac{\frac{1}{8}\eta\tilde{\gamma}^2G_{qm}^3\sin\varphi}{(1 - \eta\tilde{\gamma}G_{qm}\sin\varphi)(1 - 2\eta\tilde{\gamma}G_{qm}\sin\varphi)} , \end{aligned} \tag{6.7}$$

where $\tilde{\gamma} = \gamma/\Gamma_g$ is the normalized coupling rate into the mirror channel. The equation is structured in powers of G_{qm} and is evaluated for certain feedback phases below.

6.2 The semiclassical model

In this section a semiclassical theory describing feedback control of the motion of the ion is presented. First, the motion of a trapped and laser cooled ion is modelled as a harmonic oscillator coupled to a thermal reservoir, i.e. the cooling laser field. The motional spectrum of the oscillator shows a Lorentzian profile. Consequently, feedback will be introduced in terms of a force derived from the motion of the ion. The analysis includes noise and an arbitrary feedback phase for a general application. Motional spectra *inside* and *outside* the feedback loop are calculated. Additionally, the corresponding oscillator energy as a function of the feedback gain is derived, which allows a comparison to the quantum-mechanical model shown before. In a later stage the generally derived equations will be discussed focussing on a feedback for cooling purposes ("cold damping").

The model presented here relies on the measurement of the (relative) position of the ion. Indeed, this is guaranteed by the homodyne measurement resulting in interference allowing for a high spatial resolution. The semiclassical approach provides a very intuitive access, the ability to determine spectra inside and outside the feedback loop is very close to the experimental work and is moreover essential for determining the feedback phase. The model presented here is based on the work reported in [32, 81, 95] and partly reproduces the cited work for the sake of clarity. Moreover, the model is applied to our experimental conditions and generalizes the approach in terms of implementing an arbitrary feedback phase and noise contributions.

6.2.1 The single ion harmonic oscillator and Doppler cooling

An ion held in a Paul-Trap is a very well isolated harmonic oscillator. As for any macroscopic system, the thermal environment determines the energy of the oscillator, i.e. following the equipartition theorem, each motional degree of freedom is driven by a thermal random force, i.e. the Langevin force. In the system studied here, the thermal bath is the ensemble of cooling laser fields. The dynamics of laser cooling is decribed in [48] in terms of light pressure forces induced by absorption and emission events. There, an expansion of the light pressure force in the velocity is leading to a frictional damping term describing the interaction between an oscillating ion and the laser (thermal) bath.

As a consequence, the motion of the single trapped ion under Doppler cooling conditions can be approximated by a driven harmonic oscillator coupled to a reservoir leading to the following equation of motion

$$\ddot{r} + \Gamma\dot{r} + \omega_t^2 r = F_L(t)/m \ , \tag{6.8}$$

where Γ is the damping or cooling rate of the oscillator, ω_t the angular frequency of its mechanical oscillations, m the mass of the oscillator and $F_L(t)$ the Langevin force describing spontaneous emission of photons. We denote the position of the ion by a general and for simplicity one-dimensional r. The position of the ion as a function of the frequency can be expressed in terms of the mechanical susceptibility of an oscillator $\chi(\omega)$, and reads

$$r(\omega) = \chi(\omega)F_L(\omega) \ , \tag{6.9}$$

where ω is the frequency variable. Squaring the frequency components is leading to the spectral density of motion

$$S_r(\omega) = |\chi(\omega)|^2 S_{F_L}(\omega) = \frac{S_{F_L}(\omega)}{m^2}\frac{1}{(\omega_t^2-\omega^2)^2+\Gamma^2\omega^2}, \tag{6.10}$$

where $S_{F_L}(\omega) = |F_L(\omega)|^2$ is the energetic spectral density of the Langevin force, and can be calculated with the help of the mechanical susceptibility of an oscillator $\chi(\omega)$ by using the Fluctuation-Dissipation Theorem (FDT) [92] yielding

$$S_{F_L}(\omega) = \frac{\hbar\ \mathrm{Im}\{\chi(\omega)\}}{|\chi(\omega)|^2}\ \coth\left(\frac{\hbar\omega}{2k_BT}\right) \ . \tag{6.11}$$

For $k_BT \gg \hbar\omega$ (classical regime) ω can be neglected in Eq. (6.11) and the spectrum of the Langevin force becomes constant in frequency space. By introducing S_{F_L} into Eq. (6.10) one obtains

$$S_r(\omega) = |\chi(\omega)|^2 S_{F_L}(\omega) = \frac{2\Gamma k_BT}{m\omega_t^2}\frac{1}{4\Delta^2+\Gamma^2} \ . \tag{6.12}$$

We have considerd the region close to resonance, i.e. $\omega_t^2 - \omega^2 \approx 2\omega_t\Delta$ and $\omega_t \approx \omega$, where $\Delta = \omega_t - \omega$ is defined as the detuning. The spectrum of a single trapped and laser cooled ion thus has a Lorentzian profile.

The temperature of the thermal bath driving the ion motion is determined by the balance of laser-induced cooling and spontaneous heating process. It is connected to the thermal energy E_0 of the ion by

$$E_0 = \hbar\Gamma_{P,tot}/2 = k_B T_0. \tag{6.13}$$

$\Gamma_{P,tot}$ is the total linewidth of the radiative transitions from the $P_{1/2}$ to the $S_{1/2}$ state and the $P_{1/2}$ to $D_{3/2}$ state for the Ba^+ ion (see Fig.3.1). E_0 can be expressed in terms of the phonon number expectation value, $\langle n_{phn}\rangle$, for a quantized oscillator to provide a comparison to the quantum-mechanical approach.

The mean position variance can be calculated by integrating the spectral density $S_r(\omega)$ over ω and represents the equipartition theorem; it reads:

$$\langle r^2\rangle = \frac{1}{2\pi}\int_{-\infty}^{\infty} S_r(\omega)d\omega = \frac{k_B T_0}{m\omega_t^2}. \tag{6.14}$$

For convenience the spectral power density of the motion can be presented as

$$S_r(\omega) = \frac{2\langle r^2\rangle\Gamma}{4\Delta^2 + \Gamma^2}. \tag{6.15}$$

After having derived the spectrum of motion of a Doppler cooled ion in a Paul trap, we want to study the behavior of the system under feedback.

6.2.2 Feedback

In the language of the semiclassical model, the motion of the ion is observed as a modulation of the homodyne photocurrent at the trap frequencies ω_t yielding sidebands in the frequency domain (described by Eq. (6.15)). As can be seen from Eq. (6.2), the modulation appears only for a high precision measurement of the position of the ion. Since a comparison between the quantum mechanical and the semiclassical descriptions will be made at a later stage, the position of the ion is denoted by $z_m(\omega)$ in the following, the projection of the position coordinate of the ion onto the mirror axis, instead of the general notation $r(\omega)$. Regardless of the realization of any back-action, the feedback is described as an additional force acting on the ion's motion leading to

$$z_{m,FB}(\omega) = \chi(\omega)[F_L(\omega) + F_{FB}(\omega)] \ . \tag{6.16}$$

The feedback force can be written in a general form like

$$F_{FB}(\omega) = \omega\Gamma G m e^{-i\varphi}(z_{m,FB}(\omega) + s_{in}(\omega)) \ , \tag{6.17}$$

where G is the feedback gain and φ the phase of the feedback loop. Additionally, a noise contribution, $s_{in}(\omega)$ being the noise amplitude present inside the feedback loop, is formally introduced. The feedback driving the ion motion thus consists of one part generated by the position measurement and a second part guided by an inherent existing (shot-) noise. Inserting Eq. (6.17) into Eq. (6.16) leads to

$$z_{m,FB}(\omega) = \frac{F_L}{1/\chi(\omega) - \omega\Gamma G m e^{-i\varphi}} + \frac{\omega\Gamma G e^{-i\varphi} s_{in}}{1/\chi(\omega) - \omega\Gamma G m e^{-i\varphi}} \ .$$

Following the procedure of the previous subsection and introducing the feedback variables

$$\begin{aligned} \Gamma_{FB} &= \Gamma - G\Gamma \sin\varphi \\ \Delta_{FB} &= \Delta - \frac{\Gamma G}{2}\cos\varphi \ , \end{aligned} \tag{6.18}$$

results in modified spectra. Mixed contributions, i.e. contributions proportional to $F_L \cdot s_{in}$ vanish due to a missing correlation. The spectrum under feedback conditions then reads

$$S_{z_m,FB} = \frac{2\langle z_m^2\rangle\Gamma + S_{in}\Gamma^2 G^2}{4\Delta_{FB}^2 + \Gamma_{FB}^2} \ . \tag{6.19}$$

The variable $S_{in} = |s_{in}|^2$ describes the spectral density of the noise in the in-loop channel. The spectrum of the oscillator under feedback still stays Lorentzian, but with a modified width and detuning. Comparing Eq. (6.15) and Eq. (6.19) clearly shows, that the feedback adds a noise contribution being proportional to gain squared, G^2.

Now the dependence of the energy of the ion oscillator as a function of the feedback gain, G, should be discussed. The position variance under feedback conditions is obtained by evaluating the integral

$$\begin{aligned} \langle z_{m,FB}^2\rangle &= \frac{1}{2\pi}\int_{-\infty}^{\infty} S_{z_m,FB}\ d\omega = \\ &= \langle z_m^2\rangle \frac{\Gamma}{\Gamma_{FB}} + \frac{S_{in}G^2}{2}\frac{\Gamma^2}{\Gamma_{FB}} \ , \end{aligned} \tag{6.20}$$

and inserting this equation into the energy of the harmonic oscillator. Normalizing to the zero gain energy leads to

$$\frac{E_{FB}\ (G)}{E_0\ (G=0)} = \frac{m}{kT}\ \omega_{FB}^2 \left(\langle z_m^2\rangle \frac{\Gamma}{\Gamma_{FB}} + \frac{S_{in}G^2}{2}\frac{\Gamma^2}{\Gamma_{FB}} \right), \tag{6.21}$$

where we have defined a new oscillation frequency

$$\omega_{FB} = \omega_t - \frac{G\Gamma}{2}\cos\varphi. \tag{6.22}$$

Equation (6.21) contains all the information about the energy of the ion oscillator as a function of the feedback gain. Furthermore it describes several kinds of feedback, i.e. different feedback phases. Obviously, since the energy depends only on the average of the position measurement, $\langle z_m^2 \rangle$, a noise contribution coming along with the position measurement averages out and does not change the energy dependence. Nevertheless, in a realistic situation, the instantaneous position has indeed an additional noise term, in the present derivation denoted as s_{in}. This property yields distinct situations inside and outside the feedback loop, since the intrinsic noise is also part of the driving feedback force (see Eq. (6.17)). The effect of these two different situations can be especially observed in the spectra of motion, because to obtain the spectra amplitudes have to be added up before squaring . This circumstance will be discussed in the following.

6.2.3 In-loop and Out-loop spectra of motion

The measured position is comprised of two parts, the precise position and a noise term. This yields

$$z_{m,FB,in-loop}(\omega) = z_{m,FB}(\omega) + s_{in}. \tag{6.23}$$

Inserting Eq. (6.16) into the equation above clearly shows, that the noise amplitude s_{in} in Eq. (6.23) has to be added with a term $\propto Ge^{-i\varphi}s_{in}$ coming from Eq. (6.17). Therefore, depending on the phase, a cancelling and even a reduction of the noise in the in-loop spectrum can take place (Fig.6.4). This effect is for example observed in closed opto-electronic loops [96] and was coined "anti-correlated state of light". Squaring the position modulus, $|z_{m,FB,in-loop}(\omega)|^2$, and applying the same approximations as before provides the spectrum measured inside the feedback loop. It reads

$$S_{z_m,FB,in-loop}(\omega) = \frac{2\langle z_m^2 \rangle \Gamma + (4\Delta^2 + \Gamma^2) S_{in}}{4\Delta_{FB}^2 + \Gamma_{FB}^2} \ . \tag{6.24}$$

We additionally introduce a new variable, A, a fitting parameter proportional to the experimental Signal-to-Noise ratio (SNR), $A = 2\langle z_m^2 \rangle / \Gamma S_{in}$ at resonance. Reformulating Eq. (6.24) finally leads to

$$S_{z_m,FB,in-loop}(\omega) = \frac{4\Delta^2 + (1+A)\Gamma^2}{4\Delta_{FB}^2 + \Gamma_{FB}^2} \ . \tag{6.25}$$

By contrast, the out-loop spectrum, $S_{z_m,FB,out-loop}$, is determined by summing up the already evaluated spectrum under feedback conditions (6.19) and a noise term, which is *not* correlated with the shot-noise produced inside the feedback loop, i.e.

$$S_{z_m,FB,out-loop}(\omega) = S_{z_m,FB} + S_{out} \ . \tag{6.26}$$

As a consequence, the out-loop spectrum of motion never shows a noise reduction making this signal an ideal measure to evaluate the energy of the ion motion as a

function of the feedback gain. On the other hand, the in-loop spectrum does show a noise reduction. This makes the in-loop signal unsuitable to measure the energy of the ion oscillator, but - as being sensitive to the phase - a proper way to determine the kind of feedback applied. Therefore, the in-loop spectra are of deep interest as a direct measure of the feedback phase, as will be shown later.

6.3 Experiment

6.3.1 Experimental Setup

The barium ion is laser-cooled by the two light-fields at 493 nm and 650 nm wavelength. The green fluorescence is collected with the Halo-lens L2, and sent to the distant mirror situated at a distance of $L \approx 25$ cm. Lens L1 collects both the directly emitted and the reflected light, focusses it onto a pinhole and sends it a 50/50 beam splitter. Transmitted light is detected by photo-multiplier one (PMT1), reflected light by PMT2. Photon counting and experiment control is done following the description in Chapter 4. Spectrum analyzers (FSP) investigate the measured photo-current in the frequency domain.

The signal of PMT1 is used to stabilize the ion mirror distance with high precision (fringe lock) by acting on the piezo-translation stage (PZT). Moreover, a copy of that signal is used for the electronics (red box) creating the feedback sent to the ion. Thus, this channel is defined as the inloop channel. The observation in the outloop channel allows for feedback independent analysis. All parameters are controlled, set and recorded with a LabView programm (PC).

6.3.2 Feedback electronics

The aim of the feedback electronics (see Fig.6.2) is to control the amplitude and the phase of the input signal, i.e. the photocurrent. The latter consists of an RF-modulation at the ion's oscillation frequency $\omega_t/2\pi$ (sideband) above the shot noise. The input signal is first low-pass filtered. To select a sideband, it is then mixed with a Local Oscillator (LO) wave at a frequency of 10.7 MHz + $\omega_t/2\pi$ to match to the central frequency (10.7 MHz) and the bandwidth (30 kHz) of a band-pass filter (IF 10.7 MHz). The amplitude of the signal is amplified with a fixed gain (AD-829) and is controlled with a bi-phase variable attenuator to avoid phase shifts for variable gain. The signal is then mixed down to its initial frequency with the same but phase-shifted (2x SPH-16) LO wave. A low pass filter cancels signals appearing at the frequency sum of the mixing products. A buffer amplifier at the output is finally used to match the 50 Ohm output impedance to the total impedance of the end cap electrodes of the trap at the sideband frequency.

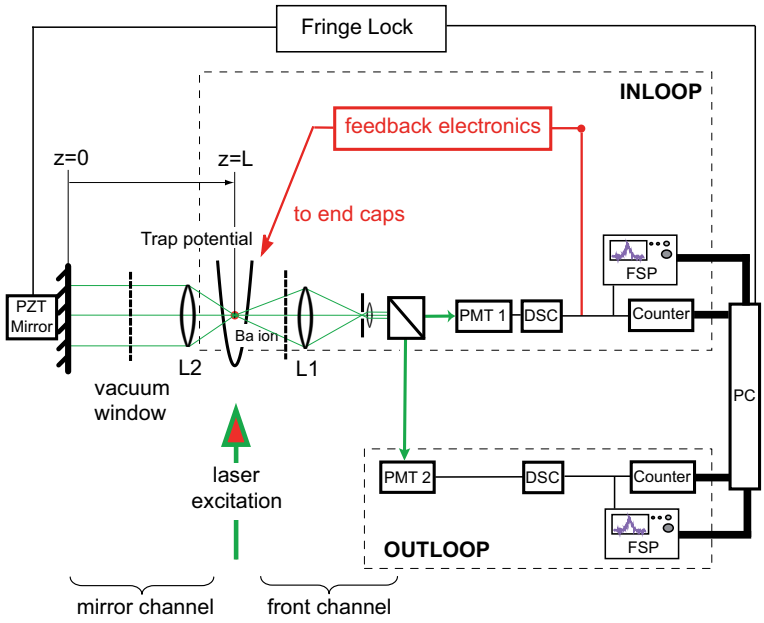

Figure 6.1: Schematics of the setup: For details see text.

6.3.3 Sideband detection

The motion of the ion in the trapping potential can be decomposed into the three normal modes with frequencies ω_x, ω_y and ω_z along x_t, y_t and z_t in the RF pseudo potential. All these oscillations change the position of the ion on a sub-wavelength thus leading to a modulation of the resonance fluorescence at these frequencies. Equation (6.2) describes the different contributions observed in the photocurrent as a function of time. The most interesting is the first term in Eq. (6.2), $\gamma\eta\langle\widetilde{z}_m\rangle_c(t)$, containing the real-time position measurement ($\propto \langle\widetilde{z}_m\rangle_c(t)$) of the ion, where of course all the three motional contributions can enter. This term is, as describing the first motional sideband, a factor of η weaker than the carrier transition. Additionally, the photocurrent carries Poisson noise (shot noise), modelled as Gaussian white noise in Eq. (6.2), ($\sqrt{\frac{\gamma}{2}}\xi(t)$), whose origin is the photon stream statistics.

In the frequency domain, a strong carrier at zero frequency and three motional sidebands ω_x, ω_y, ω_z displaced from the carrier are superimposed on a noise pedestal spectrally flat over the entire observed range, i.e. the shot noise level. Figure 6.3 shows a typical photocurrent spectrum zoomed at the frequencies of interest, $\omega_x/2\pi \sim 1\,\mathrm{MHz}$ (X-sideband) and $\omega_y/2\pi \sim 1.2\,\mathrm{MHz}$ (Y-sideband). The spectra are normalized to the shot noise level and are taken with all the fluorescence coupled into the PMT1 channel. Analyzing the spectra enables one to determine the laser cooling rate Γ, i.e. the width of the sideband, and the motional energy of the ion, E_0, given by the area under the sideband. In Fig. 6.3 the excitation is done with the main beam (see Fig. 4.1) leading

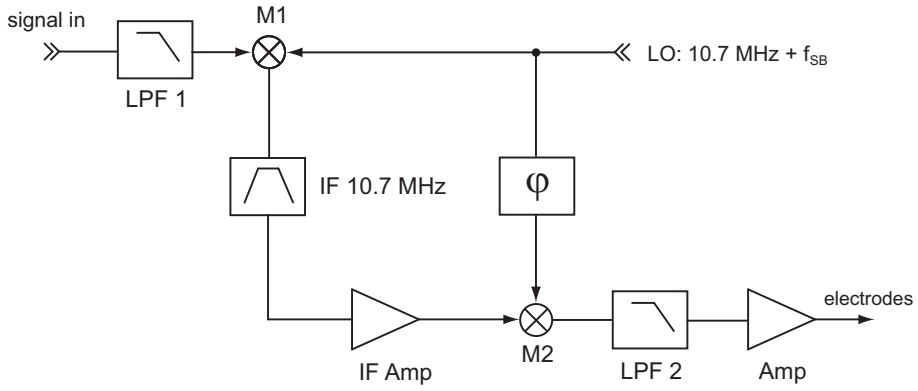

Figure 6.2: Schematics of feedback electronics. The photocurrent modulated at f_{sb} (signal in) is mixed to a frequency at 10.7 MHz (M1), filtered and mixed down again (M2) with the same local oscillator whose phase can be altered generating a phase shifted signal at f_{sb}.

to an equal cooling rate of the X- and Y-sideband on the order of 450 Hz, whereas the motion along z ("Z-sideband") is not observable due to an optimal cooling process.

6.3.4 Feedback

The information of the position and the motion of the ion is used to apply electronic feedback. While different feedback phases are presented to give a complete analysis, the main subject is to study feedback leading to a reduction of the ion's energy, i.e. electro-mechanical cooling.

The feedback was described quantum-mechanically in section 6.1 in terms of the feedback current (Eq. (6.4)) containing the operator $\langle X_\varphi \rangle_c^I(t)$ counting for different phases. Additionally, $\sqrt{\frac{\gamma}{2}}\Xi$, describes the shot noise present in an experiment based on photon counting. In the semiclassical model the feedback is described as different forces (Eq. (6.17)) depending on a phase factor. As in the quantum mechanical model, we also find a noise term, denoted as s_{in}.

The feedback phase plays a dominant role in the following experiments. It originates from the phase of the ion motion and needs to be stable over several feedback operations. By comparing the cooling ratio, $\Gamma/2\pi \approx 400\,\mathrm{Hz}$, and the ratio of feedback determined by the bandwidth of the loop filter, $B/2\pi = 30\,\mathrm{kHz}$, one can see, that this requirement is fulfilled. Furthermore, the phase of the feedback applied to the ion needs to be precisely determined. A callibration relying on the inloop-spectra will be shown in the following section.

In addition, the feedback current contains all components of the motion of the ion, i.e. all visible secular sidebands. By mixing the input signal with the right frequency of the local oscillator, a desired sideband is selected on which feedback is acting on. Thus

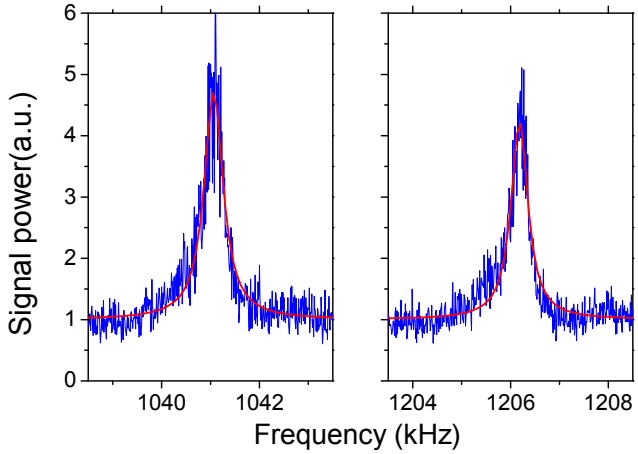

Figure 6.3: X and Y- sideband (from the left) for Dopplercooling with the mainbeam (Z sideband not observable). The spectra are normalized to shot-noise. The sidebands show roughly the same heights corresponding to equal cooling conditions. Parameters: $\Gamma_x/2\pi = 470 \pm 20\,\mathrm{Hz}$ and $\Gamma_y/2\pi = 420 \pm 20\,\mathrm{Hz}$, RBW=10 Hz.

the presented feedback operations are one-dimensional. Spectra are typically recorded within 20 to 30 seconds depending on the resolution (typically 10 Hz) and the number of averages (typically 150).

In-loop spectra and phase determination

The inloop-spectra described by Eq.(6.25) determine the feedback phase experienced by the ion. This phase can also be evaluated by pure electronic analysis. A combination of both methods was used in the experimental work.

Figure 6.4 shows In-loop spectra for different feedback phases, i.e. $\varphi = -\pi/4$, $-\pi/2$, $5\pi/4$, π. Furthermore the relevant sideband without any feedback applied (no FB, $G = 0$) is shown in the top middle of the figure array. The plot shows that the measured phase-dependent changes in the In-loop spectra are nicely reproduced by the semiclassical calculations. The case $\varphi = -\pi/2$ offers, due to symmetry reasons, a proper measure for the overall feedback phase the ion experiences. Taking this phase as a calibration and measuring the electronic phase shift of the circuit allows for a determination of the phase within $\pm 3°$.

In the following different cases of feedback should be selected. The systematic analysis first shows the results of a quantum-mechanical approach followed by the semiclassical investigation. After a comparison, experimental In-loop and Out-loop results are shown for different feedback gains.

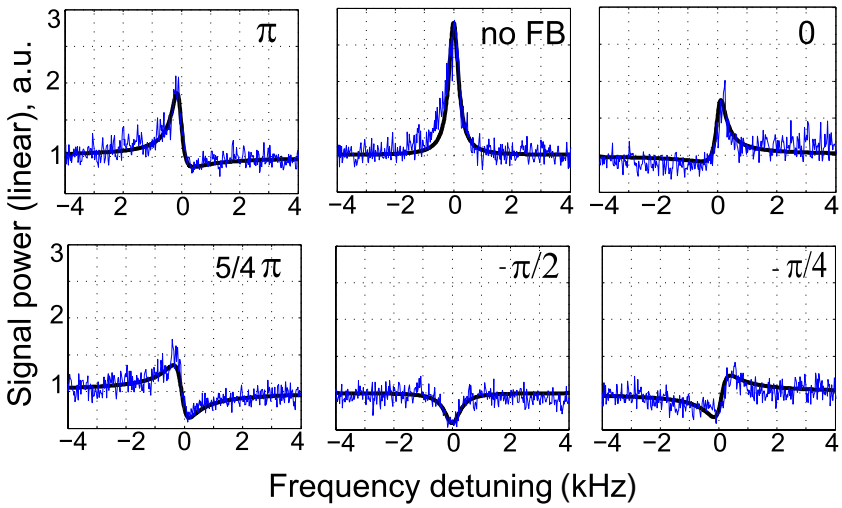

Figure 6.4: Sidebands recorded inside the feedback loop (inloop) for different feedback phases. The case of a $\pi/2$ feedback phase is shown in figure 6.6. The full line shows the result of Eq. (6.25) for A=0.6, $0.35 < G < 0.6$ and varying phases.

Feedback with phase ($-\pi/2$)

This case refers to the so-called cold damping, where oscillators are damped by applying a viscous force, i.e. a force proportional and opposite to the velocity of the ion. The signal derived from the measurement is proportional to the position, as described in Eq. (6.4). For $\varphi = -\pi/2$, $X_\varphi \equiv a_m e^{i\varphi} + a_m^\dagger e^{-i\varphi}$, the operator defining the kind of feedback, becomes $X_\varphi = i(a_m^\dagger - a_m)$, proportional and opposite to the momentum operator, $p_m \equiv i(a_m - a_m^\dagger)$, as desired. In the quantum-mechanical model the normalized energy of the ion written in terms of the mean phonon number reads (cf. Eq. (6.27))

$$\frac{\langle n_{phn}\rangle_{ss}^{-\pi/2}}{n_{phn,i}} = \frac{n_{phn,i} + \frac{1}{2}\eta\tilde{\gamma}(2n_{phn,i}-1)G_{qm} + \frac{1}{8}\tilde{\gamma}G_{qm}^2}{n_{phn,i}(1+2\eta\tilde{\gamma}G_{qm})} \,. \tag{6.27}$$

In the semiclassical description one finds the dependence for the energy of the ion under feedback operation by evaluating Eq. (6.21) for the phase $-\pi/2$. In that case Eq. (6.21) becomes

$$\frac{E_{\varphi=-\pi/2}\,(G)}{E_0\,(G=0)} = \frac{1}{1+G} + \frac{1}{A}\,\frac{G^2}{1+G} \,. \tag{6.28}$$

The first term in the energy relation shows a $1/(1+G)$ dependence leading to a reduction of the energy for an increasing gain. The second term weighted by G^2 describes a driving of the ion's motion by the intrinsic noise. These two competing terms lead to a decreased energy for low gains and an increasing energy for high gains dominated

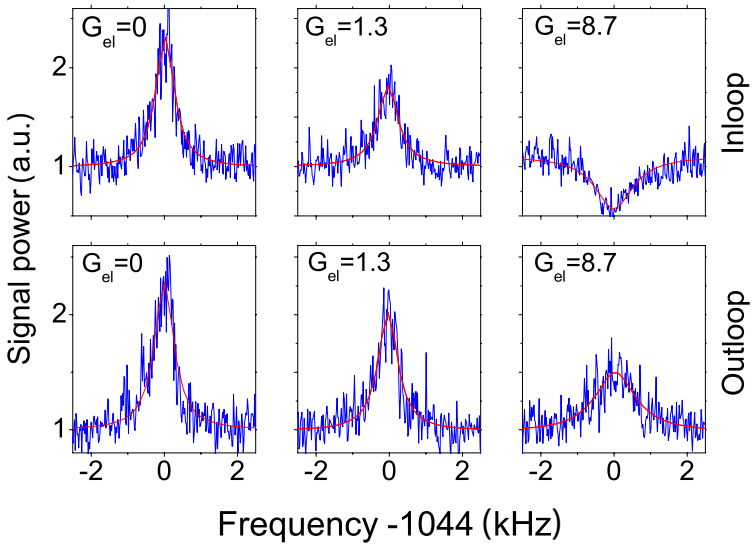

Figure 6.5: The X-sideband under feedback operation with optimal phase (-$\pi/2$): The three figures on top are recorded inside the feedback loop (inloop), the lower ones outside the feedbacl loop (outloop). We measure linewidths of $\Gamma_{G=0}/2\pi = 635(30)$Hz, $\Gamma_{G=1.3}/2\pi = 650(30)$Hz, $\Gamma_{G=8.7}/2\pi = 1340(100)$Hz in the outloop spectra. No frequency shift is measured.

by noise feedback. One finds a similar behavior in Eq.(6.27). One term proportional to $1/(1 + \text{const G})$ describing cooling and a term $\propto G^2/(1 + \text{const G})$ describing the heating due to noise. While the classical approach depends just on one parameter, A, the q.m. models keeps track of all individual, experimental parameters.

Evaluating Eq.(6.18) shows the physical properties of this kind of feedback. The damping rate and the detuning are modified, such that

$$\begin{aligned} \Gamma_{FB} &= \Gamma(1+G) \\ \Delta_{FB} &= \Delta \ , \end{aligned} \tag{6.29}$$

leading to an increased damping rate with increasing gain, whereas the detuning remains unchanged, i.e. no frequency shift is observed. This implies, that this kind of feedback provides cooling of the ion oscillator by increasing the friction force, a force being proportional but opposite to the velocity of the ion.

The results of this special feedback operation is shown in Fig. 6.5 for observing the signal inside the feedback loop (upper row) and for outside (lower row), respectively. While in the top, right plot of Fig. 6.5 a noise reduction caused by an electronic cancelling of the shot noise and its feedback can be clearly observed, the bottom most right plot of Fig. 6.5 does not show the noise reduction anymore, thus revealing pure damping of the ion motion. An increase of the damping rate, Γ, with an increasing

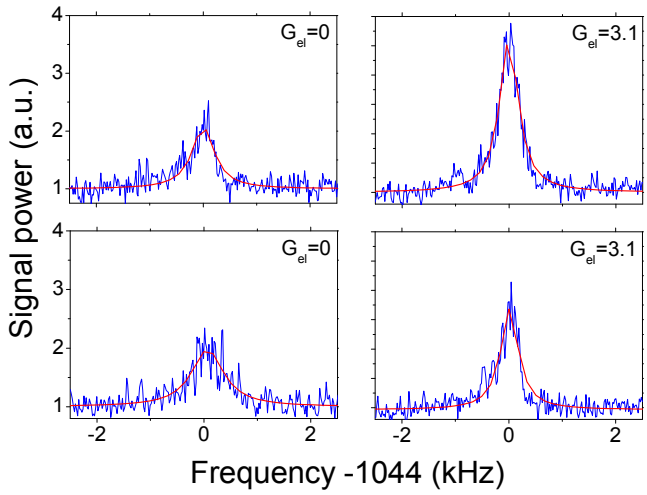

Figure 6.6: The X-sideband under feedback operation with phase $(\pi/2)$: The top figures show inloop spectra, the lower ones outloop spectra. The measured linewidths (outloop) are $\Gamma_{G=0}/2\pi = 740(40)$Hz and $\Gamma_{G=3.1}/2\pi = 400(20)$Hz. No frequency shift is measured.

gain is observed, but no frequency shift.

Feedback with phase $(\pi/2)$

The feedback discussed here is a feedback proportional to the momentum operator as in the case of feedback with phase $-\pi/2$, but with opposite sign. This can be seen by evaluating $X_\varphi \equiv a_m e^{i\varphi} + a_m^\dagger e^{-i\varphi}$ for $\pi/2$, i.e. $X_\varphi = i(a_m - a_m^\dagger)$, thus a feedback leading to heating is expected. The ion energy vs gain relation from Eq. (6.27) reads

$$\frac{\langle n_{phn}\rangle_{ss}^{\pi/2}}{n_{phn,i}} = \frac{n_{phn,i} - \frac{1}{2}\eta\tilde{\gamma}(2n_{phn,i}-1)G_{qm} + \frac{1}{8}\tilde{\gamma}G_{qm}^2}{n_{phn,i}(1-2\eta\tilde{\gamma}G_{qm})}. \tag{6.30}$$

Only for $G_{qm} < 1/(2\eta\tilde{\gamma})$ the quantum mechanical theory predicts a steady-state. One finds a $1/(1-\text{const G})$ and a term $\propto G^2/(1-\text{const G})$.

The energy relation derived from the semiclassical model for that case reads

$$\frac{E_{\varphi=\pi/2}\ (G)}{E_0\ (G=0)} = \frac{1}{1-G} + \frac{1}{A}\ \frac{G^2}{1-G}\ . \tag{6.31}$$

The first term proportional to $1/(1-G)$ already shows an increase of the ion's energy for low gains. Moreover, a singularity at $G = 1$ yields a diverging energy in the theory, thus forbidding a steady state for all gains under this feedback condition. This phenomenon is also predicted by the quantum-mechanical approach. The damping rate is modified,

$\Gamma_{FB} = \Gamma(1 - G)$, which leads to a decrease in the interaction (cooling) rate of the oscillator and the thermal bath of the laser field. $\Delta_{FB} = \Delta$ remains unchanged as in the case of $-\pi/2$.

Figure 6.6 demonstrates the experimental results. The inloop measurements show an excessive "heating" of the ion explained by the inverse effect of noise cancellation shown before. The outloop measurements show a reduction of the sideband width as a function of the gain, while the area under the sideband is increasing. No frequency shift is observed.

Feedback with phase (π) and (0)

For a feedback with phase π one finds $X_\varphi \propto a_m + a_m^\dagger$. Thus a feedback force proportional to the position of the ion $\widetilde{z}_m \equiv a_m + a_m^\dagger$ is applied. The q.m. derivation yields (cf. Eq. (6.27))

$$\frac{\langle n_{phn}\rangle_{ss}^{\pi}}{n_{phn,i}} = 1 + \frac{1}{8}\,\frac{\tilde{\gamma} G_{qm}^2}{n_{phn,i}}[1 + 4\eta^2\tilde{\gamma}(2n_{phn,i} + 1)], \tag{6.32}$$

whereas the semiclassical prediction is

$$\frac{E_{\varphi=\pi}(G)}{E_0\ (G=0)} = 1 + \frac{G^2}{A}\ . \tag{6.33}$$

Both theoretical approaches show a quadratical dependence of the ion's energy as a function of the gain, though the semiclassical derivation just has one proportionality factor. The feedback parameters can be evaluated with the help of Eq.(6.18). The damping rate and the detuning under such conditions read

$$\begin{aligned} \Gamma_{FB} &= \Gamma \\ \Delta_{FB} &= \Delta\ + \frac{\Gamma G}{2}. \end{aligned} \tag{6.34}$$

Thus, the damping rate remains unchanged, but Δ_{FB} is increased which describes a shift of the oscillation frequency, as expected. Figure 6.7 shows the sideband measured outside the feedback loop. The width of the sideband (Γ) is $\Gamma_{noFB}/2\pi = 510(20)$Hz and $\Gamma_{G=1.3}/2\pi = 495(20)$Hz, thus describing an almost constant damping rate. Moreover, Fig.6.7 is already indicating a slight frequency shift on the order of $\delta f = 2$kHz under feedback operation. Figure 6.8 shows the frequency shift as a function of the electronic gain obtained for a series of five datasets. The errorbars indicate statistical deviations.

The case of a feedback with phase (0) is comparable to the case of phase (π). While the damping rate Γ remains unchanged, a frequency shift can be measured as well, i.e. $\Delta_{FB} = \Delta\ - \frac{\Gamma G}{2}$. Thus, the results of such a feedback induces a negative frequency shift.

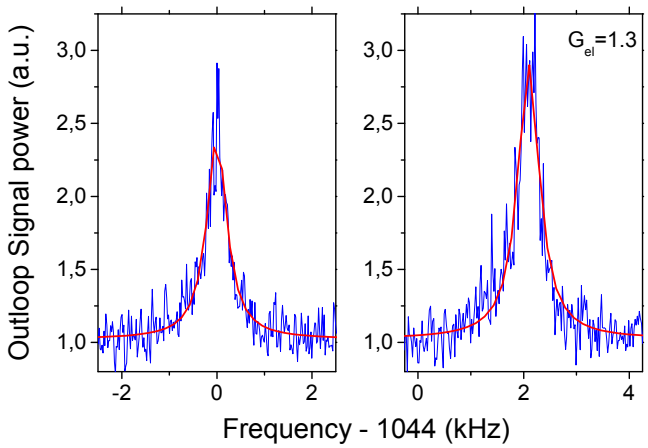

Figure 6.7: The X-sideband under a feedback operation with phase π measured outside the feedback loop. The sideband Γ remains unchanged, however a frequency shift of 2 kHz is measured (see also Fig. 6.8).

Calibration of the feedback gain

The amplitude of feedback applied to the ion is determined by the gain parameter. Experimentally, the purely electronic gain G_{el} - as being proportional to the overall, real gain - is used. In the presented analysis, G is introduced as the gain for the semiclassical model, G_{qm} ($G'_{qm} = G_{qm}/\eta$) for the quantum-mechanical. In the following, we will discuss, how these parameters relate.

We assume $G = a \cdot G_{el}$, where a is a (constant) conversion factor. Equation (6.29) describes the increase of the damping rate as a function of the gain under a feedback operation with phase $(-\pi/2)$. Rearranging this expression leads to

$$\frac{\Gamma_{FB}(G_{el})}{\Gamma_{noFB}} = a \cdot G_{el} - 1. \tag{6.35}$$

Measuring the increase of the damping rate Γ_{FB} as a function of the electronic gain (see Fig.6.9) yields a conversion factor of $a = 0.13(2)$ between the electronic gain G_{el} and the realistic gain G used for the semiclassical model.

On the other hand, a derivation in Ref. [76] results in

$$\frac{\Gamma_{FB}(G)}{\Gamma_{noFB}} = \frac{2\ \varepsilon n_{phn}}{1+\alpha} \cdot \frac{G_{qm}}{\eta} - 1, \tag{6.36}$$

where $\varepsilon = 0.006$ is the fraction of the solid angle collected (including the detector quantum efficiency), $\eta = 0.07$ the Lamb-Dicke parameter and $\alpha = 2/5$ the dipole parameter. Together with feedback with phase (π) comes a frequency shift, δf, expressed

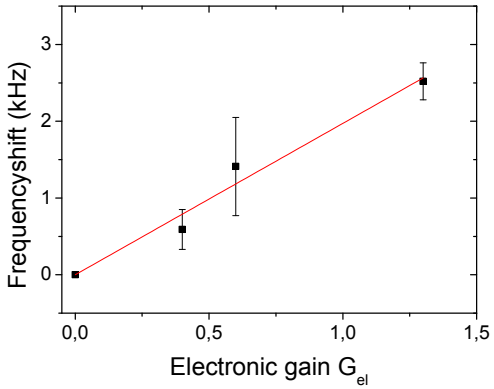

Figure 6.8: Frequency-shift of outloop spectra as a function of the electronic gain under π-phase feedback operation. A shift of 2kHz per electronic gain-unit is measured.

in Ref. [76]

$$\delta f \cdot G_{el} = \frac{\gamma\eta}{2} \cdot \frac{G_{qm}}{\eta}. \tag{6.37}$$

The parameter $\gamma \approx 40$ kHz is defined in Eq. (6.2). A frequency shift of 2 kHz yields $\frac{G_{qm}}{\eta} \approx 1.3 G_{el}$, inserting this into Eq. (6.36) results in $G_{qm} \approx 0.19 \cdot G_{el}$. We then conclude, that $G \sim G_{qm}$ and that the overall gain experienced by the ion is about one order of magnitude smaller than the pure electronic gain.

6.3.5 Motional energy and comparison of the models

In this section both theories, the semiclassical and the quantum-mechanical, are confronted with data measured in feedback experiments with different phases.

The mean phonon number of the ion oscillator is $n_{phn} \approx 17$ and is thus in a regime, where both theories are valid. Thereby, the Lamb-Dicke limit sets an upper limit for the application of the quantum-mechanical theory. Both theories in combination provide full understanding of such an experiment at the boundary of classical and quantum-mechanical physics. Semi-classical physics delivers an intuitive picture, but at the cost of loosing track of individual experimental parameters. In our case the parameter A ($\propto$ SNR) determines the experimental environment, but is a fitting parameter. On the other hand, the quantum-mechanical theory gives a quantitative understanding of the experiment and provides access to all kind of experimental parameters, e.g. the fraction of the solid angle collected by the observation lenses or the mean phonon number n_{phn} at the Doppler cooling limit. The latter allows one to calibrate the ion's vibrational energy in absolute numbers.

Figure 6.10 shows the vibrational energy of the ion oscillator as a function of the electronic feedback gain for three different feedback phases ($-\pi/2$ (a), π (b), $\pi/2$ (c)).

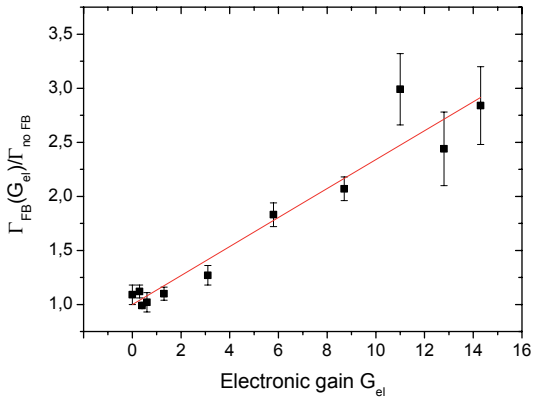

Figure 6.9: The linewidth of outloop spectra as a function of the electronic gain, a measurement supporting Eq. (6.29). A conversion factor between electronic and real gain is determined: $G = 0.13 * G_{el}$.

The vibrational energy is normalized to the case without feedback, i.e. $G_{el} = 0$. The figures show measured data together with the semiclassical model (Eqs. (6.28), (6.31) and (6.33)) and the quantum-mechanical prediction (Eqs. (6.27), (6.32)).

Firstly for feedback damping (feedback phase of $-\pi/2$, Fig.6.10(a)) we measure a cooling of the ion below the Doppler limit by ~ 30 %. We observe an agreement between the measurement and both theories for small gains G_{el}. The data support both theories within the measurement error bars. The semiclassical model shows a more pronounced cooling at higher gain (0.63 @ $G_{el} = 1.6$) compared to the quantum-mechanical case (0.68 @ $G_{el} = 1.3$). This can be explained by the state-destructive nature of a quantum measurement, which is not considered in the semiclassical approach. For higher gain, the semiclassical model shows a stronger heating of the ion by the measurement induced noise. From the quantum-mechanical model we can deduce a mean photon occupation number for the laser cooled Ba^+ ion of $n_{phn} \approx 17$.

Secondly, Fig.6.10(b) shows feedback leading to heating of the ion motion. Once again, we observe agreement (within the error bars) between the measurement and both theories for a small gain. Both theories show a quadratic increase of the ions energy as the feedback gain is increased. A better agreement between the measurements and the quantum-mechanical theory can be found by "applying" a feedback signal with a detuning δ of $\delta \approx \Gamma$ in the quantum-mechanical model. This is shown in the inset of Fig.6.10(b), where the vertical line describes a singularity introduced by the frequency detuning. The quantum-mechanical model looses its validity at this point, the semiclassical still grows quadratically with G_{el}. Another remarkable feature is shown in this plot. The data-points at $G_{el} > 1.3$ clearly show a saturation of the ion energy for high gains. This effect can be explained by a competition of two effects, the driving feedback field and the confining trap potential.

In the case of a feedback with phase $\pi/2$ shown in Fig.6.10(c) we can observe a similar behavior. The measurement clearly shows , that the energy of the ion is not increased, even for higher gains. On the contrary, both theories suggest a rapid increase of the ion's energy for small gains and show singularities at $G_{el} = 0.6$ ($G_{el} = 1$) in the quantum-mechanical (semiclassical) description.

To summarize, we find good agreement between measurements and both models for feedback with phase $-\pi/2$ and phase π. In addition, experimental results show a saturation effect setting limits for a "self excitation" of the ion oscillator, which is not included in either theory.

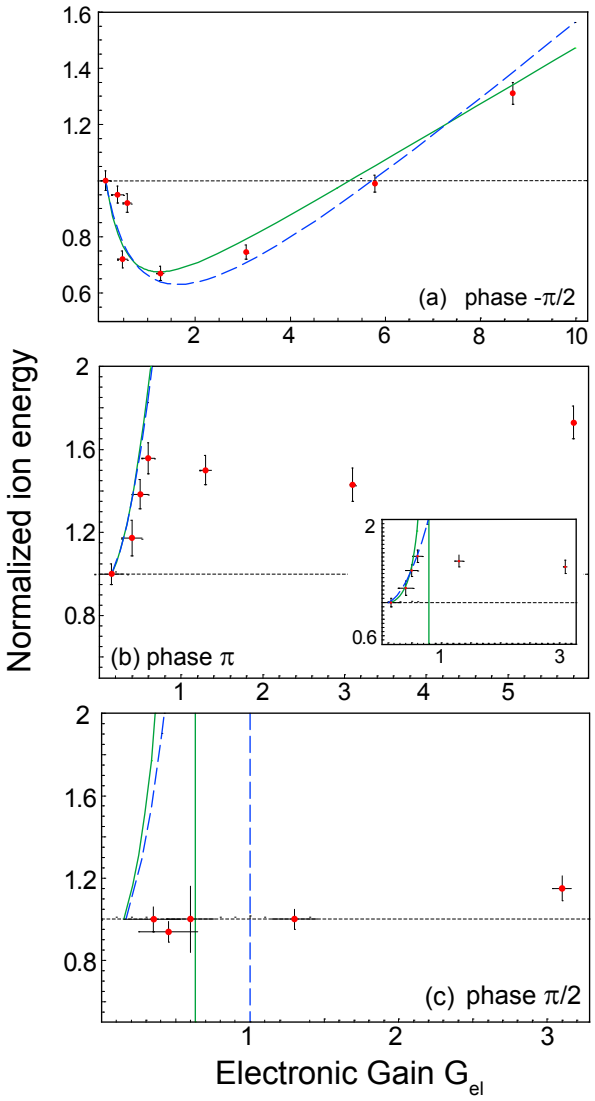

Figure 6.10: The (normalized) energy of the ion as a function of the feedback gain for different phases, $-\pi/2$ (a), π (b) and $\pi/2$ (c). The green, full line describes the quantum-mechanical model, the blue, coarse dashed line shows the result of the semiclassical theory, the fine dashed line shows the line of unity. Only the phase of $-\pi/2$ is leading to feedback damping. The parameters used for the quantum-mechanical model are identical for all three plots: $\eta = 0.06$, $n_{phn} = 17$, $\varepsilon = 0.06, \delta = 0$ (Γ in the inset of (b)). The parameters for the semiclassical model: $A = 9$ in (a) and $A = 0.6$ in (b) and (c).

7 Time-resolved measurements of motional sidebands

This chapter presents time-resolved measurement of the motion of a single Barium-ion making use of second-order time correlations of fluorescence photons. By beating the fluorescence with itself in a "self-homodyne" configuration, radial sidebands are visible in the time-domain. The second-order correlation function turns out to be a very powerful tool: At the nanosecond time-scale, the correlations describe the internal structure of the ion wave-function and the anti-bunching in the resonance fluorescence is quantitatively reproduced. On the other hand, for microseconds time-scale, the correlations show the motional degrees of freedom. Thus, (radial) motional modes and their relative coherence are measured with a time-resolution down to 1 ns thus proving the stability of the ion trap.

From Chapter 3, in particular Eq. (3.52), it is apparent, that the photocurrent measured in the "self-homodyne" configuration contains information about the motion of the ion. Observations shown in Fig. 5.7 or in Chapter 6 evidently demonstrate this in the frequency domain where motional sidebands are clearly visible. Indeed, a time-resolved measurement of the same photocurrent reveals motional degrees of freedom too.

7.1 The experimental setup

The experimental setup is shown in Fig. 7.1. The Barium ion is laser-cooled by the two lasers at 493 nm (green) and 650 nm (red) wavelength. The lasers have frequencies close to resonances and intensities below the saturation thresholds. The ion-trap operating with typical parameters confines the Barium ion to oscillate at trap frequencies of about $\omega_x/2\pi \approx 1\,\mathrm{MHz}$, $\omega_y/2\pi \approx 1.2\,\mathrm{MHz}$ and $\omega_z/2\pi \approx 2$ MHz in the radial (x and y) and axial (z) modes of motion. The trap coordinate system is denoted with (x, y, z) and the lab coordinate system with (x', y', z') as before.

In this experiment, only the green part of the resonance fluorescence is studied. The distant mirror situated $L \approx 25$ cm away from the ion retro-reflects the fluorescence collected through the Halo-lens L2. Overlapping the ion and its mirror image creates the self-interference as described in Chapter 3. Scanning the piezo-mechanical mounts for the mirror scans this interference with a visibility as high as 72 % for very weak laser excitation [28]. The analysis presented in the following was obtained for slightly

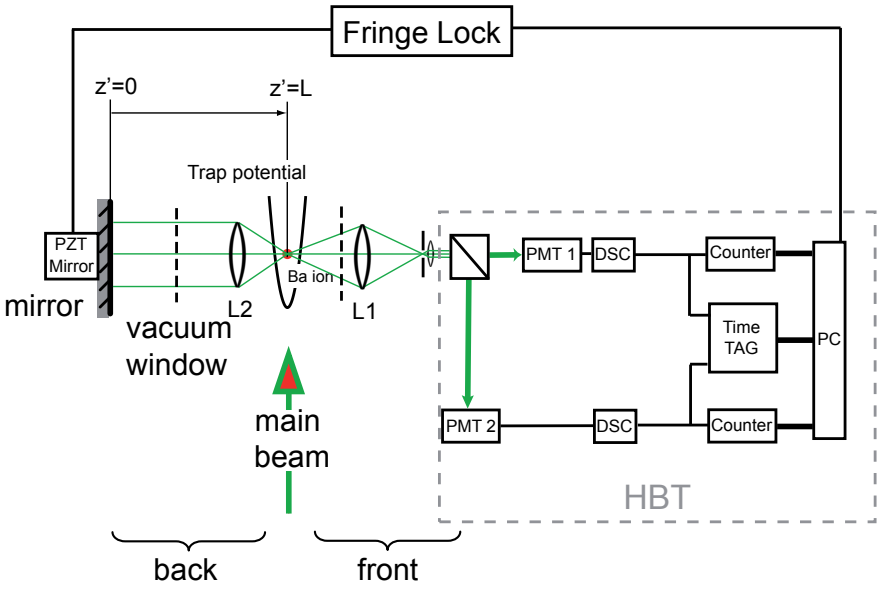

Figure 7.1: Sketch of the experimental setup: L1...macroscope, L2...Halo-lens inside the vacuum, PZT...piezo translation stage, PMT...photomultiplier, DSC...discriminator, Time TAG...correlator, HBT...Hanbury-Brown and Twiss setup.

higher excitation intensities so that the contrast reduces to about 50 %. Using a mean photo-current as set-point, L is fixed in these experiments such that the ion is located at the slope of its reflected fluorescence standing wave: The mirror position is controlled with a precision of 10 nm by the mean of a servo loop acting on a piezo-mechanical positioning (fringe lock). The second-order correlation function is measured in a Hanbury-Brown and Twiss configuration (HBT) including a 50/50 beam splitter and two photo-multipliers. The photons detected by the two photomultipliers are time tagged according to their arrival time in an auto correlator (TAG in Fig. 7.1). Second-order time correlations among these events are then calculated. Unlike methods where merely time intervals between *successively* detected photons are correlated, the time tag method has no statistical influence on the count rate (pile-up effect) and needs no systematic corrections [97]. Finally, detected correlations are normalized so that $g^{(2)}_{z'}(\infty) \to 1$.

In a corpuscular picture, green fluorescence photons can take two paths along the mirror-detector axis before reaching the photo-detectors: either they are emitted directly towards the detectors or they are emitted towards the mirror and then detected after reflection. The distance between the ion and the mirror sets the time delay, $\tau = 2 \times L/c \approx 1.5$ ns, between these paths.

7.2 The Model

Now the second-order time correlations of green fluorescence photons should be investigated with a particular focus on the secular motion of the ion. The mirror is placed at $z'=0$, the center of the trap is at $z'=L$. The position operator of the ion relative to the center of the trap is denoted by $\widehat{z}_m \propto (a_m + a_m^\dagger)$; a_m and $a_m^\dagger$ are bosonic operators associated to the motion of the ion. The trap axis is tilted with respect to z' by approximately 45°, z_m in fact corresponds to the projection of x, y or z along z'. Along the z' axis, the field operator for green photons then reads (cf. Eq. (3.47))

$$E_{z'}(t) = \sqrt{\epsilon\Gamma_g}\sin(k_g(L+\widehat{z}_m))\sigma^-(t), \tag{7.1}$$

where Γ_g is the $P_{1/2}$-$S_{1/2}$ spontaneous emission rate and k_g the corresponding photon $k-$vector at 493 nm. In Eq. (7.1), $\sigma^-=|S_{1/2}\rangle\langle P_{1/2}|$ is the lowering Pauli operator, associated to the creation of a photon. Moreover, when writing Eq. (7.1) it is implicitly assumed that this experiment is carried out in the Markovian limit [1]. The time delay induced by the mirror, T, is in fact much smaller than the dynamics of the system, namely the spontaneous emission lifetime of the $P_{1/2}$ state, $\tau \ll 1/\Gamma_g$, and the timescales associated with laser interactions, $\tau \ll 1/\Omega$, $1/|\Delta_L|$, Ω and Δ_L being the laser excitation and detuning respectively. Along the z'–axis, the second-order correlation function is defined by

$$g^{(2)}_{z'}(t,t+\tau) \propto \langle E^\dagger_{z'}(t)E^\dagger_{z'}(t+\tau)E_{z'}(t+\tau)E_{z'}(t)\rangle. \tag{7.2}$$

In the following experiments, at the Doppler limit the mean phonon number for the motional states of the ion is $n \approx 17$, resulting in an effective $\eta\sqrt{n} \approx 0.3$. $\eta = 2\pi a_0/\lambda \sim 0.07$ is the Lamb-Dicke parameter, a_0 denotes the r.m.s. size of the trap ground state. In such a regime, the motional sidebands have intensities reduced by the effective Lamb-Dicke parameter, relative to the elastic component of the fluorescence. It is thus satisfied to expand exponentials (cf. Chapter 3), e.g.

$$e^{ik_g\widehat{z}_m} = e^{i\eta(\widehat{a}_m+\widehat{a}^\dagger_m)} \equiv 1 + i\eta(a_m + a_m^\dagger) + o(\eta^2). \tag{7.3}$$

For the ion placed at the slope of the mirror standing wave, *i.e.* $k_gL=\pi/4$, the oscillating term in Eq. 7.1 is expanded into

$$\begin{aligned}
\sin(k_g(L+\widehat{z}_m)) &= \sin(k_gL + \eta(\widehat{a}_m + \widehat{a}^\dagger_m)) \\
&= \sin(k_gL)\cos(\eta(\widehat{a}_m + \widehat{a}^\dagger_m)) + \cos(k_gL)\sin(\eta(\widehat{a}_m + \widehat{a}^\dagger_m)) \\
&= \frac{1}{\sqrt{2}}[\cos(\eta(\widehat{a}_m + \widehat{a}^\dagger_m)) + \sin(\eta(\widehat{a}_m + \widehat{a}^\dagger_m))] \\
&= \frac{1}{\sqrt{2}}[1 + \eta(\widehat{a}_m + \widehat{a}^\dagger_m) - \frac{\eta^2}{2}(\widehat{a}_m + \widehat{a}^\dagger_m)^2 + ...]
\end{aligned} \tag{7.4}$$

[1] The non-Markovian interaction between the ion and its reflected fluorescence is studied in the next chapter

The field operator for green photons can be rewritten,

$$E_{z'}(t) = \sqrt{\epsilon\Gamma_g}\widehat{c}_m\sigma^-(t), \tag{7.5}$$

with

$$\widehat{c}_m = \frac{1}{\sqrt{2}}\left(1 + \eta(\widehat{a}_m + \widehat{a}_m^\dagger) - \frac{\eta^2}{2}(\widehat{a}_m + \widehat{a}_m^\dagger)^2\right). \tag{7.6}$$

From equations (7.1-7.6) the deduced normalized second-order correlation function at lowest order in η is

$$g_z^{(2)}(t, t+\tau) \cong (1 + 2\eta\langle a_m + a_m^\dagger\rangle)g^{(2)}(t, t+\tau)\ , \tag{7.7}$$

where $g^{(2)}(t, t+\tau)$ denotes the usual normalized second order correlation function for a single trapped ion. In order to accurately reproduce the exact shape of the measured correlations, $\gamma^{(2)}$ is evaluated considering the 8 relevant electronic levels for the ion internal states [63]. The second term, proportional to $\langle a_m + a_m^\dagger\rangle$, shows that the $g^{(2)}$–function is modulated by the motion of the ion. This modulation arises from the self homodyne configuration of the experimental setup. Finally, for continuous laser excitation, Eq. (7.7) is evaluated at steady state, i.e. for t $\rightarrow \infty$, such that $g_z^{(2)}(t, t+\tau) \rightarrow g_z^{(2)}(\tau)$.

7.3 Results

In Fig. 7.2 the measured second-order photon correlation function for a ion-mirror distance of $L \approx 25\,\text{cm}$ is presented. It is obtained after subtracting the contributions from non-interfering ion and mirror image. In the following only the coherent part of the interaction between directly emitted and reflected fluorescence photons, i.e. the signal described by Eq. (7.7) (see Chapter 8 for details) is considered. Apart from the usual photon anti-bunching at $\tau = 0$, for time intervals τ greater than $1/(2\pi\Gamma_g)$, a modulation induced by the motion of the ion is resolved in the $g^{(2)}$–function , as previously discussed. In the experimental setup, every secular modes of motion, namely one axial and two radial ones, can contribute. Indeed, these have non-vanishing projections along the $z'-$ axis. In addition, the micro-motion which appears due to the trap drive at 20 MHz, can also be projected along z'. However, the amplitude of the micro-motion is reduced to operate in the most stable trap region, the observed modulation in the $g^{(2)}$–function is then only due to the secular motion of the ion.

For this geometry, laser-cooling is more efficient along the axial direction z than along the radial ones. Therefore, the amplitude of the axial motion is reduced compared to the one of the radial modes. The modulation of the correlation function is then mainly governed by the sum of projections of the radial modes. As shown in Fig. 7.2, slow and fast frequency components are resolved. The slow component reflects the beat-frequency between the two radial modes of motion, separated by ≈164 kHz for our trap.

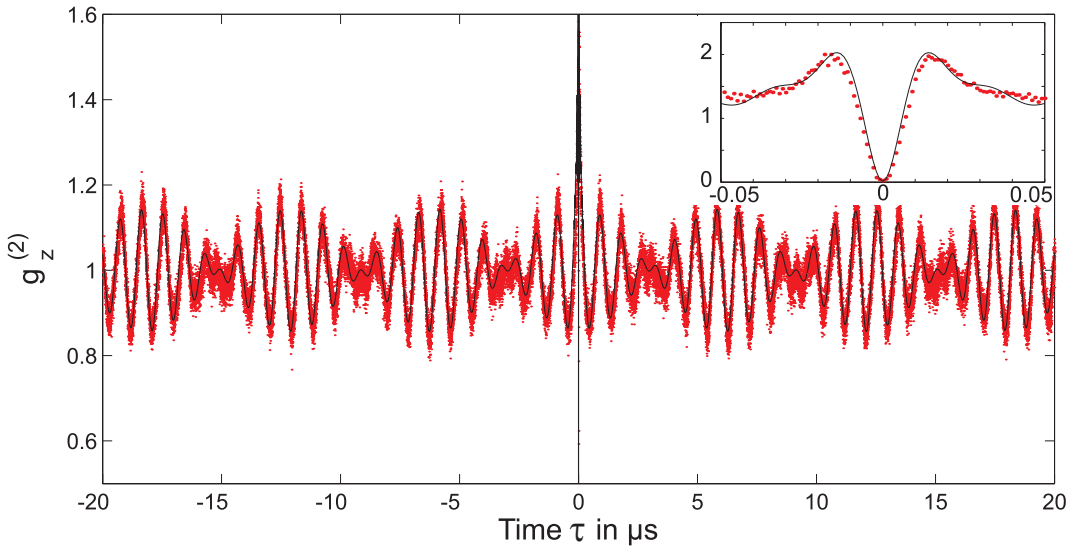

Figure 7.2: Second-order time correlation function for time intervals τ up to 20 μs: The experimental data are shown as (red) dots, the theoretical predictions for the same parameters as a black, solid line. The modulation of the $g^{(2)}$–function reveals the two frequencies of the motional sidebands along the radial directions. *Inset:* Photon-antibunching for short times τ up to 50 ns. Experimental data are displayed with a 1 ns time resolution.

A Fourier transform of the correlation function shown in Fig. 7.3 thereby exhibits the exact frequencies, $\omega_x/2\pi = 1.034(1)$ MHz along the x axis and $\omega_y/2\pi = 1.198(1)$ MHz along the y axis. Note that the vanishing contrast of the modulation (for $\tau \approx 500$ μs) limits the accuracy of the central frequency measurement.

A de-phasing between the radial modes of motion of the ion is observed. The amplitude of the beat signal presented in Fig. 7.2 diminishes exponentially with a time constant equals to 1.64 ms. This reveals that the phase of each radial mode diffuses due to laser-cooling. Such observation is confirmed by independent measurements of radial sidebands [30]. On the other hand, the central frequencies of the two radial modes do not drift within the experimental precision. More precisely, up to $\tau \approx 500\,\mu$s, no difference between the frequencies used in the model and the ones of the radial modes deduced from the correlation function is resolved: Figure 7.3 demonstrates good agreement between the data and the theoretical predictions for $\tau \approx 160\,\mu$s. The analysis in fact yields an upper limit for the frequency drift of the trap potential, about 2 kHz per 30 min (the overall measurement time). Note that measurements performed with the same trap show drifts of the radial frequencies on the order of 600 Hz per 30 minutes [30].

In summary, this measurement shows that second-order correlation functions ob-

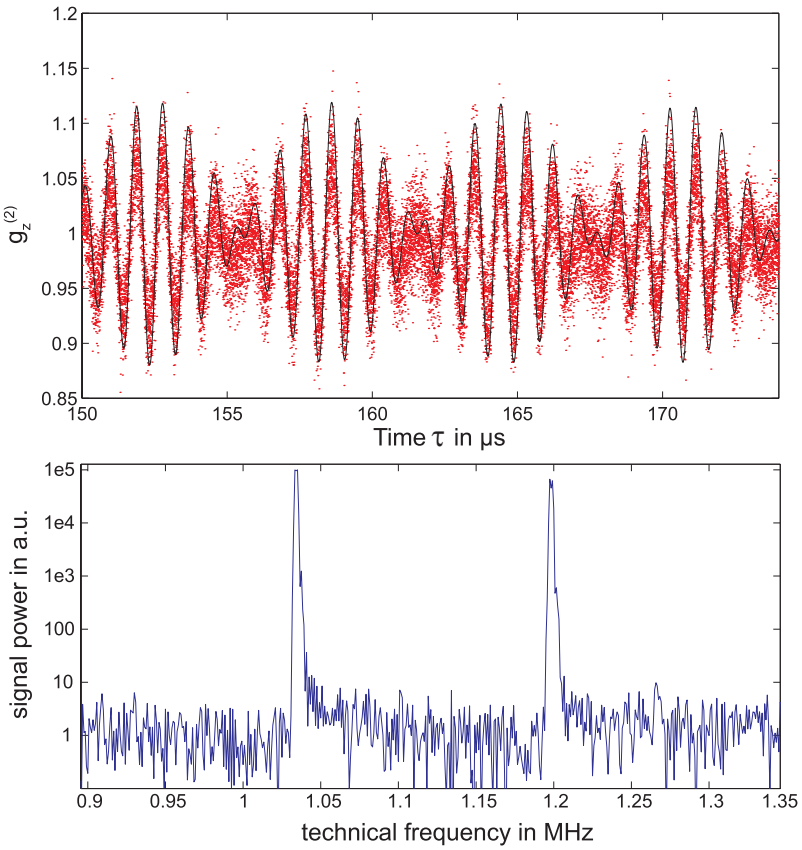

Figure 7.3: *Top:* The second-order time correlation function for $\tau \approx 160$ μs. The data (red points) and the theoretical predictions still coincide thus revealing the trap stability (Experimental data are displayed with a 1 ns time resolution) *Bottom:* Spectrum of the correlation function which shows the two radial sidebands. Other frequency components are suppressed by at least three orders of magnitude.

tained in a homodyne configuration can reveal both internal and external dynamics of a single trapped-ion. At short time intervals between photon emissions (nanoseconds), the ion *internal* dynamics governs the correlation function while for longer time intervals (microseconds), the *motion* of the ion modulates the correlation function. In the latter case, the ion probes its surrounding potential such that the $g^{(2)}$–function can be used to characterize the stability of the trap potential.

8 Photon correlations vs. interference of single-atom fluorescence in a half cavity

This chapter describes an experiment to investigate photon correlations for a single laser-excited ion trapped in front of a mirror. The measurements were performed in the old trap. Unlike the measurements presented in chapter 7 the ion-mirror distance is on the order of one meter. This "half-cavity" system is thus studied in a non-Markovian regime, i.e. a regime where the time delay picked up during a photon round-trip is *not* negligible compared to the relevant time scales present in this system, e.g. the lifetime of the excited state. Thus, significant memory effects appear. Varying the relative distance between the ion and the mirror on a nm scale, i.e. positioning the ion in the node or anti-node of the standing interference-wave, photon correlation statistics can be tuned smoothly from an antibunching minimum to a bunching-like maximum. This analysis reveals the field establishment in a half-cavity interferometer and thus gives also insight into cavity-QED physics. Moreover, the measurements confirm the predictions made in a theoretical paper published by Uwe Dorner and Peter Zoller in [34]. The experiments presented here are published in [98].

8.1 The experimental setup

The schematic experimental set-up is shown in Fig. 8.1. The ion is continuously driven and cooled by the two narrow-band lasers at 493 nm (green) and 650 nm (red) exciting the $S_{1/2}$–$P_{1/2}$ and $P_{1/2}$–$D_{3/2}$ transitions, respectively. A fraction ϵ of the green fluorescence photons is reflected by the distant mirror placed at $z = L$ and focussed back onto the ion. The $g^{(2)}$ correlation function of the 493 nm light is analyzed in the observation channel opposite to the mirror in a Hanbury-Brown and Twiss setup (see Fig. 3.5). The photon-pulses are discriminated and correlated using the time-tag method (TTSPC), according to Fig. 4.6, with a specified temporal resolution is 4 ps. For the measurements the time intervals between pairs of detected photons is evaluated using a 500 ps time bin width, and then divide the data by the total integration time (several hours) after background subtraction. A slow electronic servo loop (fringe lock) stabilizes the average photocurrent and thereby permits control of the distance L between the ion and the mirror with better than 10 nm precision.

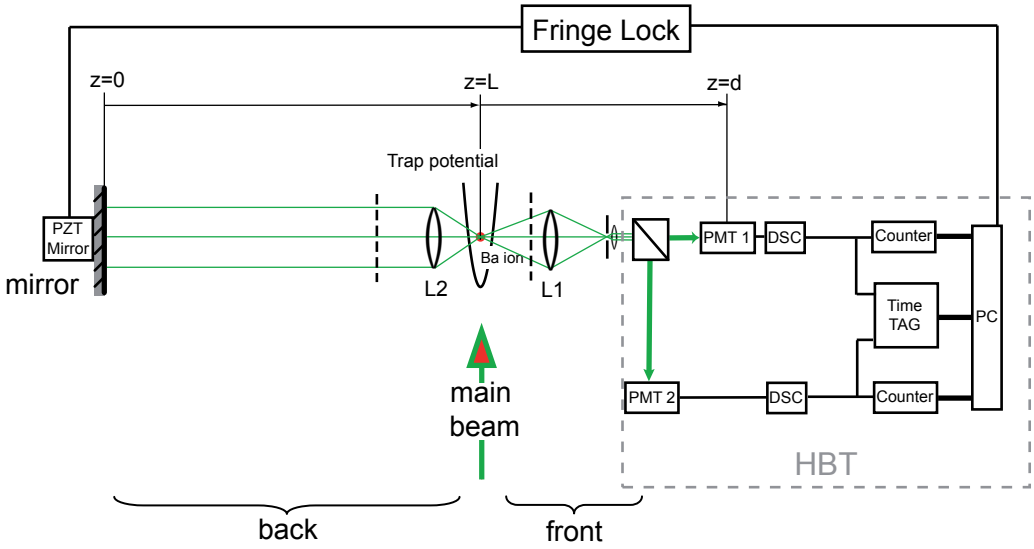

Figure 8.1: Experimental setup: Piezo-actuators (PZT), photomultipliers (PMT 1 and 2), TTSPC: Time Tagged Single Photon Counting.

The measured light has two components, the direct and the reflected part of the radiation scattered by the ion, with a time delay T between them. For very low laser intensities, when all scattering is elastic, the resulting interference of these components is observed with up to 72% visibility [28] into that mode. In the measurements presented here slightly higher laser excitation parameters are used, whereby the contrast reduces to around 50%. The interference signal can be viewed as a consequence of the standing wave which forms in the mirror mode and which leads to inhibited and enhanced detection of resonance fluorescence photons [28]. The signal varies with the ion-mirror distance L as $\sin^2(k_g L)$, where k_g is the momentum of photons emitted at 493 nm, according to Eq. (3.52). A fringe minimum corresponds to the ion being located at a node of the standing wave, i.e. $k_g L = n\pi$ (n being an integer); the maximum corresponds to $k_g L = (n + \frac{1}{2})\pi$, i.e. to the ion being at an antinode (cf. Fig. 3.11).

Note that on average there are less than 10^{-3} photons in the mode volume between the ion and the mirror. Photodetection reveals interference which is created by partial waves corresponding to the same individual photon. In addition, each detection event implies state projection of the atom and thereby exhibits its dynamical information.

8.2 The model

Now the second order correlation for arrival times of green photons should be investigated. Theoretical studies of such a system can be found in Ref. [34]. Here, the main theoretical results, restricting the treatment to the $S_{1/2}$ and $P_{1/2}$ levels, should be

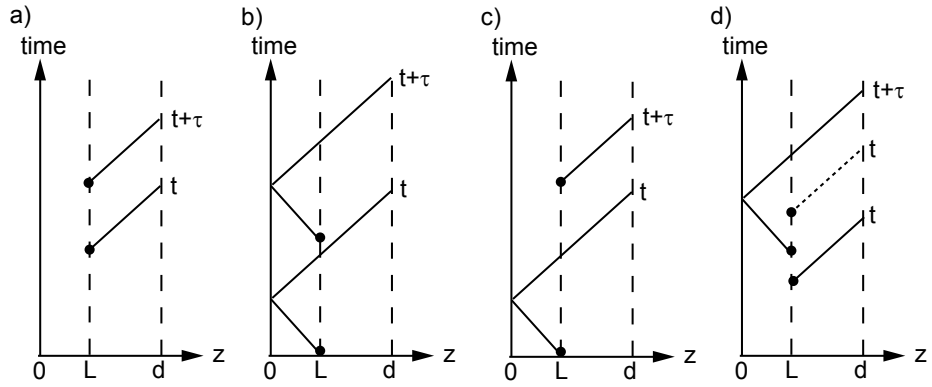

Figure 8.2: Space-time diagram for the four different contributions in Eq.(8.2). Reproduced from [34].

recalled. As shown in Fig. 8.1, the mirror-ion-detector axis is labelled as z, the mirror is positioned at $z = 0$ and the trap center at $z = L$[1]. The "round-trip" time a photon needs to cover the ion-mirror-ion distance is denoted with T, the time difference between two correlated photons is denoted with τ. Neglecting the motion of the ion in the trap, the field operator for green photons in the mirror mode (index m) at $z = L$ reads

$$E_m(L,t) = \frac{\epsilon\Gamma_g}{2}\frac{i\hbar}{d}e^{-i\omega_L t}[\sigma^-(t)\theta(t) - e^{i\omega_L T}\sigma^-(t-T)\theta(t-T)] \ , \tag{8.1}$$

where $\theta(t)$ is a step function centered at $t = 0$, Γ_g is the free-space decay rate of the $P_{1/2}$ to $S_{1/2}$ transition, and d its dipole oscillator strength. σ^- denotes the lowering operator from $|P_{1/2}\rangle$ to $|S_{1/2}\rangle$ and ω_L the laser frequency. In Eq.(8.1) the Heisenberg (interaction) picture is used, such that operators are presented in a rotating frame $\sigma^-(t) \rightarrow \sigma^-(t)e^{-i\omega_L t}$. Including proper commutation rules between input and output states of the field, the second order time correlation function in the mirror mode, $g_m^{(2)}(t,t+\tau) = \langle E_m^\dagger(L,t)E_m^\dagger(L,t+\tau)E_m(L,t+\tau)E_m(L,t)\rangle$, reads

$$\begin{aligned} g_m^{(2)}(t,t+\tau) \propto \| & \sigma^-(t+\tau)\sigma^-(t) \\ & + e^{2i\omega_L T}\sigma^-(t+\tau-T)\sigma^-(t-T) \\ & - \mathcal{T}_{\leftarrow} e^{i\omega_L T}\sigma^-(t+\tau-T)\sigma^-(t) \\ & - e^{i\omega_L T}\sigma^-(t+\tau)\sigma^-(t-T)|i\rangle\|^2 \ , \end{aligned} \tag{8.2}$$

where $|i\rangle$ denotes the initial state of the system, i.e. the ion in the ground state $|S_{1/2}\rangle$ and the mirror mode in the vacuum state. The different contributions in Eq. (8.2) are visualized in Fig. 8.2 and interpreted as follows: the first term corresponds to the detection of two photons directly emitted towards the detectors (case a)) placed at

[1]For simplicity the lab coordinate system is here denoted with x, y, z.

$z = d$ and separated by a time interval τ; in the second term (case b)), these photons are both reflected by the mirror situated at $z = 0$ and therefore both delayed by T before detection. The two last contributions describe possible detection of either first a directly emitted photon and then a second one after its reflection on the mirror (third term, case d)), or vice-versa (fourth term, case c)). In the former case, for $\tau < T$ causality is ensured by $\mathcal{T}_{\leftarrow}$ which enforces the time ordering of the two operators on its right hand side. These must be arranged chronologically from right to left and have to be commuted if they are not. Consequently, in Eq.(8.2) different contributions interfere. The first two terms induce anti-bunching around $\tau = 0$ while the two others may counteract this usual behavior. As we show below, the weight of each component strongly depends on the actual position of the ion, i.e. whether it is located at a node or at an anti-node of the mirror mode. Finally, from Eq.(8.2) one obtains in the steady-state limit ($t \to \infty$)

$$g_m^{(2)}(\tau) \propto \; |2b_{\mathrm{P}_{1/2}}(\tau)\cos(2k_gL) - b_{\mathrm{P}_{1/2}}(|\tau - T|) - b_{\mathrm{P}_{1/2}}(\tau + T)|^2 \tag{8.3}$$

where $b_{\mathrm{P}_{1/2}}$ denotes the occupation amplitude of the $\mathrm{P}_{1/2}$ level. In principle, it should be evaluated including the mirror induced modifications of decay rate and energy value of the $\mathrm{P}_{1/2}$ state [28]- [30]. Nevertheless, the mirror back-action can be neglected for the current analysis, with ϵ being on the order of 1.5%. Then $b_{\mathrm{P}_{1/2}}$ is deduced from the density matrix time evolution considering a single Ba^+ ion trapped in free space. Note that all 8 electronic sub-levels need to be accounted for in order to accurately reproduce the exact shape of the measured correlations [63]. Figure 8.3 shows a plot of Eq. (8.3) for a delay time $T = 1/\Gamma_g \sim 7\,\mathrm{ns}$ and for three different positions Node ($k_gL = 0$), Slope ($k_gL = \pi/4$) and Anti-node ($k_gL = \pi$).

8.3 Results

In the left panel of Fig. 8.4, the correlation function in absence of the mirror, $g_{nm}^{(2)}$, is presented. It is obtained using the set-up depicted in Fig. 8.1, but with the mirror blocked. The measurement exhibits the single-ion characteristic of anti-bunching at short time, with a null rate of coincidences, $g_{nm}^{(2)}(0) \simeq 0$. It is accurately reproduced by the simulations described in chapter 3 and do not require any fitting parameter, only experimental conditions such as laser powers and detunings [63].

The right panel of Fig. 8.4 shows the correlation function when the mirror is included, but without overlapping the reflected field with its source; ion and mirror image are then spatially distinct, and there is no interference. The signal, $g_{ni}^{(2)}(\tau)$, corresponds to three synchronous but non-interfering sources, shifted in time by $\pm T$ ("non-coherent addition"). The expected contributions to this signal are the moduli squares of the three terms in Eq. (8.3), without the cosine dependance, i.e. without interference, it reads

$$g_m^{(2)}(\tau) \propto \; 2|b_{\mathrm{P}_{1/2}}(\tau)|^2 + |b_{\mathrm{P}_{1/2}}(|\tau - T|)|^2 + |b_{\mathrm{P}_{1/2}}(\tau + T)|^2. \tag{8.4}$$

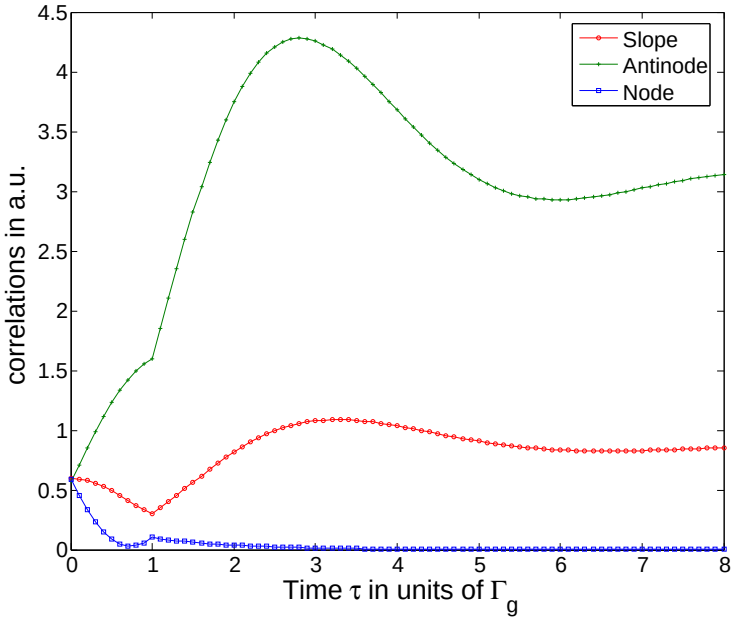

Figure 8.3: Calculated second order correlation function for a two level system for a delay time of T=7 ns. Details in the text.

As shown by the full line, their sum accurately reproduces the measurements. In the following this signal is used as a reference, as discussed below.

Figure 8.5 is presenting raw data of measured second order correlation functions, where both $g_m^{(2)}(\tau)$ and $g_{ni}^{(2)}(\tau)$ are contributing. Two different ion-mirror distances of $L \sim 65\,\text{cm}$ and $\sim 90\,\text{cm}$ are shown in the left and right panel. The corresponding delay-times are $T = 4.5\,\text{ns}$ and $T = 6\,\text{ns}$ respectively, comparable to the excited state lifetime of $1/\Gamma_g \approx 7\,\text{ns}$. For each distance three different situations are studied, the ion being at a Node position (blue, line and square), at the slope (red, line and circles) or at an Antinode position (green, line and circles) of the standing wave. Prominent features appear at $\tau \sim 0$, whose visibility is a function of the overall ion-mirror distance.

In the model leading to Eq. (8.3), experimental conditions are assumed to be ideal with 100% fringe contrast of the green interference. Experimentally a contrast of merely 50% is observed, such that Eq. (8.3) only accounts for half of the measured correlations, while the remaining part corresponds to $g_{ni}^{(2)}$. Therefore in all data sets for $g_m^{(2)}(\tau)$ shown below, the measured $g_{ni}^{(2)}(\tau)$ has already been subtracted from the raw histogram data. Limited interference contrast arises from inelastic scattering, imperfect mode-matching of direct and reflected light, and relative motion between ion and mirror.

Figure 8.6 presents the normalized second order correlation functions $g_m^{(2)}(\tau)$ for interfering ion and mirror image. As above, three relevant situations are studied: the ion close to a node ($k_g L = 0.03\pi$), on the slope ($k_g L = 0.28\pi$) and close to an antinode

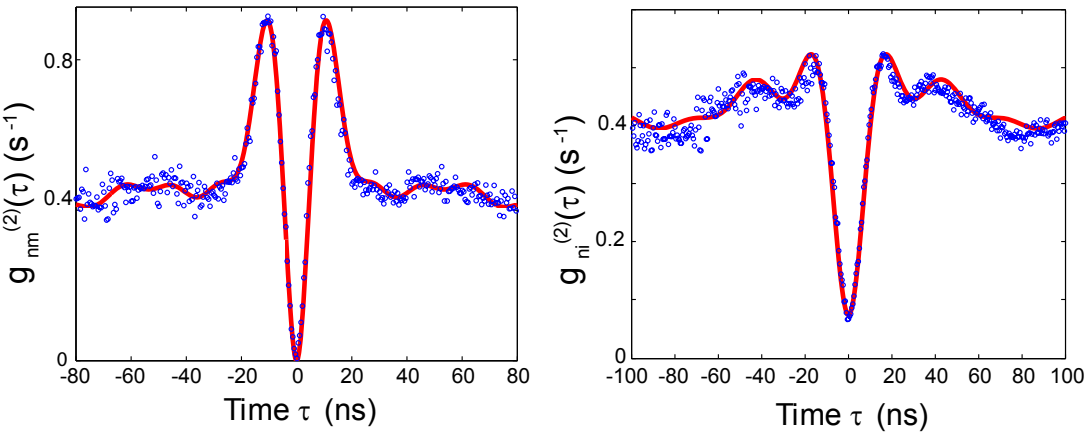

Figure 8.4: *Left*: Measured second order correlation function without mirror, $g^{(2)}_{nm}$ (circles) and its simulation calculated from 8-level Bloch equations (line). *Right*: Correlation function for non-interfering ion and mirror image, $g^{(2)}_{ni}$, for $T = 4.5$ ns. The line is the sum of four correlation functions as explained in the text.

($k_g L = 0.4\pi$) of the standing-wave mirror mode. The first notable feature is that always $g^{(2)}_m(0) > 0$. For the single ion trapped in front of a mirror, such coincidence can only appear when a directly emitted and reflected photon are simultaneously detected. This is possible in this experiment since the delay of a reflected photon is comparable to the time required to re-excite the ion to the $P_{1/2}$ state.

The second important feature is that all situations show the same coincidence rate $g^{(2)}_m(0)$, although the relative phase ($2k_g L$) between the coincident direct and reflected photon fields is different in the three situations. This demonstrates that at $\tau = 0$ interference can not be observed yet.

Another interesting feature appears in the long-time limit $\tau \gg T$: in Eq.(8.3) the time argument of $b_{P_{1/2}}$ reduces to τ and

$$g^{(2)}_m(\tau) \equiv \sin^4(k_g L)|b_{P_{1/2}}(\tau)|^2|b^{(ss)}_{P_{1/2}}|^2, \tag{8.5}$$

where $|b^{(ss)}_{P_{1/2}}|^2$ is the steady state population of the $P_{1/2}$ state. The second order correlation function thus factorizes into the product of the first order correlations at time t and $(t + \tau)$. For the anti-node position, $k_g L = \pi/2$, the interference is constructive and $g^{(2)}_m(\tau \gg T)$ is maximal. On the other hand, at the node position the fully established destructive interference suppresses the detection of photon pairs with long time intervals between them, thus creating a strong effective bunching around τ=0 despite the fact that only a single atom is investigated. Studying the long-time limit is in fact reminiscent of high finesse cavity QED.

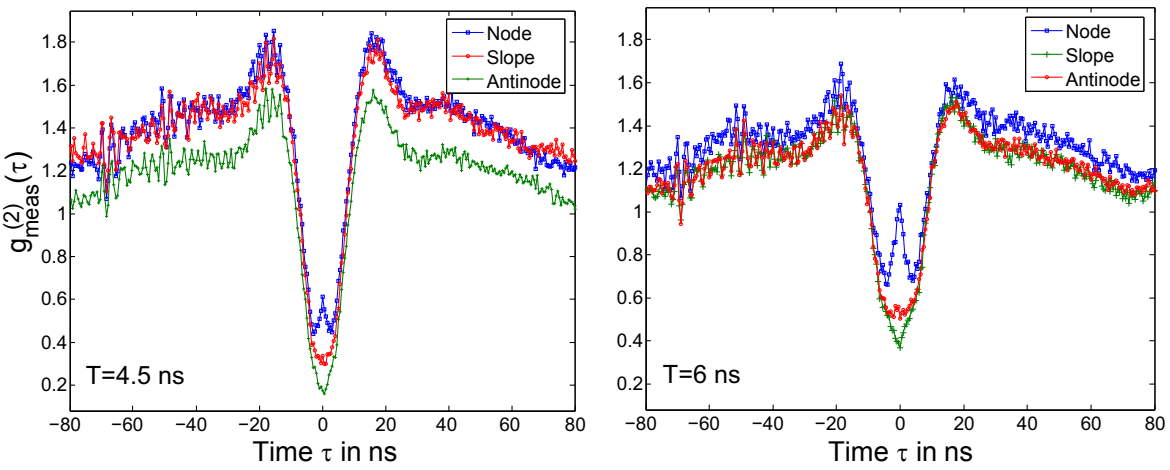

Figure 8.5: Measured second order correlation function for a delay time of T=4.5 ns (left) and T=6 ns (right).

Finally, the correlations for short time delay between photon detections, $0 < \tau \leq T$ are studied. In this regime memory effects are crucial, as one can see from Eq. (8.3), where excited-state amplitudes at different times are superimposed. The difference between the three positions originates mainly from the weight $\cos(2k_g L)$ of the first term in Eq. (8.3), which corresponds to the processes where both photons are emitted in the same direction. The two other terms, describing processes where they take opposite directions, do not depend on the mirror phase. As a result, a conspicuous kink in all the curves at $T \approx \tau$ is observed. This kink marks the onset of full interference, when no more which-way information is present.

To summarize, the second order time correlation function shows dramatically different results depending on the position of the ion, e.g. at a node or at an antinode of the reflected field standing wave. The detection of photon pairs separated by a large time interval is modulated by the interference experienced by each photon. Coincident two photon detections are insensitive to the exact position of the ion, because interference can not be established. Consequently, when the ion is placed at a node of its reflected fluorescence standing wave, a single photon detection is prohibited by first order interference while a joint two photon detection is allowed. This appears as a bunched profile in the correlation function which reveals the transient regime of the field establishment in the half cavity interferometer. The quasi-bunching effect can be increased with the ion-mirror distance.

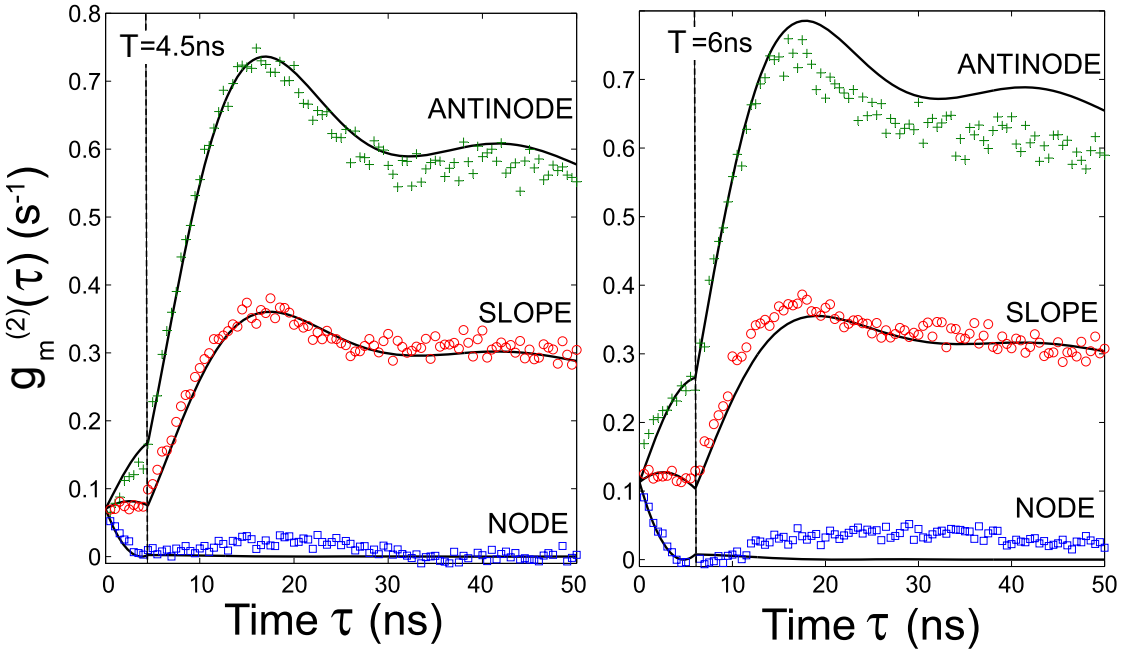

Figure 8.6: Measured correlation function $g_m^{(2)}(\tau)$, after subtraction of the non-interfering part, for the ion placed near a node (squares), a slope (circles) and an anti-node (crosses) of the standing-wave mirror mode. Each data set corresponds to 3 hours of integration. The lines represent the results of Eq. (8.2).

9 Quantum interference from photons emitted by a single ion

In this chapter an experiment is discussed, where the single Ba^+ ion is converted into a pseudo two-photon source by splitting its resonance fluorescence, delaying part of it, and recombining both parts on a beam splitter. A Hong-Ou-Mandel two-photon interference is observed with a contrast reaching 83 %. The spectral brightness of this two-photon source is quantified and compared to parametric down conversion devices.

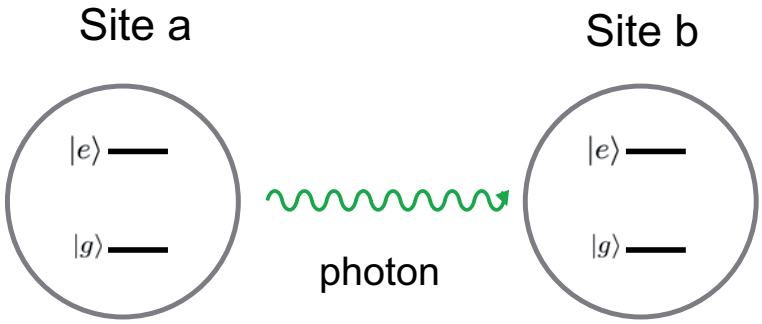

Figure 9.1: A quantum network: Two static quantum bits (e.g. atoms with excited state $|e\rangle$ and ground state $|g\rangle$) at site a and b are connected via flying, photonic q-bits.

As mentioned in the introduction, two photon interference is a basic component in a "quantum network" (Fig. 9.1), where atoms/ions are static qubits and photons are the flying qubits. Schemes proposed in [106, 111] describe possible ways to entangle two atoms in such a network by measuring emitted photons via a beam-splitter, i.e. measurement-induced entanglement. Its efficiency highly depends on the indistinguishability of the emitted photons, which can be characterized directly by two-photon interference. The effect of two-photon interference was observed for the first time in 1987 by Hong, Ou and Mandel [115] studying a parametric down conversion system, more recent studies were done with atoms in dipole traps [113] and two ions in remote traps [105]. Similar experiments were performed with an atom-cavity system [108] and quantum dots [109].

Here, the phenomenon of two-photon interference is studied for photons emitted from just one ion. It is shown, that this setup is a pseudo two-photon source of

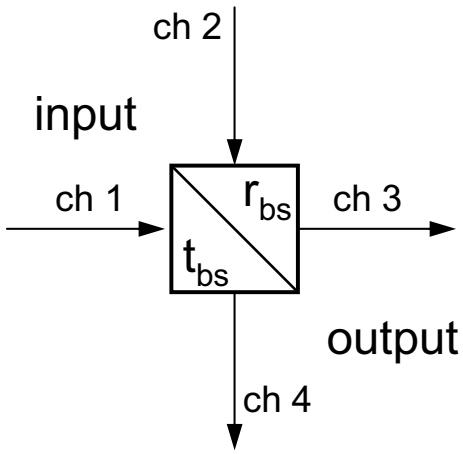

Figure 9.2: A 50/50 beamsplitter and its input and output channels (ch). r_{bs} and t_{bs} are the reflection and transmission coefficients.

reasonable quality, i.e. with high spectral brightness, as will be discussed later. A possible application would be entanglement distribution following a scheme proposed in [104].

In the first part, a general introduction into the quantum description of a beam splitter and the phenomenon of two-photon interference is discussed. The general analysis is then applied to the case where single photons emitted by the Ba^+ ion are sent to a 50/50 beam splitter. Finally the experimental results are discussed. This work is summarized in [107].

9.1 Quantum description of a beam splitter

At the heart of a two-photon interference setup is a 50/50 beam splitter. Following the notation of [110] and [115] this optical device is described with two input ports (denoted with 1 and 2) and two output ports (3 and 4), as shown in Fig. 9.2. In classical physics two coherent incident light beams with complex amplitude α_1 and α_2 interfere at the beam splitter according to a linear transformation $\mathbf{B}$ (2 x 2 transformation matrix) creating the output amplitudes α_3 and α_4

$$\begin{pmatrix}\alpha_1\\ \alpha_2\end{pmatrix} = \mathbf{B}\begin{pmatrix}\alpha_3\\ \alpha_4\end{pmatrix}. \tag{9.1}$$

In quantum optics the complex amplitudes correspond to bosonic operators for the different ports, i.e. $\hat{a}_1$, $\hat{a}_2$ for the input ports and $\hat{a}_3$, $\hat{a}_4$ for the output ports respectively. The linear transformation at the beam splitter is also valid for the quantized field, i.e.

$$\begin{pmatrix}\hat{a}_1\\ \hat{a}_2\end{pmatrix} = \mathbf{B}\begin{pmatrix}\hat{a}_3\\ \hat{a}_4\end{pmatrix}. \tag{9.2}$$

The bosonic operators fulfill the commutation rules

$$[\hat{a}_i, \hat{a}_j^\dagger] = \delta_{ij} , \quad [\hat{a}_i, \hat{a}_j] = [\hat{a}_i^\dagger, \hat{a}_j^\dagger] = 0. \tag{9.3}$$

The transformation matrix $\mathbf{B}$ has to be unitary ($\mathbf{B}^{-1} = \mathbf{B}^\dagger$) to provide conservation of energy and to ensure the correct commutation rules. We choose

$$\begin{pmatrix} \hat{a}_1 \\ \hat{a}_2 \end{pmatrix} = \begin{pmatrix} t_{bs} & ir_{bs} \\ ir_{bs} & t_{bs} \end{pmatrix} \begin{pmatrix} \hat{a}_3 \\ \hat{a}_4 \end{pmatrix}, \tag{9.4}$$

where r_{bs} and t_{bs} are the (field) reflection and transmission coefficients of the beam splitter (index bs), such that

$$r_{bs}^2 + t_{bs}^2 = 1 . \tag{9.5}$$

The coefficients r_{bs} and t_{bs} are considered to be the same for all polarizations. Moreover, the number operator $\hat{n}_i = \hat{a}_i^\dagger \, \hat{a}_i$ can be used to express the energy conservation

$$\hat{n}_1 + \hat{n}_2 = \hat{n}_3 + \hat{n}_4. \tag{9.6}$$

An alternative choice of the beam-splitter transformation matrix is used in [110], it reads

$$\mathbf{B} = \begin{pmatrix} t_{bs} & r_{bs} \\ -r_{bs} & t_{bs} \end{pmatrix}. \tag{9.7}$$

9.1.1 Input and Output states

First, we study an input state with one photon in mode 1 and one in mode 2, i.e. a two Fock-state. We assume that both photons are in the horizontal polarization mode. The states are obtained by applying creation operators to the vacuum state[1] $|0\rangle = |0\rangle_1 \otimes |0\rangle_2$

$$|\Psi_{in}\rangle = \hat{a}_1^\dagger \hat{a}_2^\dagger |0\rangle_1 |0\rangle_2 = |1\rangle_1 |1\rangle_2. \tag{9.8}$$

The transition from input state to output state $|\Psi_{out}\rangle$ is described by the beam-splitter transformation, i.e. Eq. 9.4. It is equivalent to the evolution of the input operators (Heisenberg picture). Substituting the creation operators in Eq. (9.8) yields the output state

$$\begin{aligned} |\Psi_{out}\rangle &= (t_{bs}\hat{a}_3^\dagger - ir_{bs}\hat{a}_4^\dagger)(-ir_{bs}\hat{a}_3^\dagger + t_{bs}\hat{a}_4^\dagger)|0\rangle \\ &= (-ir_{bs}t_{bs}(\hat{a}_3^\dagger)^2 - ir_{bs}t_{bs}(\hat{a}_4^\dagger)^2 - r_{bs}^2\hat{a}_4^\dagger\hat{a}_3^\dagger + t_{bs}^2\hat{a}_3^\dagger\hat{a}_4^\dagger)|0\rangle \end{aligned} \tag{9.9}$$

The first two terms correspond to states where the two input photons both go into the same output channel, i.e. one photon is transmitted and the other one is reflected. The other two options, where one photon appears in either output port, correspond to

[1] Note that the two particles in two different input modes are identical in the case of bosons.

a transmission or reflection of *both* photons. For photons of identical polarization, e.g. $|H\rangle$, these two cases are indistinguishable, both create a state $|1\rangle_{3,H}|1\rangle_{4,H}$. Formally, we can write $\hat{a}_4^\dagger, \hat{a}_3^\dagger = \hat{a}_3^\dagger \hat{a}_4^\dagger$ due to the commutator relation for independent bosonic modes $[\hat{a}_i^\dagger \hat{a}_j^\dagger] = 0$. Equation (9.9) then reads

$$|\Psi_{out}\rangle = (-ir_{bs}t_{bs}(\hat{a}_3^\dagger)^2 - ir_{bs}t_{bs}(\hat{a}_4^\dagger)^2 + (t_{bs}^2 - r_{bs}^2)\hat{a}_3^\dagger \hat{a}_4^\dagger)|0\rangle \tag{9.10}$$

For a 50:50 beam splitter $r_{bs} = t_{bs} = 1/\sqrt{2}$ the amplitude for the $|1\rangle_{3,H}|1\rangle_{4,H}$ state vanishs. The unitarity of the transformation matrix $\mathbf{B}$ ensures opposite sign for both photons reflected and the transmitted. We obtain an output state for indistinguishable photons of

$$|\Psi_{out}\rangle = \frac{-i}{\sqrt{2}}(|2\rangle_3|0\rangle_4 + |0\rangle_3|2\rangle_4), \tag{9.11}$$

where $-i$ is a global phase. To summarize, two incoming, indistinguishable photons will always leave a 50:50 beam splitter together in the same output port. This effect is also called **coalescence** of photons and can be used to measure the degree of indistinguishability of the photons.

This behavior is *not* observed for (incoming) photons with different polarizations. The last two terms for the output state in Eq. 9.9, i.e. the reflection and transmission of both photons lead to distinguishable states. That is why these probability amplitudes can not be subtracted in this case. We distinguish the photon operators with a polarization index H and V. Photons are assumed to be horizontally (vertically) polarized in mode 1 (2), respectively leading to an input state

$$|\Psi_{in}\rangle = \hat{a}_{1,H}^\dagger \hat{a}_{2,V}^\dagger |0\rangle = |1\rangle_{1,H}|1\rangle_{2,V}. \tag{9.12}$$

The same procedure as before yields a state

$$|\Psi_{out}\rangle = (ir_{bs}t_{bs}\hat{a}_{3,H}^\dagger \hat{a}_{3,V}^\dagger + ir_{bs}t_{bs}\hat{a}_{4,H}^\dagger \hat{a}_{4,V}^\dagger - r_{bs}^2 \hat{a}_{4,H}^\dagger \hat{a}_{3,V}^\dagger + t_{bs}^2 \hat{a}_{3,H}^\dagger \hat{a}_{4,V}^\dagger)|0\rangle, \tag{9.13}$$

where the photons in the output ports remain distinguishable by their polarization. As a consequence, $|1\rangle_3|1\rangle_4$ output-states do *not* vanish for the case of *distinguishable* photons and correlations are measured.

9.1.2 Hong-Ou-Mandel (HOM) Dip

Thus, a possible characterization of the output state of a beam splitter is to measure correlations, i.e. the joint probability of detecting a photon in both of the output channels. For that, a photon counting device (e.g. photomultipliers (PMT) or avalanche diodes (APD)) is used. A two photon state like $|2\rangle_3|0\rangle_4$ creates *one* click in one PMT, the dead-time of the PMT prevents from detecting the second photon. Only states with one photon in each output channel like $|1\rangle_3|1\rangle_4$ (or $|1\rangle_{3,H}|1\rangle_{4,V}$, $|1\rangle_{3,V}|1\rangle_{4,H}$) create clicks in both PMT's at the same time (coincidences), regardless of the polarization of the

input photons. Since states with identical polarizations show the effect of coalescence, one would expect a continuous drop of the coincidence rate down to 0 as the input photons become "more and more" identical. Here, all properties of photons play a role: Frequency, coherence length, polarization or the spatial mode they occupy. In the case discussed here, photons vary in polarization only, since they are emitted by the same ion.

The effect of a drop in the coincidence rate as a consequence of two photon interference is called Hong-Ou-Mandel (HOM) interference in honor to the people, who performed this type of experiments for the first time in 1987 [115].

9.1.3 Evaluation of the coincidence counts/rate

The evaluation of the coincidence rate corresponds to the measurement of correlations. Mathematically, one has to evaluate the second-order correlation function among channel 3 and 4. Introducing different times for the photon detection and using the usual normalization procedure we can define the correlation function written in terms of bosonic field operators of the output modes

$$g^{(2)}(t, t+\tau) = \frac{\langle \hat{a}_3^\dagger(t)\hat{a}_4^\dagger(t+\tau)\hat{a}_4(t+\tau)\hat{a}_3(t)\rangle}{\langle \hat{a}_3^\dagger(t)\hat{a}_3(t)\rangle\langle \hat{a}_4^\dagger(t)\hat{a}_4(t)\rangle} \ . \tag{9.14}$$

The correlation function describes the coincidence rate as a function of the time delay between the photon detection. For $\tau = 0$ it gives the detection rate of two photons arriving at the same time.

9.1.4 A classical light field

For example, an input field with amplitude E_0 in both input channels is considered. The input channel 2 has an arbitrary phase relative to channel 1, i.e. $E_0 e^{i\phi}$, but the fields are supposed to have the same polarization. The input fields are transformed according to

$$E_3 = t_{bs}E_0 + ir_{bs}E_0\ e^{i\phi} \qquad\qquad E_4 = ir_{bs}E_0 + t_{bs}E_0\ e^{i\phi} \tag{9.15}$$

The correlation function at time $\tau = 0$ reads

$$g^{(2)}(0) = \frac{\frac{1}{2\pi}\int_0^{2\pi}\langle E_3^\dagger E_4^\dagger E_4 E_3\rangle d\phi}{\langle E_3^\dagger E_3\rangle\langle E_4^\dagger E_4\rangle} \tag{9.16}$$

$$= \frac{\frac{1}{2\pi}\int_0^{2\pi}\langle |E_0|^4 - |E_0|^4 sin^2\phi\rangle d\phi}{\frac{1}{2\pi}\int_0^{2\pi}\langle |E_0|^2 - |E_0|^2 sin\phi\rangle\langle |E_0|^2 + |E_0|^2 sin\phi\rangle d\phi}. \tag{9.17}$$

For a fluctuating phase the integral yields $\sin\phi = 0$ and $\sin^2\phi = 1/2$. As a consequence $g^{(2)}(0) = 1/2$ for a random phase. Note that for a given phase $\varphi = 0$ the correlation

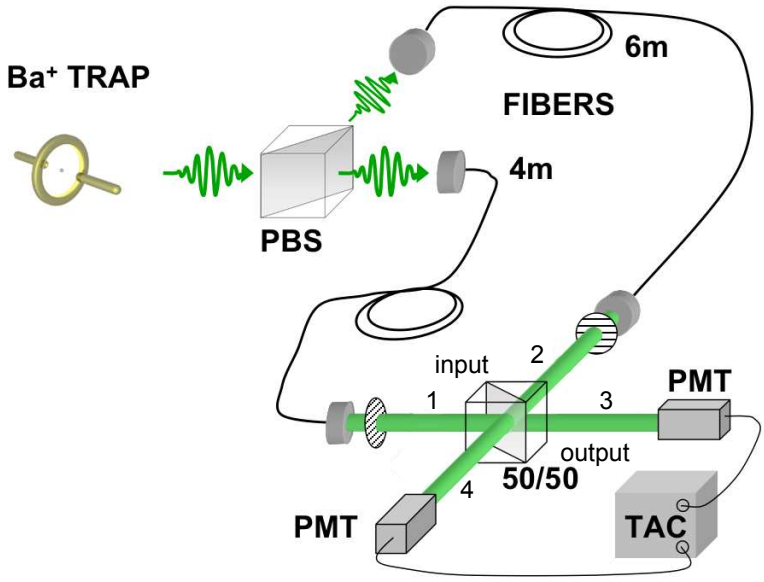

Figure 9.3: Sketch of the experimental setup: Fluorescence photons are collected in two single mode optical fibers and send to the interferometer. PBS...polarizing beam splitter, TAC...time acquisition card

function is $g^{(2)}(0) = 1$, while for $\phi = \pi/2$ the correlation function is $g^{(2)}(0) = 0$, i.e. no correlations are measured. In this case the relative phase between the incoming fields leads to a destructive interference in one of the output arms. Therefore, the intensity is nulled and correlations can not be measured.

The simple quantum description of a beam splitter does not include any discussion about how the photons are generated. In the following it will be shown how photons emitted from a single ion can be used as input of the beam splitter.

9.2 A single-ion two-photon source

9.2.1 Setup

Figure 9.3 shows a 3D-sketch of the experimental setup used for this experiment, Fig. 9.4 gives a more detailed overview. The green resonance fluorescence of the Barium ion is collected with the Halo-lens inside the vacuum chamber (cf. ch. 4), passes a telescope for beam size matching and a polarizing beam splitter, which splits the light into equal amplitudes. The two output channels are coupled to single mode optical fibers of 4 and 6 meters length, respectively. This length difference introduces a time delay of $T=$ 10 ns. The polarization of the photons is controlled by a combination of a polarizing

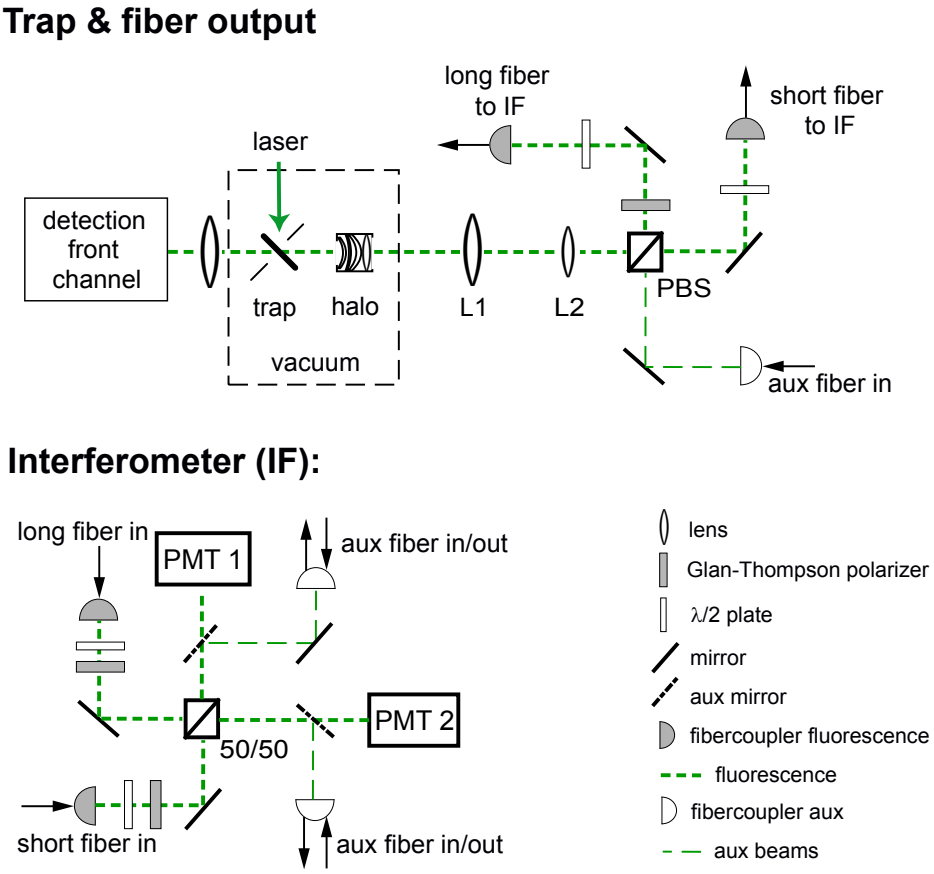

Figure 9.4: Detailed experimental setup. *Top:* Fluorescence photons are collected in two single mode optical fibers and guided to the interferometer (IF). Polarization is controlled using the combination of a polarizing beam splitter (PBS) and half wave-plates. At the fiber outputs, photons are vertically polarized by Glan-Thompson polarizers (hatched discs). Single photon arrival times are monitored with a Time Acquisition Card (TAC) with up to 100 ps resolution.

beam splitter (PBS) and half wave-plates. At the fiber outputs, photons are vertically polarized by Glan-Thompson prisms to cancel polarization fluctuations of the fiber transmission. Single photon arrival times are monitored in a Hanbury-Brown & Twiss setup with sub-nanosecond time resolution. Auxiliary beams guiding coherent laser light are used for adjusting the interferometer.

The exciting laser intensities are adjusted such that the second order photon correlations at T become large. The height of the first optical nutation (cf. ch. 3) is controlled by laser intensities and can be arbitrary large for the Ba^+ ion's complex level structure [63]. The introduced time delay is chosen to meet the first optical nutation, where

the probability to produce 2coincident photons is increased.

9.2.2 The model

Neglecting the motion of the ion, in a frame rotating at the laser frequency, ω_L, the green photon field radiated by the ion reads

$$\widehat{E}_i(t) = \xi e^{-i\omega_L t}\sigma^-(t)\theta(t), \tag{9.18}$$

where ξ represents a constant amplitude and θ is a step function centered at t=0. The lowering Pauli operator from $|\mathrm{P}_{1/2}\rangle$ to $|\mathrm{S}_{1/2}\rangle$, σ^-, is associated with a single photon creation. The 4 and 6 meter fibers are attached to the entrance ports of the interferometer labelled with "1" and "2". The incoming photons all have a vertical polarization, the two output ports are denoted "3" and "4". Adopting the notation used in the previous sections with field transmission (t_{bs}) and reflection (r_{bs}) coefficients, the field operators in the output arms "3" and "4" read

$$\begin{aligned}\widehat{E}_3(t) &= t_{bs}\widehat{E}_i(t-\alpha)e^{i\phi} + ir_{bs}\widehat{E}_i(t-\alpha-T)\\ \widehat{E}_4(t) &= t_{bs}\widehat{E}_i(t-\alpha-T) + ir_{bs}\widehat{E}_i(t-\alpha)e^{i\phi},\end{aligned} \tag{9.19}$$

where α takes into account the delay between emission and collection of green photons and can be set to zero without loosing generality. The time-argument T is couting for the delay picked up in the long fiber. The fields at the two input ports have here been directly expressed in terms of $\widehat{E}_i$. The phase ϕ corresponds to random fluctuations between the output fields of the two fibers. Although the two output modes are in an identical polarization state and are overlapping with a precision of $\approx 5-10\mu m$ for the 3 mm beam diameter, the detection setup does not allow for a sub-wavelength mechanical stability which justifies the introduction of ϕ. For a 50/50 beam splitter $r_{bs} = t_{bs} = 1/\sqrt{2}$ and the fields in the two output arms can then be written

$$\begin{aligned}\widehat{E}_3(t) &= \frac{1}{\sqrt{2}}\left[\widehat{E}_i(t)e^{i\phi} + i\widehat{E}_i(t-T)\right]\\ \widehat{E}_4(t) &= \frac{1}{\sqrt{2}}\left[\widehat{E}_i(t-T) + i\widehat{E}_i(t)e^{i\phi}\right].\end{aligned} \tag{9.20}$$

We can now evaluate the correlations measured in output arms, i.e. calculate

$$g^{(2)}(t,t+\tau) \propto \langle \widehat{E}_4^\dagger(t)\widehat{E}_3^\dagger(t+\tau)\widehat{E}_3(t+\tau)\widehat{E}_4(t)\rangle\ . \tag{9.21}$$

After inserting Eq. (9.20) and (9.18) into (9.21), evaluating the steady state limit ($t\to\infty$) and averaging over all the possible values for $\phi\in[0,2\pi]$, the second-order correlation function reads

$$g^{(2)}(\tau) \propto\ 2|b_{\mathrm{P}_{1/2}}(\tau)|^2 + |b_{\mathrm{P}_{1/2}}(|\tau-T|) - b_{\mathrm{P}_{1/2}}(\tau+T)|^2, \tag{9.22}$$

where $b_{P_{1/2}}$ denotes the occupation amplitude of the $P_{1/2}$ level, as described in Chapter 3. For the case that the two input modes $\widehat{E}_1$ and $\widehat{E}_2$ do not interact, e.g. if they are not spatially overlapping or if their polarization is different, the normalized correlation function then reads

$$g^{(2)}_{ni}(\tau) \propto \; 2|b_{P_{1/2}}(\tau)|^2 + |b_{P_{1/2}}(|\tau - T|)|^2 + |b_{P_{1/2}}(\tau + T)|^2. \tag{9.23}$$

In the following two-photon interference experiments, a mixture of interacting and non interacting correlations is measured. These have respective weights governed by the interference contrast, V, yielding a measured correlation function,

$$g^{(2)}_{meas}(\tau) \propto V g^{(2)}(\tau) + (1 - V) g^{(2)}_{ni}(\tau) \; . \tag{9.24}$$

9.2.3 Results

One fiber

In the inset part of Fig. 9.5 the normalized second order correlation function is presented when one of the two fibers is blocked. The usual single ion $g^{(2)}$-function is measured and shows an almost ideal anti-bunching ($g^{(2)}(0)$=0.02(2) with no background subtraction) and a large optical nutation ($g^{(2)}(13ns)$=3.0(3)). The measurement is used for calibration purposes.

Two fibers: Incoherent addition

Figure 9.5 also shows the normalized second order correlation when the two fiber output modes are not overlapping at the beam splitter, i.e. the non-interacting case or "incoherent addition"[2]. The black line shows the theoretical prediction based on Eq.(9.23). Second-order photon correlations are well reproduced by the dashed lines representing the three delayed, but non-interacting correlation functions from Eq. (9.23) centered at τ=0 and τ=$\pm T$, respectively. Experimental data are presented with a 500 ps resolution and the corresponding variance obtained from shot noise (Poisson statistics at all times τ). Moreover, the number of measured photon pairs with zero time-delay, $g^{(2)}_{ni}(0)$= 1.3(1), is higher than the normalization ($g^{(2)}_{ni}(\infty)$=1), i.e. the average intensity squared. This proves a successive conversion of a single ion into a bright source of two coincident photons.

Two fibers: Optimal overlap

The normalized second order correlation function for an optimum overlap of the two fiber output modes is presented in Fig. 9.6. Compared to Fig. 9.5, a large drop in the coincidence rate is observed with a measured value of 0.21(5). The experimental data

[2]This situation could also be reproduced with orthogonal polarization inputs.

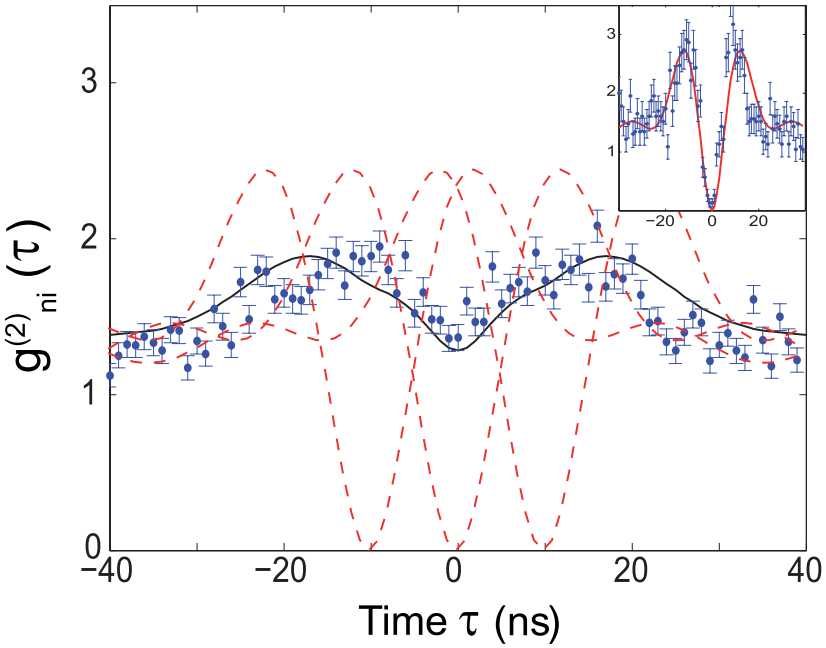

Figure 9.5: Normalized second order correlation function when the two fiber output modes are not overlapping. Data points correspond to an accumulation of one hour. The black line shows the theoretical prediction, $g^{(2)}_{ni}$, using experimental parameters. *Inset:* Normalized second order correlation function when one fiber output mode is blocked. The red line presents the solution of the Bloch equations for the experimental parameters. Note the amplitude of the optical nutation.

are obtained after 30 minutes of accumulation and presented with 500 ps resolution. The corresponding variance is obtained from shot noise (Poisson statistics at all times τ). In fact, long integration times limit the contrast of the measured two-photon interference. A drift of about 5-10 % of the interference contrast has been observed within 1-2 hours, most likely as a consequence of mechanical instabilities of the interferometer.

For a perfect destructive two-photon interference one would expect $g^{(2)}(0) = 0$. In Eq. (9.22), the first term (dashed line in Fig. 9.6) represents the contribution from correlations between photons emerging from the same source (the same fiber). For a single ion/atom this contribution vanishes at τ=0 as shown in the inset of Fig. 9.5. The second term in Eq. (9.22) (dashed-dotted line in Fig. 9.6) describes the destructive interference between the amplitudes associated with successive photon detections at times $\{t; t + |\tau - T|\}$ and $\{t; (t + \tau + T)\}$. These two contributions are identical at $\tau = 0$, consequently the coincidence rate vanishes. This is then a result of both the anti-bunching nature of photon emission and the destructive interference of two-photon state amplitudes, i.e. the Hong-Ou-Mandel dip. Without the latter, the second order

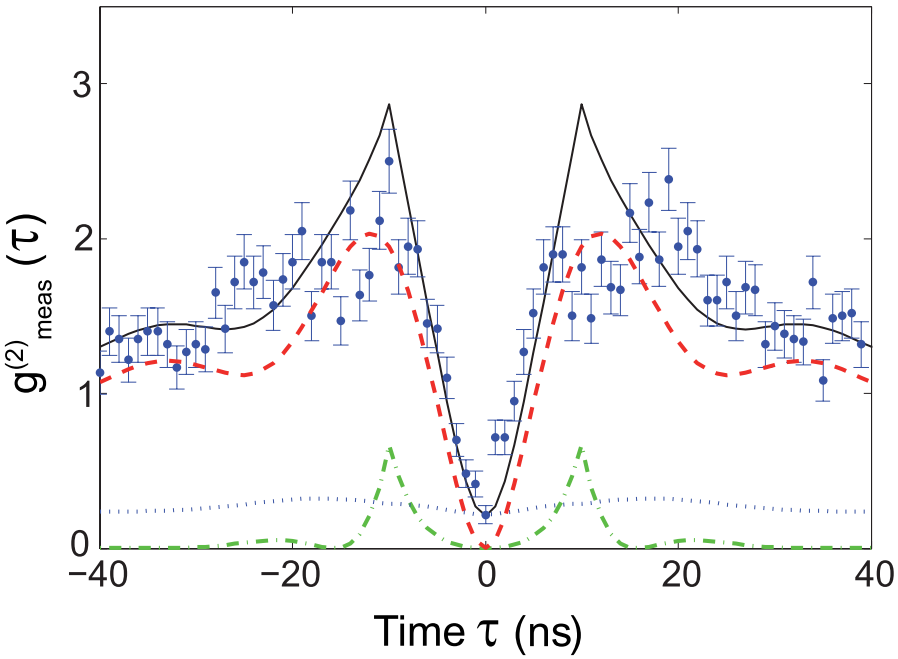

Figure 9.6: Normalized second order correlation function for an optimum overlap between the fiber output modes. The solid line shows the result of our predictions for $V = 83\%$, i.e. $g^{(2)}_{meas} \propto 0.83 g^{(2)} + 0.17 g^{(2)}_{ni}$. The first contribution splits into two parts: The first term of Eq. 9.22 shown as the red, dashed line, and the second term drawn as the green, dashed-dotted line. Background contributions, i.e. $g^{(2)}_{ni}$, are described by the dotted line.

correlation function is not necessarily anti-bunched (see for instance Fig. 9.5)

The measured second-order correlation function still shows a non-vanishing value at τ=0. These detected coincidences have two components: one part is due to accidental correlations between stray-light and fluorescence photons and the other part is given by the fraction of distinguishable photons which are detected. The first contribution is measured to be 3 % and is neglected in Fig. 9.6. The second part derives from imperfect optical alignment such as partial or unmatched mode overlap between the two fiber outputs. From the situation where the two fiber output modes are completely distinguishable – Fig. 9.5 with $g^{(2)}_{ni}(0)$= 1.3 (1) – one can conclude that the degree of indistinguishability of the photons detected, i.e. the two photon interference contrast (V), is equal to 83(5) % without subtracting accidental counts. Finally, the line-shape of the observed two-photon coalescence shows a peculiar statistical behavior almost completely characterized by the $g^{(2)}$ – correlation function, i.e. by the statistics of photon emission. The coherent excitation process shows up as an oscillatory behavior (optical nutation) in the correlation function. The two-photon coalescence reveals a similar effect, as can be seen in Fig. 9.6 and/or Eq. (8.3).

9.2.4 A comparison to parametric down conversion

The generated "single-ion two-photon source" system has to be compared to Parametric down-conversion setups (PDC), *the* model system for producing entangled photon pairs. PDC photons exhibit a spectral linewidth of the order of 50 GHz [114]. Associated with a rate of $\approx 3\ 10^6$ pairs/s, a spectral brightness reducing to at most 50 pairs/s per MHz is deduced. In our measurements, a rate of ≈ 1 pair/s is achieved, at a detection rate of $\approx 2\text{x}10^4$ photons/channel/s including all detection losses. Elastically scattered photons have a linewidth of few 10 kHz and then exhibit a spectral brightness about 50 pairs/s per MHz. Inelastically scattered photons have a linewidth of 15.7 MHz yielding a spectral brightness of ≈ 0.1 pairs/s per MHz. This rate can be increased by at least an order of magnitude since the optical nutation in the correlation function can reach ≈ 20 for appropriate laser excitations [63]. Furthermore, in the new setup two high halo-lenses collecting a total solid angle of 8 % are installed. These should allow to enhance the spectral brightness by another order of magnitude. Inelastically scattered photon-pairs could then reach a spectral brightness of ≈ 20 pairs/s per MHz like typical PDC based devices. Based on atomic ensembles, the most efficient two-photon source has been demonstrated with a spectral brightness as high as $5\text{x}10^4$ pairs/s per MHz [11].

In summary, splitting the resonance fluorescence, delaying part of it and recombining both parts on a beam splitter, allows one to efficiently produce almost ideal two-photon pairs. The spectral brightness obtained is shown to be comparable with parametric down-conversion devices. Fluorescence photon pairs are therefore candidates to achieve entanglement distribution protocols. The success of the latter however requires a high photon-ion coupling efficiency which can be reached combining an optical cavity and high numerical aperture optical lenses. Thus, this analysis will be of interest when single atoms and resonance fluorescence photons are at the node of quantum networks.

10 Summary and conclusion

This work reported on a selection of textbook experiments performed with a single, laser-cooled Barium ion stored in a Paul trap, a ring trap. Quantum optic experiments of two categories were carried out: Quantum feedback experiments and quantum correlation measurements in various setups. In parallel, a new, linear trap setup was constructed, integrated into the old setup and proved to be fully operational by showing ion images, compensation of micromotion, excitation spectra, self-interference of single resonance fluorescence photons and motional sidebands of the ion. Furthermore, a new, simple and highly efficient photo-ionization method was implemented used for both trap setups.

In a first experiment, quantum feedback to the single ion was demonstrated. Based on a homodyne setup, the self-interference of single resonance fluorescence photons allowed us to measure the position and thus the motion of the ion as an electronic signal. Proper feedback processed in an electronic circuit was influencing the motion of the ion, from feedback heating to feedback cooling. The latter proved to provide a shot-noise limited, one-dimensional electronic cooling below the Doppler limit, down to 70% of the ion's initial energy. Results were obtained by comparing motional spectra and ion-energies under different feedback operations. A comparison to a quantum-mechanical model resulted in an estimation of the mean phonon number of the vibrational states.

Moreover, second order correlation measurements of the resonance fluorescence of the ion in front of the mirror were investigated. For a short ion-mirror distance, the correlation function was demonstrated to be a perfect tool for investigating all degrees of freedom of the ion, its internal and external degrees. Thereby, the correlation function was used to study the dynamics of the ion covering a temporal range from nano-seconds to milli-seconds with a resolution of 1 ns and less. Anti-bunching was observed for short times, while modulations of the second order correlation function at bigger times were interpreted as a time-resolved measurement of the secular sidebands of the ion. The analysis was used to determine the motional sidebands and to prove the trap stability.

Second order correlation functions for an increased ion-mirror distance were investigated later. The analysis considered a non-Markovian regime, i.e. a regime, where retardation effects played a crucial role. The delay-time introduced by a photon-round trip towards the mirror and back was on the order of the lifetime of the excited state (7 ns) for an ion-mirror distance of almost one meter. The observation of photon pairs was shown to be influenced by the relative placement of the ion in the standing wave of the self-interference. These measurements proved the establishment of a standing wave in a half-cavity.

In the last experiment, Hong-Ou-Mandel interference of fluorescence photons of the Barium ion was shown. The phenomenon of two-photon interference was used to determine the degree of indistinguishability of the photons. The setup proved to produce two-photon pairs of reasonable spectral brightness taking benefit of the low bandwidth of fluorescence photons compared to down-conversion photon-pairs.

The effect of two-photon interference plays an important role for quantum networking as being *the* measure of indistinguishability which several protocols of entanglement and state transfer rely on [106, 111]. While possible realizations of deterministic quantum network operations rely on pulsed measurements, preparation and detection schemes [22], a fundamentally different "coupling" of two ions in two remote traps appear to be more suitable for the present experimental setup. As a logical step it is apparent to extend the feedback experiments shown in this work and in [32] to the case of two traps, i.e. coupling the mechanical properties of the two "harmonic oscillators" (the ions) in two distant traps. In particular, the oscillation phase of ion 1 and ion 2 could be stabilized. Moreover, influencing the oscillation amplitude, similar to the case studied in ch. 6, appears to be a proper tool to transfer energy from one ion to the other. Even a coupling to other oscillators, e.g. nano-mechanical oscillators, could be a challenging system to study coupled oscillators at/in the quantum regime.

Bibliography

[1] M. Born and E. Wolf, *Principles of Optics*, Pergamon Press, Reprint (1993).

[2] W. Paul, *Ein neues Massespektrometer ohne Magnetfeld*, Z. Naturforsch. **A8**, 448 (1953).

[3] W. Paul, O. Osberghaus, and E. Fischer, *Ein Ionenkäfig*, Forschungsberichte des Wirtschafts- und Verkehrsministeriums Nordrhein-Westfalen 415, Westfälischer Verlag (1958).

[4] D. J. Wineland, and H. Dehmelt, *Proposed 1014 delta upsilon less than upsilon laser fluorescence spectroscopy on T1+ mono-ion oscillator III*, Bull. Am. Phys. Soc. **20**, 637, (1975).

[5] D. J. Wineland, R. E. Drullinger, and F. L. Walls, *Radiation-Pressure Cooling of Bound Resonant Absorbers*, Phys. Rev. Lett. **40**, 1639 (1978).

[6] W. Neuhauser, M. Hohenstatt, P. Toschek, and H. Dehmelt, *Optical-Sideband Cooling of Visible Atom Cloud Confined in Parabolic Well*, Phys. Rev. Lett. **41**, 233 (1978).

[7] J. I. Cirac and P. Zoller, *Quantum Computations with Cold Trapped Ions*, Phys. Rev. Lett. **74**, 4091 (1995).

[8] P. Zoller et al., *Quantum information processing and communication - Strategic report on current status, visions and goals for research in Europe*, Eur. Phys. J. D **36**, 203 (2005).

[9] H. J. Briegel, W. Dür, J. I. Cirac, and P. Zoller, *Quantum Repeaters: The Role of Imperfect Local Operations in Quantum Communication*, Phys. Rev. Lett **81**, 5932 (1998).

[10] R. Ursin , F. Tiefenbacher , T. Schmitt-Manderbach , H. Weier, T. Scheidl, M. Lindenthal, B. Blauensteiner, T. Jennewein, J. Perdigues, P. Trojek, B. Omer, M. Furst, M. Meyenburg, J. Rarity, Z. Sodnik, C. Barbieri, H. Weinfurter, and A. Zeilinger, *Entanglement-based quantum communication over 144km*, Nature Physics **3**, 481 (2007).

[11] J. K. Thompson, J. Simon, H. Loh, and V. Vuletic, *A high-brightness source of narrowband, identical-photon pairs*, Science **313**, 74 (2006).

[12] T. Wilk, S. C. Webster, H. P. Specht, G. Rempe, and A. Kuhn, *Polarization-controlled single photons*, Phys. Rev. Lett. **98**, 063601 (2007).

[13] D. N. Matsukevich and T. Chanelière and M. Bhattacharya and S.-Y. Lan and S. D. Jenkins and T. A. B. Kennedy and A. Kuzmich, *Entanglement of a Photon and a Collective Atomic Excitation*, Phys. Rev. Lett **95**, 040405 (2005).

[14] H. de Riedmatten, J. Laurat, C. W. Chou, E. W. Schomburg, D. Felinto, and H. J. Kimble, *Direct Measurement of Decoherence for Entanglement between a Photon and Stored Atomic Excitation*, Phys. Rev. Lett **97**, 113603 (2006).

[15] D. Felinto, C. W. Chou, J. Laurat, E. W. Schomburg, H. de Riedmatten, and H. J. Kimble, *Conditional control of the quantum states of remote atomic memories for quantum networking*, Nat. Phys. **2** (12), 844 (2006).

[16] H. Häffner, W. Hansel, C. F. Roos, J. Benhelm, D. Chek-al-kar, M. Chwalla, T. Korber, U. D. Rapol, M. Riebe, P. O. Schmidt, C. Becher, O. Guhne, W. Dur, and R. Blatt, *Scalable multiparticle entanglement of trapped ions*, Nature **438**, 643 (2005).

[17] B. B. Blinov, D.L. Moehring, L.-M. Duan, and C. Monroe, *Observation of entanglement between a single trapped atom and a single photon*, Nature **428**, 153 (2004).

[18] D. L. Moehring, M. J. Madsen, B. B. Blinov, and C. Monroe, *Experimental Bell Inequality Violation with an Atom and a Photon*, Phys. Rev. Lett **93**, 090410 (2004).

[19] J. Laurat, H. de Riedmatten, D. Felinto D, C.W. Chou, E. W. Schomburg, and H.J. Kimble, *Efficient retrieval of a single excitation stored in an atomic ensemble*, Opt. Express **14**, 6912 (2006).

[20] M. D. Eisaman, A. André, F. Massou, M. Fleischhauer, A. S. Zibrov, and M. D. Lukin, *Electromagnetically induced transparency with tunable single-photon pulses*, Nature **438**, 837 (2005).

[21] T. Chanelière , D. N. Matsukevich , S. D. Jenkins , S. Y. Lan , T. A. B. Kennedy, and A. Kuzmich, *Storage and retrieval of single photons transmitted between remote quantum memories*, Nature **438**, 833 (2005).

[22] D. L. Moehring, P. Maunz, S. Olmschenk, K. C. Younge, D. N. Matsukevich, L. M. Duan, and C. Monroe, *Entanglement of single-atom quantum bits at a distance*, Nature **449**, 68 (2007).

[23] L. Mandel, E. Wolf, *Optical Coherence and Quantum Optics* (Cambridge University Press, Boston, 1995).

[24] J.H. Kimble, M. Dagenais, and L. Mandel, *Photon Antibunching in Resonance Fluorescence*, Phys. Rev. Lett **39**, 691 (1977).

[25] F. Diedrich, and H. Walther, *Nonclassical radiation of a single stored ion*, Phys. Rev. Lett **58**, 203 (1987); M. Schubert, I. Siemers, R. Blatt, W. Neuhauser, and P. E. Toschek, *Photon antibunching and non-Poissonian fluorescence of a single three-level ion*, Phys. Rev. Lett **68**, 3016 (1992).

[26] R. Hanbury Brown and R. Q. Twiss, *Question of correlation between photons in coherent light rays*, Nature (London) **178** 1046 (1956).

[27] S. Lloyd, *Coherent quantum feedback*, Phys. Rev. A **62**, 022108 (2000).

[28] J. Eschner, Ch. Raab, F. Schmidt-Kaler, and R. Blatt, *Light interference from single atoms and their mirror images*, Nature **413**, 495-498 (2001).

[29] M. A. Wilson, P. Bushev, J. Eschner, F. Schmidt-Kaler, C. Becher, U. Dorner, and R. Blatt, *Vacuum-Field Level Shifts in a Single Trapped Ion Mediated by a Single Distant Mirror*, Phys. Rev. Lett. **91**, 213602 (2003).

[30] P. Bushev, A. Wilson, J. Eschner, Ch. Raab, F. Schmidt-Kaler, Ch. Becher, and R. Blatt, *Forces between a single atom and its distant mirror image*, Phys. Rev. Lett. **92**, 223602 (2004).

[31] J. Bolle, *Spektroskopie und nichtklassische Fluoreszenzeigenschaften von einzelnen gespeicherten Barium-Ionen* (Doktorarbeit, Innsbruck 1998).

[32] P. Bushev, *Interference experiments with a single Barium ion: From QED towards quantum feedback* (Dissertation, Innsbruck, 2004).

[33] P. Bushev, D. Rotter, A. Wilson, F. Dubin, Ch. Becher, J. Eschner, R. Blatt, V. Steixner, P. Rabl, and P. Zoller, *Feedback cooling of a single tarpped ion*, Phys. Rev. Lett. **96**, 043003 (2006).

[34] U. Dorner and P. Zoller, *Laser-driven atoms in half-cavities*, Phys. Rev. A **66**, 023816 (2002).

[35] R. P. Gosh, *Ion traps*, Clarendon Press, (1995).

[36] D. Leibfried, R. Blatt, C. Monroe, and D. Wineland, *Quantum dynamics of single trapped ions*, Rev. Mod. Phys. **75**, 281 (2003).

[37] D. F. V. James, *Quantum dynamics of cold trapped ions with application to quantum computation*, Appl. Phys. B **66**, 181 (1998).

[38] A. Steane, *The ion trap quantum information processor*, Appl. Phys. B **64**, 623 (1997).

[39] Ch. Roos, *Controlling the Quantum State of Trapped Ions* (Doktorarbeit, Innsbruck 2000).

[40] S. Gulde, *Implementing Quantum Gates With Ion Traps* (Doktorarbeit, Innsbruck 2003).

[41] H. C. Nägerl, *Ion Strings for Quantum Computation* (Doktorarbeit, Innsbruck, 1998).

[42] M. Riebe, *Preparation of entangled states and quantum teleportation with atomic qubits* (Doktorarbeit, Innsbruck, 2005).

[43] D. Rotter, *Photoionisation von Kalzium* (Diplomarbeit, Innsbruck, 2003).

[44] Ch. Raab, *Interference experiments with the fluorescence light of Ba^+ ions* (Doktorarbeit, Innsbruck, 2001).

[45] J. P. Schiffer, *Phase transitions in anisotropically confined ionic crystals*, Phys. Rev. Lett. **70**, 818 (1993).

[46] D. G. Enzer, M. M. Schauer, J. J. Gomez, M. S. Gulley, M. H. Holzscheiter, P. G. Kwiat, S. K. Lamoreaux, C. G. Peterson, V. D. Sandberg, D. Tupa, A. G. White, R. J. Hughes and D. F. V. James, *Observation of power-law scaling for phase transitions in linear trapped ion crystals*, Phys. Rev. Lett. **85**, 2466 (2000).

[47] M. G. Raizen, J. M. Gilligan, J. C. Bergquist, W. M. Itano, and D. J. Wineland *Ionic-Crystals In A Linear Paul Trap*, Phys. Rev. A **45**, 6493 (1992).

[48] S. Stenholm, *The semiclassical theory of laser cooling*, Rev. Mod. Phys. **58**, 699 (1986).

[49] D. R. Lide, *Handbook of chemistry and physics, 78^{th} edition*, CRC Press (1997-1998).

[50] NIST, *Basic atomic and spectroscopic data*, Online database, `http://physics.nist.gov/PhysRefData/ASD/index.html`

[51] R. Loudon, *The Quantum Theory of Light* (Clarendon Press, Oxford, 1983).

[52] H. Oberst, *Resonance fluorescence of sigle Barium ions*, (Diplomarbeit, University of Innsbruck, 1999).

[53] H. Dehmelt, *Proposed 1014delta Nu Less Than Nu Laser Fluorescence Spectroscopy On Tl+ Mono-Ion Oscillator*, Bull. Am. Phys. Soc. **18**, 1521 (1973).

[54] B. R. Mollow, *Power Spectrum of Light Scattered by Two-Level Systems*, Phys. Rev. **188**, 1969 (1969).

[55] C. Cohen-Tannoudji, *Atom-photon interaction*, A Wiley-interscience publication (1992)

[56] F. Y. Wu, R. E. Grove, and S. Ezekiel, *Investigation Of Spectrum Of Resonance Fluorescence Induced By A Monochromatic Field*, Phys. Rev. Lett. **35**, 1426 (1975).

[57] H. Walther, *Atomic Fluorescence Induced by Monochromatic Excitation*, Laser Spectroscopy 1975, Lecture Notes in Physics, Berlin Springer Verlag, **43**, 358, (1975)

[58] Y. Stalgies, I. Siemers, B. Appasamy, T. Altevogt and P. E. Toschek, *The spectrum of single-atom resonance fluorescence*, Europhys. Lett. **35**, 259 (1996).

[59] J. I. Cirac, R. Blatt, A. S. Parkins, and P. Zoller, *Spectrum Of Resonance Fluorescence From A Single Trapped Ion*, Phys. Rev. A **48**, 2169 (1993).

[60] M. Lindberg, *Resonance Fluorescence Of A Laser-Cooled Trapped Ion In The Lamb-Dicke Limit*, Phys. Rev. A **34**, 3178 (1986).

[61] Ch. Roos, Th. Zeiger, H. Rohde, H. C. Nägerl, J. Eschner, D. Leibfried, F. Schmidt-Kaler, and R. Blatt, *Quantum state engineering on an optical transition and decoherence in a Paul trap*, Phys. Rev. Lett. **83**, 4713 (1999).

[62] Ch. Raab, J. Eschner, J. Bolle, H. Oberst, F. Schmidt-Kaler, R. Blatt, *Motional sidebands and direct measurement of the cooling rate in the resonance fluorescence of a single trapped ion*, Phys. Rev. Lett. **85**, 538 (2000).

[63] M. Schubert, I. Siemers, R. Blatt, W. Neuhauser, and P. E. Toschek, *Transient Internal Dynamics Of A Multilevel Ion*, Phys. Rev. A **52**, 2994 (1995).

[64] Ch. Raab, J. Bolle, H. Oberst, J. Eschner, F. Schmidt-Kaler, and R. Blatt, *Diode laser spectrometer at 493 nm for single trapped Ba+ ions*, Appl. Phys. B **67**, 683 (1998).

[65] L. S. Ma, Ph. Courteille, G. Ritter, W. Neuhauser and R. Blatt, *Spectroscopy of Te2 with modulation transfer: Reference lines for precision spectroscopy in Yb+ at 467 nm*, Appl. Phys. B **57**, 683 (1993).

[66] R. D. Hudson and V. L. Carter, *Absorption Spectrum of Ba I in the Region of Autoionization from 2382 to 1700 Å*, Phys. Rev. A **2**, 1296 (1970).

[67] P. Esherick, J. A. Armstrong, R. W. Dreyfus, and J. J. Wynne, *Multiphoton Ionization Spectroscopy of High-Lying, Even-Parity States in Calcium*, Phys. Rev. Lett. **36**, 643 (1976).

[68] A. V. Steele, L. R. Churchill, P. F. Griffin, and M. S. Chapman, *Photoionization and photoelectric loading of barium ion traps*, Phys. Rev. A **75**, 053404 (2007).

[69] D. J. Armstrong, R. P. Wood, and C. H. Greene, *Photoionization Of The 5d6p 3d1 State Of Barium*, Phys. Rev. A **47**, 1981 (1993).

[70] D. J. Armstrong, and J. Cooper, *Isotope-Selective Photoionization Spectroscopy Of Barium*, Phys. Rev. A **47**, R2446 (1993).

[71] L.-W. He, C. E. Burkhardt, M. Ciocca, J. J. Leventhal, H.-L. Zhou and S. T. Manson, *Correlation effects in the photoionization of Ba(6s6p* $^1P_1$*): Determination of cross sections for production of specific final J states*, Phys. Rev. A **51**, 2085 (1995).

[72] L.-W. He, C. E. Burkhardt, M. Ciocca, J. J. Leventhal, and S. T. Manson, *Absolute cross sections for the photoionization of the 6s6p* ^1P *excited state of barium*, Phys. Rev. Lett. **67**, 2131 (1991).

[73] V. Lange, U. Eichmann, and W. Sandner, *Photoionization Of Excited Barium 6s6p (1)P1*, Phys. Rev. A **44**, 4737 (1991).

[74] R. P. Wood, C. H. Greene, and D. Armstrong, *Photoionization of the barium 6s6p* $^1P^{\circ}_1$ *state*, Phys. Rev. A **47**, 229 - 235 (1993).

[75] C. W. Gardiner and P. Zoller, *Quantum Noise* (Springer, Berlin, 2004).

[76] V. Steixner, P. Rabl, and P. Zoller, *Quantum feedback cooling of a single trapped ion in front of a mirror*, Phys. Rev. A **72**, 043826 (2005).

[77] H.M. Wiseman and G. J. Milburn, *Squeezing via feedback*, Phys. Rev. A. **49**, 1350 (1994).

[78] H. Häffner, W. Hansel, C. F. Roos, J. Benhelm, D. Chek al kar, M. Chwalla, T. Korber, U. D. Rapol, M. Riebe, P. O. Schmidt, C. Becher, O. Guhne, W. Dur and R. Blatt, *Scalable multi-particle entanglement of trapped ions*, Nature **438**, 643-646 (2005).

[79] D. Leibfried, E. Knill, S. Seidelin, J. Britton, R. B. Blakestad, J. Chiaverini, D. B. Hume, W. M. Itano, J. D. Jost, C. Langer, R. Ozeri, R. Reichle and D. J. Wineland, *Creation of a six-atom 'Schrodinger cat' state*, Nature **438**, 639-642 (2005).

[80] H.M. Wiseman and G. J. Milburn, *Quantum theory of optical feedback via homodyne detection*, Phys. Rev. Lett. **70**, 548-551 (1993).

[81] B. D'Urso, B. Odom, and G. Gabrielse, *Feedback Cooling of a One-Electron Oscillator*, Phys. Rev. Lett. **90**, 043001 (2003).

[82] T. Fischer, P. Maunz, P. W. H. Pinkse, T. Puppe and G. Rempe, *Feedback on the Motion of a Single Atom in an Optical Cavity*, Phys. Rev. Lett. **88**, 163002 (2002).

[83] N.V.Morrow, S.K. Dutta and G. Reithel, *Feedback control of atomic motion in an optical lattice*, Phys. Rev. Lett. **88**, 093003 (2002).

[84] J. E. Reiner, W. P. Smith, L. A. Orozco, H. M. Wiseman, and J. Gambetta, *Quantum feedback in a weakly driven cavity QED system*, Phys. Rev. A. **70**, 023819, (2004).

[85] J.M. Geremia, J. K. Stockton, and H. Mabuchi, *Real-Time quantum feedback control of atomic spin-squeezing*, Science **304**, 270 (2004).

[86] R. Ruskov and A. N. Korotkov, *Quantum feedback control of a solid-state qubit*, Phys. Rev. B **66**, 041401 (2002).

[87] A. Hopkins, K.Jacobs, S. Habib, and K. Schwab, *Feedback cooling of a nanomechanical resonator*, Phys. Rev. B **68**, 235328 (2003).

[88] S.Manchini, D.Vitali, and P. Tombesi, *Optomechanical cooling of a macroscopic oscillator by homodyne feedback*, Phys. Rev. Lett. **80**, 688 (1998).

[89] D.Vitali, S.Manchini, L.Ribichini, and P.Tombesi, *Mirror quiescence and high-sensitivity position measurements with feedback*, Phys. Rev. A **65**, 063803 (2002).

[90] V. Giovannetti, P.Tombesi, and D. Vitali, *Non-Markovian quantum feedback from homodyne measurements: The effect of a nonzero feedback delay time*, Phys. Rev. A **60**, 1549-1561 (1999).

[91] D. N. Klyshko, A. V. Masalov, *Photon noise: Observation, suppression, interpretation* Physics-Uspekhi **38**, 1203 (1995).

[92] L. Landau and E.Lifschitz, *Course of Theoretical Physics: Statistical Physics* (Pergamon, New York, 1958).

[93] J. Eschner, *Sub-wavelength resolution of optical fields probed by single trapped ions: Interference, phase modulation, and which-way information*, Eur. Phys. J. D **22**, 341-345 (2003).

[94] P. F. Cohadon, A. Heidmann, and M. Pinard, *Cooling of a Mirror by Radiation Pressure*, Phys. Rev. Lett. **83**, 3174 (1999).

[95] M. Pinard, P.F. Cohadon, T. Briant, and A. Heidmann, *Full mechanical characterization of a cold damped mirror*, Phys. Rev. A **63**, 013808 (2000).

[96] A.V.Masalov, A.A.Putilin, and M.V.Vasilyev, *Sub-Poissonian light and photocurrent shot noise suppression in closed opto-electronic loop*, J. Mod. Optics **41**, 1941 (1994).

[97] P. B. Coates, *Fast Measurement Of Short Time Intervals*, J. of Phys. E **1**, 878 (1968).

[98] F. Dubin, D. Rotter, M. Mukherjee, C. Russo, J. Eschner, and R. Blatt, *Photon correlation versus interference of single-atom fluorescence in a half-cavity.*, Phys. Rev. Lett. **98**, 183003 (2007)

[99] M. Hennrich, A. Kuhn, and G. Rempe, *Transition from Antibunching to Bunching in Cavity QED*, Phys. Rev. Lett **94**, 053604 (2005).

[100] P. Milonni, *The quantum vacuum* (Academic Press, London, 1993).

[101] A. Kreuter, C. Becher, G. P. T. Lancaster, A. B. Mundt, C. Russo, H. Häffner, C. Roos, J. Eschner, F. Schmidt-Kaler, and R. Blatt, *Spontaneous emission lifetime of a single trapped Ca+ ion in a high finesse cavity*, Phys. Rev. Lett. **92**, 203002 (2004).

[102] R.J. Cook, and P. W. Milonni, *Quantum theory of an atom near partially reflecting walls*, Phys. Rev. A **35**, 5081 (1987).

[103] G. Alber, *Photon wave packets and spontaneous decay in a cavity*, Phys. Rev. A **46**, R5338 (1992).

[104] B. Kraus and I. Cirac, *Discrete Entanglement Distribution with Squeezed Light*, Phys. Rev. Lett **92**, 013602 (2004).

[105] P. Maunz, D. L. Moehring, S. Olmschenk, K. C. Younge, D. N. Matsukevich and C. Monroe, *Quantum interference of photon pairs from two remote trapped atomic ions*, Nature Physics **3**, 538 (2007).

[106] C. Cabrillo, J. I. Cirac, P. García-Fernández, and P. Zoller, *Creation of entangled states of distant atoms by interference*, Phys. Rev. A **59**, 1025 (1999).

[107] F. Dubin, D. Rotter, M. Mukherjee, S. Gerber and R. Blatt, *Single-ion two-photon source*, Phys. Rev. Lett. **99**, 183001 (2007)

[108] T. Legero, T. Wilk, M. Hennrich, G. Rempe and A. Kuhn, *Quantum Beat of Two Single Photons*, Phys. Rev. Lett. **93**, 070503 (2004)

[109] D. Fattal, C. Santori, J. Vuckovic, G. S. Solomon, Y. Yamamoto, *Indistinguishable single photons from a quantum dot*, Phys. Stat. Sol. B-Basic Res. **238**, 305 (2003)

[110] U. Leonhard, *Measuring the quantum state of light*, Cambridge University Press, (Cambridge 1997).

[111] Simon C., W. T. M. Irvine, *Robust Long-Distance Entanglement and a Loophole-Free Bell Test with Ions and Photons*, Phys. Rev. Lett. **91**, 110405 (2003).

[112] D. L. Moehring, M. J. Madsen , K. C.Younge, R. N. Kohn Jr., P. Maunz , L. -M. Duan , C. Monroe , and B. B. Blinov et al., *Quantum networking with photons and trapped atoms (Invited)*, J. Opt. Soc. Am. B **24**, 300 (2007) .

[113] J. Beugnon, M. Jones, J. Dingjan, B. Darquie, G. Messin, A. Browaeys, and P. Grangier, *Quantum interference between two single photons emitted by independently trapped atoms*, Nature **440**, 779 (2006).

[114] F. Koening, E. J. Mason, F. N. C. Wong, and M. A. Albota, *Efficient and spectrally bright source of polarization-entangled photons*, Phys. Rev. A **71**, 033805 (2005).

[115] C. K. Hong, Z. Y. Ou, and L. Mandel, *Measurement of subpicosecond time intervals between two photons by interference*, Phys. Rev. Lett **59**, 2044 (1987).

Danksagung

Ich möchte an dieser Stelle all jenen meinen herzlichen Dank aussprechen, die mich bei der Fertigstellung dieser Arbeit begleitet und unterstützt haben. In erster Linie bedanke ich mich bei Rainer Blatt für die Möglichkeit, eine Dissertation in einem solch professionellen Umfeld durchführen zu können. Neben den wissenschaftlichen und finanziellen Resourcen, hat mich speziell die Möglichkeit beeindruckt, weltweit bekannte und wichtige Persönlichkeiten der Physik zu treffen. Der Besuch der Physik-Nobelpreisträger N. Ramsey, J. Hall, T. Hänsch und W. Ketterle im Barium-Labor während der ICAP 2006 wird mir immer in Erinnerung bleiben, speziell N. Ramsey's Kommentar "That's neat, that's neat..." habe ich immer noch im Ohr. Mir wurde stets viel Verantwortung für das Barium-Experiment übertragen und viel Freiraum gelassen, wodurch ich wertvolle Einblicke in die Leitung und Organisation eines Experimentes erhalten konnte. Ich möchte mich auch für die netten (und teilweise auch *leicht* ausufernden) Spießbratenabende in Rainer's Garten bedanken. Ich verstehe heute noch nicht, wie eine Gruppe von Physikern solche Berge von Fleisch vernichten kann.

Grosser Dank gilt natürlich meinen unmittelbaren Kollegen im Labor: Pavel Bushev lernte mich am Experiment ein und ermöglichte mir, gleich am ersten Labortag interessante Messungen zu machen. Unsere nächtlichen Labor-Gespräche über russische und auch nicht-russiche Artillerie waren für mich immer sehr amüsant und halfen mir die Müdigkeit zu überwinden. Auch François Dubin sei mein ganz spezieller Dank ausgesprochen. Sein Beitrag zu dieser Arbeit war essentiell. Unsere gemeinsame, mehr als zweijährige Arbeit, war sehr ergiebig, interessant und wertvoll. François brachte mir im besonderen die theoretische Seite unserer Messungen näher und hatte immer gute Ideen für neue Experimente. Ich bedanke mich auch bei François' Freundin Silvia, die oft für François und mich gekocht hat. Manas Mukherjee möchte ich besonders für seine Unterstützung beim Aufbau der neuen, linearen Falle und des Photo-Ionisationslasers danken. Auch Sebastian Gerber war am Aufbau und der Installation der neuen Falle maßgeblich beteiligt. Als noch das eine oder andere Problem der neuen Apperatur gelöst werden musste, war unser gemeinsames Motto "Augen zu und durch" oder besser gesagt "Vakuum auf und zu". Ich möchte mich auch für die sehr interessanten Gespräche und für den einen oder anderen Tip bzgl. "effizienten" Internetgebrauchs bedanken.

Besten Dank auch an Carlos Russo, der die Programme für die Auswertung unserer Korrelationsfunktionen zur Verfügung gestellt hat. Auch den restlichen Mitarbeitern

der Blatt-Gruppe sei gedankt für die Arbeitsatmosphäre und Hilfestellungen zu den verschiedensten Problemen. Namentlich möchte ich gerne meine Mensa-Mitstreiter Jan Benhelm, Mike Chwalla, Thomas Monz, Mark Riebe und Philipp Schindler erwähnen.

"Muchas gracias" an die Kollegen in Barcelona, Markus Hennrich, Felix Rohde und Carsten Schuck, mit deren Kooperation die neue Falle aufgebaut worden ist. Allen voran, Jürgen Eschner, der mich als ehemaliger Assistent des Barium-Experimentes am Anfang meiner Arbeit betreut hat und mit dem wir stets interessante Diskussionen geführt haben. An dieser Stelle seien auch die Mitarbeiter der mechanischen Werkstatt am Institut erwähnt, die die Fallen für Innsbruck und Barcelona gefertigt haben: Josef Dummer, Anton Schönherr, Helmut Jordan und Stefan Haselwandter.

Ich möchte auch jenen Menschen meinen Dank aussprechen, die mich während meiner Arbeit auf privater Ebene unterstützt haben. Dabei möchte ich mich im besonderen bei meinen Musikerkollegen und Freunden Daniel Rubin, Christian Schenk und Daniel Schrott für die "coolen" Stunden im Proberaum bedanken und bei meiner Familie für die vielseitige und herzliche Unterstützung durch all die Jahre meiner Ausbildung.

Am Ende, aber nicht zuletzt, möchte ich mich ganz herzlich bei meiner Freundin Anne für Ihre aufmerksame und liebevolle Unterstützung bedanken, die auch in schwierigen Zeiten während der Arbeit starken Rückhalt geboten hat.

Vielen Dank!